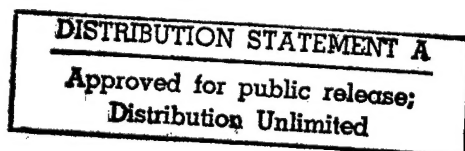# Low Tension Cable Dynamics and Prediction of

Vortex Induced Vibrations of Acoustic Array Cables

MARK A. GROSENBAUGH
Woods Hole Oceanographic Institution
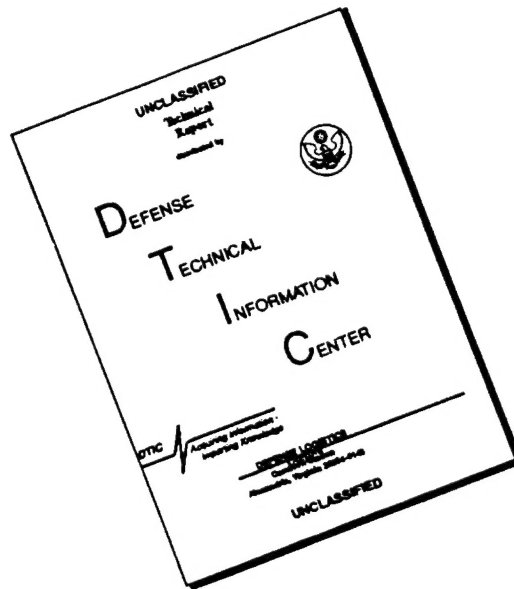Woods Hole, MA 02543

19961030 092

December 15, 1993

DISCLAIMER NOTICE

M96-09-3202

PLEASE CHECK THE APPROPRIATE BLOCK BELOW:

☑ _____1_____ copies are being forwarded. Indicate whether Statement A, B, C, D, E, F, or X applies.

☑ DISTRIBUTION STATEMENT A:
APPROVED FOR PUBLIC RELEASE: DISTRIBUTION IS UNLIMITED

☐ DISTRIBUTION STATEMENT B:
DISTRIBUTION AUTHORIZED TO U.S. GOVERNMENT AGENCIES ONLY; (Indicate Reason and Date). OTHER REQUESTS FOR THIS DOCUMENT SHALL BE REFERRED TO (Indicate Controlling DoD Office).

☐ DISTRIBUTION STATEMENT C:
DISTRIBUTION AUTHORIZED TO U.S. GOVERNMENT AGENCIES AND THEIR CONTRACTORS; (Indicate Reason and Date). OTHER REQUESTS FOR THIS DOCUMENT SHALL BE REFERRED TO (Indicate Controlling DoD Office).

☐ DISTRIBUTION STATEMENT D:
DISTRIBUTION AUTHORIZED TO DOD AND U.S. DOD CONTRACTORS ONLY; (Indicate Reason and Date). OTHER REQUESTS SHALL BE REFERRED TO (Indicate Controlling DoD Office).

☐ DISTRIBUTION STATEMENT E:
DISTRIBUTION AUTHORIZED TO DOD COMPONENTS ONLY; (Indicate Reason and Date). OTHER REQUESTS SHALL BE REFERRED TO (Indicate Controlling DoD Office).

☐ DISTRIBUTION STATEMENT F:
FURTHER DISSEMINATION ONLY AS DIRECTED BY (Indicate Controlling DoD Office and Date) or HIGHER DOD AUTHORITY.

☐ DISTRIBUTION STATEMENT X:
DISTRIBUTION AUTHORIZED TO U.S. GOVERNMENT AGENCIES AND PRIVATE INDIVIDUALS OR ENTERPRISES ELIGIBLE TO OBTAIN EXPORT-CONTROLLED TECHNICAL DATA IN ACCORDANCE WITH DOD DIRECTIVE 5230.25, WITHHOLDING OF UNCLASSIFIED TECHNICAL DATA FROM PUBLIC DISCLOSURE, 6 Nov 1984 (Indicate date of determination). CONTROLLING DOD OFFICE IS (Indicate Controlling DoD Office).

☐ This document was previously forwarded to DTIC on _____ (date) and the AD number is _____.

☐ In accordance with the provisions of DoD instructions, the document requested is not supplied because:

☐ It is TOP SECRET.

☐ It is excepted in accordance with DoD instructions pertaining to communications and electronic intelligence.

☐ It is a registered publication.

☐ It is a contract or grant proposal, or an order.

☐ It will be published t a later date. (Enter approximate date, if known.)

☐ Other. (Give Reason.)

Lori M. Mahoney
Print or Typed Name

_508.389.8850_
Telephone Number

Lori M. Mahoney
Authorized Signature Date

Table of Contents

I. PROJECT SUMMARY

This report presents results from cable dynamic studies that were performed in support of the design of acoustic arrays for the High Gain Program. The studies were confined to two specific areas: 1) The dynamic response of cables under low tension, and 2) The prediction of vortex-induced vibrations of long cables in a shear current.

The research was carried out both at Woods Hole Oceanographic Institution (WHOI) and Massachusetts Institute of Technology (MIT). The work on low tension cables was performed by Professor Michael Triantafyllou (MIT) and Dr. Christopher Howell (WHOI and MIT). The work on vortex induced vibrations was by performed by Dr. Mark Grosenbaugh (WHOI), Professor Triantafyllou, and Dr. Ram Gopalkrishnan (WHOI and MIT).

1.1 Low Tension Cables

Dynamics of low-tension cables are important for understanding the response of arrays that lay-over in a current at 45 degrees. Such an array that behaves like "blades of grass" in a current was put forth hypothetically to address the problem of increasing horizontal resolution. However, at the time the idea was put forth, there existed no comprehensive way of analyzing the dynamics of such a system because of the array cables would be under low tension.

There are many applications, besides the low-tension High Gain arrays, where it is desirable to have cables under very low tension. Some other examples are drifting buoys with hanging instrument arrays, tethers of remotely operated underwater vehicles, and towed acoustic arrays during sharp maneuvers. All of these cases require special analytical techniques because of numerical singularities that arise when the tension is nearly zero.

The work described in §2-6 develops the special numerical techniques for analyzing the dynamics of systems that use low-tension cables (Howell, 1992). The analysis begins with the derivation of the fully nonlinear three-dimensional cable equations that include the effects of bending and torsion. The terms that model the bending stiffness and torsional stiffness are key to removing the singularities due to zero tension.

Two novel schemes are presented in §3 for numerically solving the cable equations. These schemes are developed with low-tension applications in mind.

In §4, we consider the problem of a cable under zero initial tension subject to an impulsive load to gain a better understanding of fundamental mechanisms of cable response intrinsic to low-tension behavior. Equations of cable motion under impulsive loading are derived and solutions are presented for a variety of initial configurations.

The transition between high-tension and low-tension regimes is studied in §5 by considering the dynamics of an inextensible chain hanging freely under its own weight and driven harmonically at the top. The high-tension regime is near the top boundary and the low-tension regime is near the free end.

Finally in §6, the effects of elasticity are incorporated into the cable equations, and the transition between inextensible and extensible behavior is analyzed. This last area of research is important for analyzing the behavior of synthetic cables which can undergo large amounts of extension without breaking. Proper modeling of extensibility is important from the standpoint of impulsive or "snap" loading. For low tensions, a cable behaves as if it is inextensible. However as the dynamic tension grows, there is a transition at which the cable begins to elongate. How this transition affects the overall dynamics must be captured in the

1

model in order to predict the proper dynamic response. This is especially true for synthetic cables which go quickly from being inextensible to a condition of extreme elongation. It is this lack of clear understanding of extensibility that forces the Navy to require a very large safety factor in the use of synthetic rope.

1.2 Vortex Induced Vibrations

The work presented in §7-9 on vortex induced vibrations gives techniques for determining drag coefficients and vibration amplitudes of long marine cables in shear currents. These methods provide a powerful tool which engineers can use to calculate the vibrational loads and fatigue life for specific configurations of High Gain arrays.

The extremely large aspect ratio and flexible nature of long marine cables make them particularly susceptible to vortex-induced vibrations. From both design and operational points of view, it is important to be able to predict the forces (primarily the drag) acting on the cable, as well as its resultant configuration and motions. Although a value of 1.2 is widely accepted as the mean drag coefficient C_{D_m} for the case of flow normal to a stationary circular cylinder, it is also well known that any motion of the cylinder can significantly alter the flow pattern and amplify the vortex-induced forces. In the case of marine cables, this means that the selection of the proper drag coefficient remains a contentious issue. Even with the fuzzy fairing, there is vortex induced vibrations and amplification of the drag coefficient.

Analysis of vortex-induced vibrations of marine cables is an area of research that lacks predictive tools. Past analyses of vortex induced vibrations have depended on stochastic models to describe the strumming process (Vandiver, 1988). These methods are able to fit full-scale experimental data by choosing the correct values of random-model parameters. However, we must emphasize that, without full-scale experiments, it is very difficult with this method to choose the correct values for the parameters.

Our techniques are deterministic. We explain vortex-induced vibrations by considering an infinitely long cable which has no natural modes - so that each point on the cable responds at the local vortex shedding frequency (Triantafyllou & Grosenbaugh, 1994). The cable acts as a wave guide and combines nearby responses into the overall amplitude signal. Laboratory measurements act as the input into the model and provide the sectional lift coefficients as a function of amplitude, frequency, and modulation frequency (Gopalkrishnan, Grosenbaugh, & Triantafyllou, 1991).

In §7, we develop a unified model for hydrodynamic excitation and damping in vortex induced vibrations. In §8, the unified model for the fluid forces is then incorporated into our deterministic model for predicting vortex induced vibrations of marine cables in a shear current. The SAIC array cable with fuzzy fairing is analyzed in §9. We present laboratory measurements of a 0.6-meter section of the cable and show how those can be used, with our deterministic model, to predict the vibration amplitude and drag coefficient.

1.3 Final Comment

The work on low tension cables and vortex induced vibrations, begun in the High-Gain program, continues at WHOI and MIT. The main thrusts are to look at the interaction between transverse and elastic modes in synthetic cables. Here, the principle tool for analysis is our numerical model for three-dimensional cable dynamics that includes the effects of

bending, torsion, and extensibility. In the area of vortex-induced vibrations, we are combining our hydrodynamic damping model, described in §9, with the cable model. This will produce a powerful simulation for modeling vortex induced vibrations of synthetic cables.

II. THREE-DIMENSIONAL LOW-TENSION CABLE EQUATIONS

2.1 Introduction

In this section, the dynamic equations which form the basis of the mathematical model of the cable are derived. The three-dimensional cable equations of motion were derived in cartesian coordinates by Routh (1955) in 1860. Derivations of these equations in so-called natural or lagrangian coordinates, fixed on the cable, have also been done by many authors, including Bliek (1984). The equations derived here extend from those presented by other authors who address cable dynamics in that forces in bending are retained. As a result, the equations presented herein constitute a more accurate model for problems in which the cable tension is small, and therefore are applicable for a wider range of tension magnitudes than previous derivations. It should be noted that Love (1927), and then Landau and Lifshitz (1959), formulated, in cartesian coordinates, fundamentally similar equations by considering the dynamics of thin rods.

Several coordinate systems can be used to study cable dynamics. A lagrangian coordinate system has two primary advantages over a fixed cartesian reference frame. First, it is more straight-forward to describe the hydrodynamic forces in body-fixed coordinates and secondly, results are more easily interpreted. Therefore, we adopt a lagrangian approach herein and, as such, the coordinate system is moving in space and time.

2.2 Kinematics in 3-D

We consider the cable as a single curvilinear line. Let s denote the unstretched lagrangian coordinate along the cable, measured from the origin of the coordinate system to a material point on the cable. The origin is chosen to coincide with a boundary, such as the free end of a towed array, and is denoted as $s = 0$. The other endpoint is denoted as $s = L$, where L is the unstretched cable length.

The cable is considered to be extensible and as such we define $p(t, s)$ as the stretched distance to the same material point s, at a time t. The change in length due to elasticity is given by the strain e. We define the longitudinal strain as

$$e = \lim_{\delta s \to 0} \frac{\delta p - \delta s}{\delta s} = \frac{dp}{ds} - 1$$

where δs is the unstretched length of an incremental segment and δp is the stretched length. The cable cross-sectional area is also altered due to elongation. Following Goodman and Breslin (1976) we make the assumption that the cable has Poisson's ratio $\frac{1}{2}$, i.e. the volume of the cable is preserved after stretching (Timoshenko,1934). This value is correct for synthetic materials. Metallic cables have a Poisson ratio closer to $\frac{1}{3}$, so this constitutes an approximation. Also, many wire and synthetic cables have a far more complex structure, and there response involves relative motion between filaments as well as extension. Therefore the chosen value is meant in an average, equivalent sense. As such, if we assume that the cable is of circular cross-section we can express the change in the cable diameter d due to stretching as

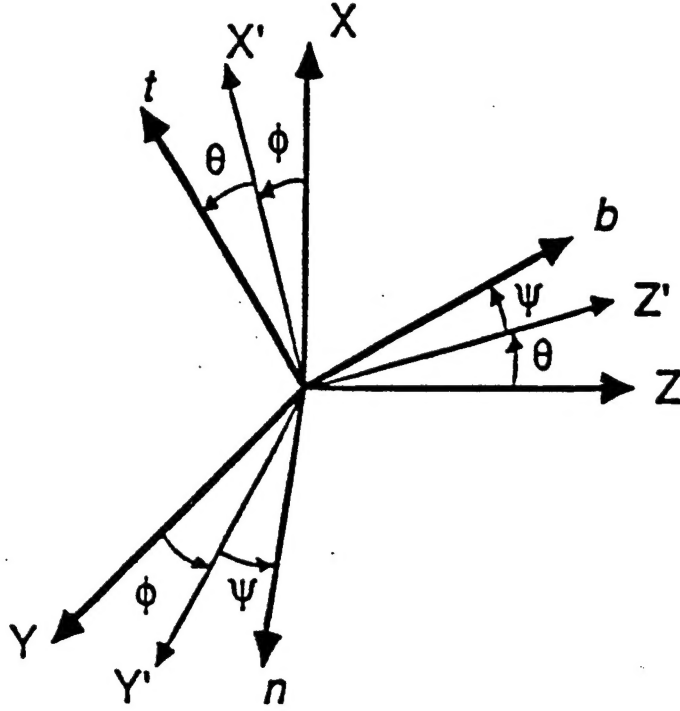$$d = d_s(1 + e)^{\frac{1}{2}} \tag{2.1}$$

4

Figure 2.1: Coordinate systems and Euler rotation sequence.

Note that here we have used the subscript s to denote a parameter in a stretched condition.

The coordinate system is resolved into the tangent, normal, and binormal directions, given by the unit vectors $\hat{t}$, $\hat{n}$, and $\hat{b}$, respectively. The tangential direction is defined as tangent to the cable axis, pointing in the direction of increasing s. The normal direction is perpendicular to $\hat{t}$ and the binormal direction is defined such that the system of vectors $(\hat{t}, \hat{n}, \hat{b})$ is orthogonal and right-handed.

The transformation between the lagrangian coordinates x, y, and z and the fixed coordinates X, Y, and Z is accomplished through a set of rotations known as Euler angles. The particular choice of Euler angles is arbitrary in the sense that any rotation sequence that provides a unique one-to-one transformation between points in the fixed and moving coordinate systems is valid. For the sake of generality, when possible equations will be expressed in a form which is independent of the Euler rotations chosen.

The following rotation sequence has been chosen for this analysis. First, a rotation about the Z axis by the angle ϕ is performed. Next, a rotation about the resulting Y' axis by the angle θ is made to bring the X' axis in line with the tangent direction. Finally, a rotation about the Z' axis by the angle ψ is conducted to fix the orientation of the normal and binormal directions. This rotation sequence is shown in figure 2.1.

These rotations can be expressed in matrix form as follows:

$$\begin{bmatrix} x \\ y \\ z \end{bmatrix} = \Gamma \begin{bmatrix} X \\ Y \\ Z \end{bmatrix}$$

where

5

$$\boldsymbol{\Gamma} = \begin{bmatrix} \cos\phi\cos\theta & \sin\phi\cos\theta & -\sin\theta \\ \cos\phi\sin\theta\sin\psi - \sin\phi\cos\psi & \sin\phi\sin\theta\sin\psi + \cos\phi\cos\psi & \cos\theta\sin\psi \\ \cos\phi\sin\theta\cos\psi + \sin\phi\sin\psi & \sin\phi\sin\theta\cos\psi - \cos\phi\sin\psi & \cos\theta\cos\psi \end{bmatrix}$$

It should be noted that it is possible to more formally define the normal direction using the so-called principal directions (Hildebrand, 1976), as done by Bliek (1984). The formulation presented here was selected because it is more general when material torsion is involved, and provides greater flexibility in deriving and expressing forces in bending. However, because Frenet's formulas are not applicable to this coordinate system, an additional constraint must be imposed to formally define the orientation of the normal and binormal directions. This constraint will be addressed in the discussion of torsional effects.

Expressions for the time and spatial derivatives are complicated to some degree by the selection of a lagrangian coordinate system. This is due to the fact that in addition to the evolution of the vector quantity of interest, the coordinate system itself also varies in time and space. This can be shown for the arbitrary vector $\vec{G}(t, s)$. Herein we employ the subscript notation $(1, 2, 3)$ to denote the variables in the $(\hat{t}, \hat{n}, \hat{b})$ directions, respectively and express $\vec{G}$ as follows:

$$\vec{G} = G_1\hat{t} + G_2\hat{n} + G_3\hat{b}. \tag{2.2}$$

First consider the time variation of $\vec{G}$. Expanding the expression for the time derivative gives

$$\frac{D\vec{G}}{Dt} = \frac{\partial \vec{G}}{\partial t} + G_1\frac{\partial \hat{t}}{\partial t} + G_2\frac{\partial \hat{n}}{\partial t} + G_3\frac{\partial \hat{b}}{\partial t}. \tag{2.3}$$

This expression for the so-called substantial or material derivative can be expressed as

$$\frac{D\vec{G}}{Dt} = \frac{\partial \vec{G}}{\partial t} + \vec{\omega} \times \vec{G}, \tag{2.4}$$

where $\vec{\omega}$ is the angular velocity vector. Physically, this vector represents the time rate change of the local coordinate system about the x, y, and z axes. The angular velocity vector is expressed as follows:

$$\vec{\omega} = \omega_1\hat{t} + \omega_2\hat{n} + \omega_3\hat{b} \tag{2.5}$$

where, in terms of the selected Euler angles

$$\omega_1 = \frac{\partial \psi}{\partial t} - \frac{\partial \phi}{\partial t}\sin\theta$$

$$\omega_2 = \frac{\partial \theta}{\partial t}\cos\psi + \frac{\partial \phi}{\partial t}\cos\theta\sin\psi$$

$$\omega_3 = \frac{\partial \phi}{\partial t}\cos\theta\cos\psi - \frac{\partial \theta}{\partial t}\sin\psi.$$

The evaluation of changes in space follows along similar lines and is given by

$$\frac{D\vec{G}}{Ds} = \frac{\partial \vec{G}}{\partial s} + \vec{\Omega} \times \vec{G} \tag{2.6}$$

where

$$\vec{\Omega} = \Omega_1\hat{t} + \Omega_2\hat{n} + \Omega_3\hat{b}. \tag{2.7}$$
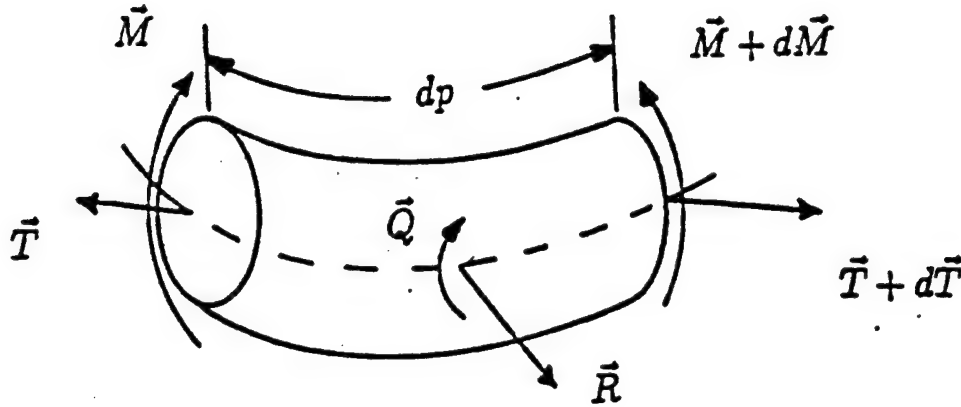
Figure 2.2: Incremental cable segment.

The vector $\vec{\Omega}$ represents the local curvature of the cable, at the point s, about the local coordinate system and is expressed in component form using the Euler angles as

$$
\begin{aligned}
\Omega_1 &= \frac{\partial \psi}{\partial s} - \frac{\partial \phi}{\partial s} \sin \theta \\
\Omega_2 &= \frac{\partial \theta}{\partial s} \cos \psi + \frac{\partial \phi}{\partial s} \cos \theta \sin \psi \\
\Omega_3 &= \frac{\partial \phi}{\partial s} \cos \theta \cos \psi - \frac{\partial \theta}{\partial s} \sin \psi.
\end{aligned}
$$

2.3 Three-Dimensional Governing Equations

2.3.1 DERIVATION OF GOVERNING EQUATIONS

We begin the derivation of the governing equations by considering a small cable segment of unstretched length ds and stretched length of dp, as shown in figure 2.2. The velocity and internal force vectors, $\vec{V}$ and $\vec{T}$, respectively are defined as follows:

$$
\begin{aligned}
\vec{V} &= v_1 \hat{t} + v_2 \hat{n} + v_3 \hat{b} \\
\vec{T} &= T_1 \hat{t} + T_2 \hat{n} + T_3 \hat{b}.
\end{aligned} \tag{2.8}
$$

Here T_1 denotes the tension force while T_2 and T_3 represent shear forces. We define $\vec{R}$ as the distributed forces per unit length and m as the unstretched mass per unit length. Conservation of mass dictates that

$$
m_s dp = m ds. \tag{2.9}
$$

7

Applying Newton's law to the cable segment, along with the conservation of mass yields

$$m\frac{D\vec{V}}{Dt} = \frac{D\vec{T}}{Ds} + \sum \vec{R}(1+e).$$

(2.10)

We expand the material derivatives in local coordinates to yield

$$m(\frac{\partial \vec{V}}{\partial t} + \vec{\omega} \times \vec{V}) = \frac{\partial \vec{T}}{\partial s} + \vec{\Omega} \times \vec{T} + \sum \vec{R}(1+e).$$

(2.11)

As mentioned, we seek to incorporate internal forces due to bending and torsional stiffness in the cable. As such we must balance the moments imposed on the incremental cable segment in figure 2.2. Here we define $\vec{M}$ and $\vec{Q}$ as the internal and distributed moment vectors. We define the following unstretched quantities: Young's modulus E; shear modulus G; cable density ρ_c; sectional second moment I; and polar moment I_p.

The unstretched internal moment vector is expressed as

$$\vec{M} = M_1\hat{t} + M_2\hat{n} + M_3\hat{b}$$

(2.12)

where, assuming the cable is a circular, homogeneous cylinder,

$$\begin{aligned} M_1 &= GI_p\Omega_1 \\ M_2 &= EI\Omega_2 \\ M_3 &= EI\Omega_3. \end{aligned}$$

(2.13)

It should be noted that in (2.13) Ω_1 represents the material torsion which, in general, is different than the geometric torsion. In addition, the mass moment of inertia per unit length matrix $\rho_c\mathbf{I}$, for a homogeneous cylinder of circular cross-section, is defined as

$$\rho_c\mathbf{I} = \begin{bmatrix} I_p & 0 & 0 \\ 0 & I & 0 \\ 0 & 0 & I \end{bmatrix}$$

Using equation 2.1, the following relations are found between stretched and unstretched quantities:

$$\begin{aligned} \vec{M} &= \vec{M}_s(1+e)^2 \\ \rho_c\mathbf{I} &= \rho_c\mathbf{I}_s(1+e)^2. \end{aligned}$$

Taking moments about the left-hand side of the cable segment and expressing the results in terms of unstretched quantities yields:

$$\frac{D}{Dt}\left[\frac{\rho_c\mathbf{I}\vec{\omega}}{(1+e)}\right] = \frac{D}{Ds}\left[\frac{\vec{M}}{(1+e)^2}\right] + \vec{Q}(1+e) + \vec{dr} \times \vec{R}(1+e) + \frac{\vec{dr}}{ds} \times \vec{T}.$$

(2.14)

In the limit that $\vec{dr} \to 0$ we find the following:

$$\begin{aligned} \vec{dr} \times \vec{R} &\to 0 \\ \frac{1}{(1+e)}\frac{\vec{dr}}{ds} &\to \hat{t}. \end{aligned}$$

8

It is unlikely that distributed moment forces will arise in the types of problems addressed in this study. As such, this term will not be retained. Applying these simplifications to equation 2.14 provides the set of moment balance equations given below.

$$\frac{D}{Dt}\left[\frac{\rho_c \mathbf{I}\vec{\omega}}{(1+e)}\right] = \frac{D}{Ds}\left[\frac{\vec{M}}{(1+e)^2}\right] + \hat{t} \times \vec{T}(1+e) \qquad (2.15)$$

The applied forces acting on the cable are located on the right-hand side of equation 2.10. These forces include the internal forces due to tension and shear, as well as external loads. The external loads will be considered in detail in §2.4.

2.3.2 SIMPLIFICATION OF GOVERNING EQUATIONS

Before expressing the governing equations in final form, we attempt to simplify the equations by identifying terms which can be neglected. This will be accomplished by conducting a nondimensional analysis of equations 2.10 and 2.15. Nondimensional terms will be denoted subscript n.

We begin by defining the following nondimensional quantities:

$$
\begin{aligned}
t_n &= t\sqrt{\frac{g}{L}} \\
\vec{\omega}_n &= \vec{\omega}\sqrt{\frac{L}{g}} \\
s_n &= \frac{s}{L} \\
\vec{\Omega}_n &= \vec{\Omega}L \\
\vec{V}_n &= \frac{\vec{V}}{\sqrt{gL}}.
\end{aligned}
$$

Substitution of these nondimensional quantities into equation 2.10 yields

$$m\frac{D\vec{V}_n}{Dt_n} = \frac{1}{mgL}\frac{D\vec{T}}{Ds_n} + \frac{1}{mg}\sum \vec{R}(1+e) \qquad (2.16)$$

Based on this we define the nondimensional force vectors $\vec{T}_n$ and $\vec{R}_n$ as

$$
\begin{aligned}
\vec{T}_n &= \frac{\vec{T}}{mgL} \\
\vec{R}_n &= \frac{\vec{R}}{mg}
\end{aligned}
$$

Introducing the previously defined nondimensional quantities into equation 2.15 and neglecting the strain terms associated with the inertial forces yields:

$$(1+e)^2\frac{\rho_c I g}{L}\frac{D\vec{\omega}_n}{Dt_n} \simeq \frac{EI}{L^2}\left(\frac{D\vec{\Omega}_n}{Ds_n} - \frac{2}{(1+e)}\frac{\partial e}{\partial s_n}\right) + \hat{t} \times \vec{T}_n mgL(1+e)^3 \qquad (2.17)$$

Here we have assumed that GI_p is on the order of EI. Rearranging terms, we write the nondimensional equations in bending.

9

$$\hat{t} \times \vec{T_n}(1+e)^3 \simeq -\beta_1 \frac{D\vec{\Omega}_n}{Ds_n} + \beta_2 \frac{D\vec{\omega}_n}{Dt_n}(1+e)^2 + 2\beta_1 \frac{\partial e}{\partial s_n} \qquad (2.18)$$

where

$$\beta_1 = \frac{EI}{mgL^3}$$
$$\beta_2 = \frac{\rho_c I}{mL^2}.$$

In order to determine the relative importance of the variations in strain, we further investigate the last term on the right-hand side. Assuming a linear stress-strain relation is applicable, we write

$$e = \frac{T}{EA}. \qquad (2.19)$$

Using this relation we find

$$\frac{EI}{mgL^3} \frac{\partial e}{\partial s_n} = \frac{I}{AL^2} \frac{\partial T_n}{\partial s_n} \simeq \frac{d^2}{L^2} \frac{\partial T_n}{\partial s_n}. \qquad (2.20)$$

The diameter to length ratio is typically very small. Therefore, based on (2.20) we will neglect this term.

To compare the relative significance of the bending stiffness term β_1 and the rotational inertia term β_2 we examine their ratio,

$$\frac{\beta_2}{\beta_1} = \frac{g\rho_c L}{E}. \qquad (2.21)$$

For steel cables, this ratio is on the order of $10^{-6}L$ meters. For synthetic cables this ratio may be slightly larger. We should still be justified, however, to neglect the rotational inertia terms. As such, rotational inertia terms will not be retained.

Next we consider forces in torsion. Neglecting the rotational inertia term in the moment balance equation about the tangential direction yields

$$GI_p \frac{\partial \Omega_1}{\partial s} = 0 \qquad (2.22)$$

Equation 2.22 simply states that the torsional rigidity remains constant throughout the cable span. In the absence of applied end moments, as is typically the case for torque balanced cables, therefore, the effect of torsion is zero. If end moments are present, i.e. a torque unbalanced cable is considered, the material torsion Ω_1 is constant along the cable span and, therefore, a constant torque is applied over the entire cable length.

Equation 2.22 can be satisfied in one of two ways. First, torsion effects can be neglected either on the basis that $\beta_1 \ll 1$ or because end moments in torsion are not present. The second approach is to calculate Ω_1 from the boundary conditions, and then impose $\Omega_1 = C(t)$ along the span, where $C(t)$ is a time varying constant.

Herein we adopt the first approach and assume that the torsional stiffness is negligible. As a result, a new equation must be chosen to replace equation 2.22. The purpose of the new equation is to fix the orientation of the local coordinate system about the tangential direction. This is an arbitrary selection because the governing equations apply regardless of the orientation of the normal and binormal directions.

For simplicity we specify the orientation of the local coordinate system by setting $\psi = 0$. This simplifies the analysis by removing one variable from the equations.

With this simplification the angular velocity and rotation vectors reduce to the following:

$$\omega_1 = -\frac{\partial \phi}{\partial t} \sin \theta$$

$$\omega_2 = \frac{\partial \theta}{\partial t}$$

$$\omega_3 = \frac{\partial \phi}{\partial t} \cos \theta$$

and

$$\Omega_1 = -\frac{\partial \phi}{\partial s} \sin \theta$$

$$\Omega_2 = \frac{\partial \theta}{\partial s}$$

$$\Omega_3 = \frac{\partial \phi}{\partial s} \cos \theta.$$

Proceeding further, we examine the significance of the shear forces T_2 and T_3. Using the simplifications discussed earlier, we find the following nondimensional relations for the shear forces:

$$T_{2n} = \beta_1 (\Omega_{1n} \Omega_{2n} - \frac{\partial \Omega_{3n}}{\partial s_n})$$

$$T_{3n} = -\beta_1 (\Omega_{1n} \Omega_{3n} + \frac{\partial \Omega_{2n}}{\partial s_n}).$$

Therefore, the shear forces are of order $O(\beta_1)$. This is an important result that provides information as to when shear forces are negligible. In particular, we find that shear stresses are inversely proportional to L^3, provided the radius of curvature is of order $O(L)$. For moderate to large tension magnitudes, tensile forces prevent the cable from developing substantial variations in curvature. Therefore, if the cable tension T_{1n} is of order $O(1)$ and the cable is very long, it is valid to neglect bending stiffness. However, if the tension is small, the cable can develop substantial curvature and shear forces must be retained.

An alternative means for investigating the significance of bending forces is to consider the induced strains. For simplicity we consider a two-dimensional configuration. Let e_T denote the strain induced by tension, i.e. $T_1 = EAe_T$, and e_c the strain induced by curvature. For a radius of curvature a, the maximum strain due to curvature is given by $e_{cm} = r/a$, where r is the radius of the cable cross-section. If we consider the case where e_{cm} is of the order of e_T, then the binormal bending moment, M_b, is given by $M_b = EI/a \simeq T_1 I/(Ar)$. For cables of circular cross-section, $I = (\pi r^4)/4$. Therefore, we find

$$M \simeq \frac{T_1 r}{4} \tag{2.23}$$

Neglecting rotational inertia effects, the binormal shear force S_b is obtained as

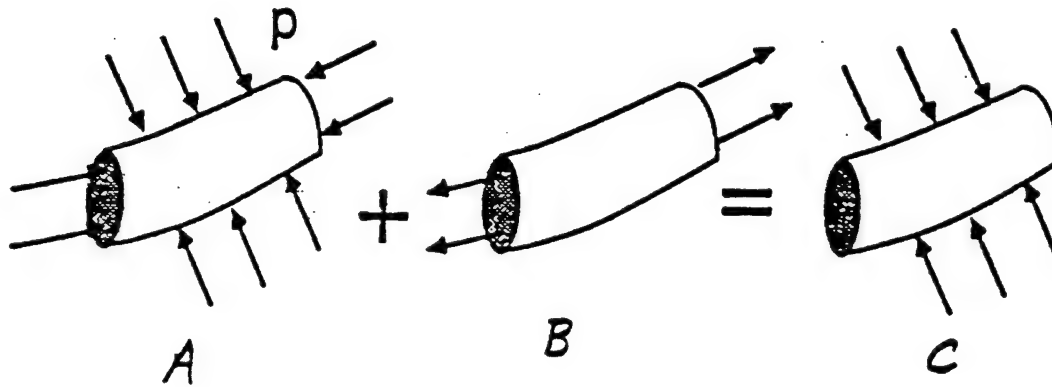$$S_b = \frac{dM_b}{ds} \simeq \frac{T_1 r}{4 l_c} \tag{2.24}$$

Figure 2.3: Superposition of forces to account for end effects.

where l_c is the characteristic length of change of the bending moment. Therefore, only if l_c is of order r, a situation which is not physically realistic, will the shear forces be of the same order of magnitude as that of T_1, in this case.

As a result, we can conclude that forces in bending are significant only if the strains they induce are greater than those induced by tension, a situation which can occur in applications involving low tension.

2.4 Applied Forces

The external forces acting on the cable include the cable weight, buoyancy, and the hydrodynamic forces of drag and added mass. Each of these forces will be addressed separately. Note that all forces discussed here are per unit stretched length.

2.4.1 CABLE WEIGHT AND BUOYANCY FORCES

Despite the seeming simplicity of static weight and buoyancy forces, a large number of papers have been written on the proper way to express these forces mathematically (Sparks, 1984). To understand why this has occurred we must first return to basic principles. Archimede's principle states that the net buoyancy force on a body *completely enclosed* in a fluid is equal to the weight of the fluid displaced by the body. The cable segment shown in figure 2.2 is attached to adjoining cable on both ends and is therefore not completely enclosed in fluid.

To account for this condition at the end points, we superimpose forces as shown in figure 2.3. Because segment A is completely enclosed, we can write the buoyancy force F_B as

$$F_B = g\rho_w A_s \tag{2.25}$$

12

where g is the gravitational constant. According to equation 2.1, this expression can be rewritten as

$$F_B(1 + e) = g\rho_w A. \tag{2.26}$$

Subtracting the buoyancy force from the cable self weight we find an expression for w, the submerged cable weight/unit length, given as

$$w_o = (m - \rho_w A)g. \tag{2.27}$$

This force acts in the direction of the gravity vector $(-\hat{i})$ and as such we write the final expression for the forces due to the submerged cable weight

$$\vec{R}_w(1 + e) = -w_o\hat{i} = w_o(n_1\hat{t} + n_2\hat{n} + n_3\hat{b}) \tag{2.28}$$

where, in terms of the selected Euler angles

$$
\begin{aligned}
n_1 &= -\cos\phi\cos\theta \\
n_2 &= \sin\phi \\
n_3 &= -\cos\phi\sin\theta.
\end{aligned}
$$

Now we must consider the end point forces in segment B. These forces act in the axial direction only and therefore can be lumped together with the internal tension. Following Goodman and Breslin (1976), we define the "effective tension", in terms the internal tension and the hydrostatic pressure P, as

$$T_{1e} = T_1 + \frac{PA}{(1 + e)}. \tag{2.29}$$

In this manner, the form of the governing equations remains unchanged in water or air. Henceforth, to simplify the expressions, T_1 is defined as the effective tension and the subscript e will be dropped.

2.4.2 HYDRODYNAMIC FORCES

Determining mathematical expressions that accurately model the fluid-structure interaction forces acting on the cable is extremely complex, especially if the effects of vortex shedding are incorporated. Therefore, it is not surprising that a large portion of hydrodynamic research is focussed in this area.

In addition to the hydrodynamic forces that arise from the cable motion itself, we seek to incorporate fluid loads due to current. To this end we define J_j as the current velocity in the jth direction. Transformation between known current magnitudes in a fixed coordinate system to local coordinates is accomplished through the transformation matrix Γ.

Herein we adopt the semi-empirical Morison type approach for modeling hydrodynamic loads (Sarpkaya and Isaacson, 1981). In this manner the fluid loads are decomposed into one component in phase with the fluid velocity (drag) and one component in phase with the fluid acceleration (added mass).

To calculate the hydrodynamic drag force, the fluid velocity field is first decomposed into tangent, normal, and binormal components. Denoting the relative velocities with a subscript r, we can write

13

$$
\begin{aligned}
v_{1r} &= v_1 - J_1 \\
v_{2r} &= v_2 - J_2 \\
v_{3r} &= v_3 - J_3
\end{aligned}
$$

Using Morison's approximation and denoting C_{dj} as the drag coefficient in the jth direction, the drag forces are expressed as follows:

$$
\vec{R}_d(1 + e) = R_{d1}\hat{t} + R_{d2}\hat{n} + R_{d3}\hat{b} \tag{2.30}
$$

where

$$
R_{d1} = -\frac{1}{2}\rho_w d\pi C_{d1} v_{1r}|v_{1r}|(1+e)^{\frac{1}{2}} \tag{2.31}
$$

$$
R_{d2} = -\frac{1}{2}\rho_w d C_{d2} v_{2r}|v_{2r}^2 + v_{3r}^2|^{\frac{1}{2}}(1+e)^{\frac{1}{2}} \tag{2.32}
$$

$$
R_{d3} = -\frac{1}{2}\rho_w d C_{d3} v_{3r}|v_{2r}^2 + v_{3r}^2|^{\frac{1}{2}}(1+e)^{\frac{1}{2}}. \tag{2.33}
$$

Needless to say, accurate values for the drag coefficients are required for accurate solutions. This is not a simple matter with complications arising, for example, from changes in surface roughness and the onset of vortex shedding. As a result, determining drag coefficients has been and continues to be an active area of research. For additional information on drag coefficients consult (Sarpkaya and Isaacson, 1981).

Hydrodynamic forces in phase with the fluid acceleration are often called the added mass forces. Added mass forces are one of the most frequently misunderstood concepts in hydrodynamics, especially for investigators who study cable problems. In basic terms, when a body immersed in a fluid is accelerated, the surrounding fluid must be displaced and therefore is also accelerated to some degree. The additional inertia force required to displace the fluid is known as the added mass force (Newman, 1977). According to this definition, the added mass force can only act in a direction normal to the cable and is independent of viscosity. Lighthill (1960) has shown that strip theory is an acceptable means of calculating added mass forces for cables.

We express the added mass force in terms of the relative accelerations of the fluid, normal to the cable, and an added mass coefficient m_a.

$$
\vec{R}_a(1 + e) = -m_a\frac{\partial v_{2r}}{\partial t}\hat{n} - m_a\frac{\partial v_{3r}}{\partial t}\hat{b} \tag{2.34}
$$

As with the drag coefficients, the evaluation of m_a is difficult. Generally, for cable problems, the following expression is used
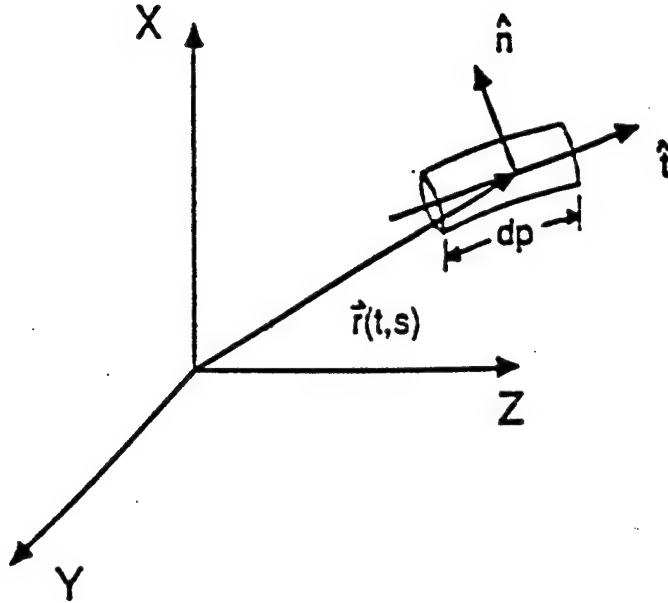
$$
m_a = \frac{\pi}{4}\rho_w d^2 \tag{2.35}
$$

14

Figure 2.4: Description of location vector $\vec{r}(t, p)$.

2.5 Compatibility Relations

The governing equations as derived are valid for an incremental cable segment. As such, compatibility relations which relate the cable velocities, orientation, and strain are required to ensure compatibility between adjoining cable segments. In the absence of strain, a simple physical interpretation of these relations is that they preserve the cable length.

We define $\vec{r}(t, p)$ as the vector from the origin of a fixed coordinate system to a point on the cable, as shown in figure 2.4. In deriving the compatibility relations we assume that the cable shape is sufficiently smooth. For this to be valid, $\vec{r}(t, p)$ and its derivatives must be continuous functions of p (or s) and t. This assumption was implicitly assumed in the derivation of the governing equations as well. This is an important requirement which may not hold for the particular case of a chain under zero tension. When tension is lost in the chain, a restoring force which prevents the chain from forming discontinuous slope does not exist because chains, unlike cables have no bending stiffness. This topic is addressed further in §5.

In the absence of discontinuities in the cable shape, we can use the property of continuous functions of two variables (Hildebrand, 1976) and write

$$\frac{D}{Dt}\left[\frac{D\vec{r}}{Ds}\right] = \frac{D}{Ds}\left[\frac{D\vec{r}}{Dt}\right]. \tag{2.36}$$

According to the definitions of the tangent and velocity vectors (Hildebrand, 1976)

$$\vec{V} = \frac{D\vec{r}}{Dt} \tag{2.37}$$

15

$$\hat{t} = \frac{D\vec{r}}{Dp} = \frac{1}{(1+e)}\frac{D\vec{r}}{Ds}$$

Substitution of 2.37 into 2.36 provides the compatibility relations in vector form

$$\frac{D}{Dt}[(1+e)\hat{t}] = \frac{D\vec{V}}{Ds}. \tag{2.38}$$

This can be expanded to give

$$\frac{\partial e}{\partial t}\hat{t} + (1+e)\vec{\omega} \times \hat{t} = \frac{\partial \vec{V}}{\partial s} + \vec{\Omega} \times \vec{V}. \tag{2.39}$$

2.6 Final Equations

In order to clarify the expressions used in subsequent sections, we eliminate the subscript notation used previously. Here we redefine the velocities (v_1, v_2, v_3) as (u, v, w) and the internal forces (T_1, T_2, T_3) as (T, S_n, S_b), where T denotes the effective tension and S_n and S_b are the normal and binormal shear forces, respectively. In addition we assume a linear stress-strain relation is applicable and write

$$e = \frac{T}{EA} \tag{2.40}$$

where T denotes the effective tension, as defined in (2.29).

In terms of the new variables and the expression for the strain, we can express the equations of motions in their final form.

$$m\left(\frac{\partial u}{\partial t} + w\frac{\partial \theta}{\partial t} - v\frac{\partial \phi}{\partial t}\cos\theta\right) = \frac{\partial T}{\partial s} + S_b\Omega_2 - S_n\Omega_3 + w_o n_1 + R_{d1} \tag{2.41}$$

$$m\left(\frac{\partial v}{\partial t} + \frac{\partial \phi}{\partial t}(u\cos\theta + w\sin\theta)\right) + m_a\frac{\partial v_{2r}}{\partial t} = \frac{\partial S_n}{\partial s} + \Omega_3(T + S_b\tan\theta) + w_o n_2 + R_{d2}$$

$$m\left(\frac{\partial w}{\partial t} - v\frac{\partial \phi}{\partial t}\sin\theta - u\frac{\partial \theta}{\partial t}\right) + m_a\frac{\partial v_{3r}}{\partial t} = \frac{\partial S_b}{\partial s} - S_n\Omega_3\tan\theta - T\Omega_2 + w_o n_3 + R_{d3}$$

$$EI\frac{\partial \Omega_2}{\partial s} = EI\Omega_3^2\tan\theta + S_b(1 + \frac{T}{EA})^3$$

$$EI\frac{\partial \Omega_3}{\partial s} = EI\Omega_2\Omega_3\tan\theta - S_n(1 + \frac{T}{EA})^3$$

$$\frac{\partial u}{\partial s} + \Omega_2 w - \Omega_3 v = \frac{1}{EA}\frac{\partial T}{\partial t}$$

$$\frac{\partial v}{\partial s} + \Omega_3(u + w\tan\theta) = (1 + \frac{T}{EA})\frac{\partial \phi}{\partial t}\cos\theta$$

$$\frac{\partial w}{\partial s} - \Omega_3 v\tan\theta - \Omega_2 u = -(1 + \frac{T}{EA})\frac{\partial \theta}{\partial t}$$

$$\Omega_2 = \frac{\partial \theta}{\partial s}$$

$$\Omega_3 = \frac{\partial \phi}{\partial s}\cos\theta$$

16

2.7 Discussion of Equations of Motion

Of fundamental significance to the study of low tension cables is that the cable governing equations are singular for zero tension if forces in bending are neglected. Dowling (1988) has shown using analytic techniques that when the cable tension is balanced by a fluid loading term, a critical point develops. She found that in order to obtain solutions beyond the critical point, bending stiffness must be incorporated in the boundary layer region near this singularity. In addition, Dowling found that solutions beyond the critical point are influenced by bending stiffness.

The singularity identified by Dowling is associated with cable equations that *neglect* bending stiffness. The more general formulation, given by (2.41), is stable for zero tension.

A physical interpretation of the zero tension singularity is most readily understood by considering the mechanisms by which energy is propagated along the cable. For a perfectly flexible cable, transverse disturbances are propagated at a speed proportional to the $\sqrt{T}$, where T is the instantaneous cable tension (Bliek, 1984). As such, the speed of energy propagation slows considerably in regions of low tension, and energy cannot be transmitted past a critical point of zero tension. As such, energy builds rapidly near the critical point, and the equations become singular. If the point of zero tension coincides with a boundary, i.e. the free end of a hanging chain, energy can be transferred by reflection. For this reason, a zero tension point is permissible at a boundary, provided the boundary is free to reflect energy. Triantafyllou and Triantafyllou (1991) have shown that if the free end of a hanging chain is constrained, the governing equations for a perfectly flexible chain are unsolvable.

An alternative energy mechanism which gains importance as the tension approaches zero is bending stiffness. In this later case, energy is transferred by flexural waves at a speed proportional to $\sqrt{EI}$. In reality, cables do exhibit a finite degree of flexural rigidity, which can serve as the necessary physical mechanism for energy transfer. By contrast chains have no flexural stiffness. They are, however, able to transfer energy by developing rotational inertia in the individual links.

III. NUMERICAL METHODS FOR SOLVING CABLE EQUATIONS

3.1 Introduction

The cable governing equations derived in §2 are nonlinear and strongly coupled. As a result, analytic solutions are unavailable except in simplified cases. Some analytic results are obtainable using asymptotic techniques, as discussed in §5, however, in order to obtain solutions for more general problems, numerical methods must be employed and a number of algorithms have been developed for this purpose.

In this section, we first discuss the previously developed numerical techniques in the area of cable dynamics. In particular we address the limitations of these techniques as they apply to the study of low-tension problems. Also addressed in this section are two recently developed algorithms which were designed to overcome the drawbacks of existing methods. These two algorithms were used extensively to obtain the numerical results discussed in the subsequent sections.

3.2 Previous Numerical Techniques

Several papers have been published which survey existing analytic and numerical techniques used to study cable dynamics. Casarella and Parsons (1970), and then Choo and Casarella (1973), provide comprehensive summaries of the developed methods. However, these papers were written in the early 1970's and recent developments have left these papers somewhat out-dated. Triantafyllou (1991) has recently published a review paper which summarizes many of the advancements that have occurred over the last twenty years.

As mentioned in the introduction, solving the cable governing equations is extremely difficult. These difficulties are principally due to geometric and hydrodynamic nonlinearities. In addition, material nonlinearities may also be present if a linear stress-strain model is not applicable.

To eliminate the nonlinearities, many methods linearize the problem by assuming small deformations from some static configuration. This greatly simplifies the analysis. However, for low-tension problems, large displacements can develop due to the small restoring force, thereby rendering any static configuration meaningless. Also, because the dynamic tension may be equal or greater than the static tension, low-tension problems cannot be simplified by linearizing the tension.

Other assumptions typically made include neglecting inertial forces, bending stiffness, and elasticity. The validity of these assumptions is dependent on the particular analysis in question and the methods therefore are often restricted to a limited class of problems.

In recent years a wide range of numerical techniques have been applied to the study of cable dynamics. The most prevalent methods of approach are finite-difference, finite-element, spectral-method and lumped-parameter models. For separate discussions of these methods see Ablow and Schechter (1983), Delmer et al. (1983), Webster (1975), Burgess (1985), and Kamman and Huston (1985). A detailed comparison between finite element and lumped parameter methods has been published by Leonard and Nath (1981). The method of characteristics has also been used successfully. In particular, Schram and Reyle (1968) used the method to show coupling occurs between transverse and longitudinal disturbances if the shape of the cable is not straight.

A finite-difference approach is most suitable for the low-tension problem. Lumped-parameter and finite-element models require an excessive amount of computer storage and often obscure the underlying physics of the problem. Other authors have determined that finite-element models are not well suited for inherently nonlinear problems, involving large displacements Delmer et al. (1988). Spectral-methods suffer from the limitation that derivative boundary conditions, such as those encountered when incorporating bending stiffness, are often difficult to evaluate.

The finite difference method has been used extensively in the past to model cable problems. Sanders (1982) developed a three-dimensional algorithm in which finite-differences are used to discretize the cable and simulations are advanced in time using a Runga-Kutta recurrence scheme (Press et al., 1988). This algorithm suffers from the limitation that inertial forces are neglected. This assumption is not valid for low-tension problems in that inertial forces can be on the same order of magnitude as tensile forces.

Ablow and Schechter (1983) developed a three-dimensional algorithm which includes inertial forces and discretizes the problem in both space and time using finite-differences. The method uses a second-order accurate implicit approximation scheme, commonly known as the box-method (Mitchell and Griffiths, 1980), which is centered in space and time. Milinazzo, Wilkie, and Latchman (1987) improved on the methodology of Ablow and Schechter by developing a better method for treating the zero tension boundary condition at the free end. Burgess (1991) corrected earlier mistakes in these publications by properly accounting for the hydrostatic and added mass forces. In addition, he has incorporated the ability to pay cable out from a ship, as required for cable deployment simulations. However, as with the previous authors, he incorrectly applied the principle of conservation of mass and derived erroneous strain terms in his equations.

An important point to note about these previous formulations is that the algorithms all become unstable if the tension approaches zero anywhere along the interior of the cable, a situation which is likely to occur in low-tension studies. This is a significant drawback of the methods and prevents altogether the study of cables under zero initial tension.

Ablow and Schechter (1983) determined that if the tension vanishes anywhere along the cable, the determinant of their stiffness matrix becomes zero. Because this matrix is inverted within their numerical approximation scheme, the method fails. As noted by Dowling (1988), the singularity encountered by Ablow and Schechter is not an artifact of their numerical scheme; instead it stems from the ommission of flexural stiffness in the dynamic equations. The previously noted finite difference schemes all neglect the effects of bending stiffness and therefore are limited in their application to low-tension problems based on both numerical and physical considerations.

An sidenote to Dowling's work is that her solution is based on the correct form of the linearized transverse momentum equation, first derived by Paidoussis (1973). In two earlier papers by Paidoussis (1966, 1968) a term was incorrectly omitted in this equation, leading Ortloff and Ives (1968), Kennedy (1980), and Kennedy and Strahan (1981) to publish erroneous solutions of the towed array problem.

The limitations of existing algorithms created a need for novel approaches to the low-tension problem. Two alternative numerical methods were developed for this purpose. The first method was primarily developed to treat problems under zero tension initially, such as impulsively loaded cables as discussed in §4. Prior to excitation of the cable, zero tension is permissible, therefore, the failure of previous algorithms in this case stems from the numerical formulation. Within the method, an explicit time integration scheme is used in which the cable tensions are cast as the only unknowns in a matrix problem. Therefore,

the onset of zero tension along the cable does not present a problem computationally. This allows a wider class of initial value problems to be studied.

The second method developed incorporates the effects of bending stiffness in an implicit finite difference formulation, similar to that of Ablow and Schechter. An implicit scheme was selected because the characteristics of the governing equations are altered by including bending stiffness (Watzky, 1992). In §3.4 we show that incorporating bending stiffness eliminates the zero tension singularity. This finding has been shown previously for the two-dimensional case by Howell (1992).

3.3 Explicit Formulation Without Bending Stiffness

Explicit time-domain integration schemes are generally used in conjunction with finite-element and lumped-parameter methods (Chiou, 1989). However, existing finite-difference algorithms use implicit time integrators. The reason is that implicit schemes can be unconditionally stable while explicit schemes are conditionally stable (Leonard and Nath, 1981). In addition, explicit schemes are not well suited for predominantly parabolic equations (Mitchell and Griffiths, 1980). This led Sanders (1982) to question the applicability of explicit schemes in general. However, it is possible to formulate the difference equations so as to retain the hyperbolic characteristics of the governing equations. In addition, by chosing the inextensible form of the cable equations, we can eliminate longitudinal waves. This reduces the stiffness of the equations because longitudinal wave speeds are generally much higher than those for transverse waves. Therefore, an explicit solution scheme is feasible, provided it remains stable. Such a scheme could offer significant advantages over implicit schemes because no iterations are required.

3.3.1 EQUATIONS OF MOTION

We restrict our attention to two-dimensional problems only. The two-dimensional inextensible form of the governing equations and compatibility relations is given by

$$
\begin{aligned}
m\left(\frac{\partial u}{\partial t} - \frac{\partial \phi}{\partial t} v\right) &= \frac{\partial T}{\partial s} - w_o \cos \phi - \frac{1}{2}\rho_w D\pi C_{dt} u_r |u_r| \qquad (3.1) \\
m\left(\frac{\partial v}{\partial t} + \frac{\partial \phi}{\partial t} u\right) + m_a \frac{\partial v_r}{\partial t} &= T\frac{\partial \phi}{\partial s} + w_o \sin \phi - \frac{1}{2}\rho_w D C_{dn} v_r |v_r| \\
\frac{\partial u}{\partial s} - \frac{\partial \phi}{\partial s} v &= 0 \\
\frac{\partial v}{\partial s} + \frac{\partial \phi}{\partial s} u &= \frac{\partial \phi}{\partial t}.
\end{aligned}
$$

These equations describe the mathematical formulation of the problem and form the basis of the numerical approximation scheme. With regard to boundary conditions, we consider the cable to be pinned at one end $(s = L)$, with the tangential and normal velocities prescribed. The other end $(s = 0)$ is considered to be a free boundary and zero tension is imposed at this end. The fourth boundary condition, zero moment at the free end, is automatically satisfied by neglecting bending stiffness.
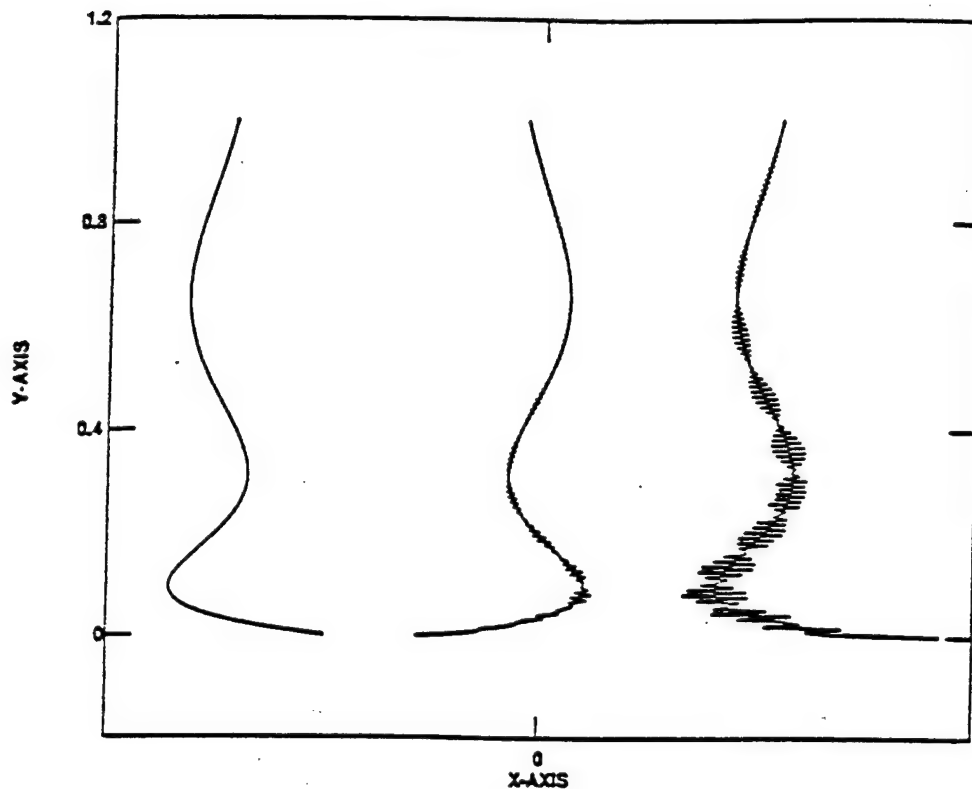
20

Figure 3.1: Example of growth of instability in an undamped explicit formulation at times t=0.0, 2.5, and 3.0 seconds.

3.3.2 Finite-Difference Approximation

The basic premise of the explicit formulation is to write all spatial derivatives in terms of the previous time step and to then solve for the new time values directly. The formulation begins by first discretizing the cable into n nodes. The governing equations are then applied directly at each node. First-order and second-order approximations are used for the time and spatial derivatives, respectively. Second-order forward and backward differences are used for spatial derivatives at nodes 1 and n, respectively.

As with any numerical scheme, stability is a major concern. It has been determined that in the formulation described above some degree of *numerical viscosity* is required for stability. This finding is demonstrated in figure 3.1. The problem studied was a hanging chain in air, subject to a sinusoidal displacement at the top. The cable was initially in a Bessel function shape, as given by the third natural mode of the linear system. The instability encountered was due to undamped high frequency parasitic waves generated at the lower boundary. It can be shown that these waves grow exponentially in time (Mitchell and Griffiths, 1980). The goal is to construct a numerical scheme which is accurate for the long wavelengths (which are the main interest) while at the same time dissipates the energy at the short wavelengths (which tend to corrupt the solution). Such a method is no less accurate than a nondissipative model, as the latter is already inaccurate for high-spatial wave numbers. For this reason an artificial dissipative term is added to each approximation of the time derivatives and the degree of dissipation is controlled by the leading coefficient α, where $\alpha \ll 1$. Mathematically, the procedure is represented by the approximation below.

21

$$\frac{\partial u}{\partial t} \approx \frac{\partial u}{\partial t} - \alpha \frac{\partial^2 u}{\partial x^2} \tag{3.2}$$

This procedure is similar to the Lax-Fredrichs and Lax-Wendroff (Mitchell and Griffiths, 1980) formulations of the first-order wave equation. Within these two methods, the leading coefficient α is dependent upon the spatial and time stepping increments, Δs and Δt, respectively, and is given by the following:

$$\alpha = \frac{\Delta s^2}{2\Delta t} \qquad Lax - Fredrichs$$

$$\alpha = \frac{\Delta t}{2} \qquad Lax - Wendroff.$$

Within the present explicit scheme, the α coefficient is independent of the stepping factors and can be varied along the cable and between the independent variables (ϕ, u, v). This allows the user greater flexibility during the investigation. The basic idea is to choose α of sufficient magnitude to provide stability while being small enough to have a negligible effect on accuracy.

Combining the approximations described above yields the following system of equations:

Node 1 (forward-differences)

$$\phi_1^{i+1} = \bar{\phi}_1^i - \lambda_r[v_3^i - 4v_2^i + 3v_1^i + u_1^i(\phi_3^i - 4\phi_2^i + 3\phi_1^i)] \tag{3.3}$$

$$u_1^{i+1} = \bar{u}_1^i + v_1^i(\phi_1^{i+1} - \bar{\phi}_1^i) + \frac{\lambda_r}{m}(-T_3^i + 4T_2^i - 3T_1^i) - \frac{w_o\Delta t}{m}\cos(\phi_1^i) - \frac{\Delta t}{m}\frac{1}{2}\rho_w D\pi C d_t u_{r1}^i|u_{r1}^i| \tag{3.4}$$

$$v_1^{i+1} = \bar{v}_1^i - \frac{m}{m_1}u_1^i(\phi_1^{i+1} - \bar{\phi}_1^i) - \frac{m_a}{m_1}[J_Y^{i+1}\cos(\phi_1^{i+1}) - J_Y^i\cos(\phi_1^i)] + \frac{w_o\Delta t}{m_1}\sin(\phi_1^i) - \frac{\lambda_r}{m_1}T_1^i(\phi_3^i - 4\phi_2^i + 3\phi_1^i) - \frac{\Delta t}{m_1}\frac{1}{2}\rho_w DC d_n v_{r1}^i|v_{r1}^i| \tag{3.5}$$

$$T_1^i = 0.0 \tag{3.6}$$

Internal Nodes (central-differences)

$$\phi_j^{i+1} = \bar{\phi}_j^i - \lambda_r[v_{j+1}^i - v_{j-1}^i + u_j^i(\phi_{j+1}^i - \phi_{j-1}^i)] \tag{3.7}$$

$$u_j^{i+1} = \bar{u}_j^i + v_j^i(\phi_j^{i+1} - \bar{\phi}_j^i) + \frac{\lambda_r}{m}(T_{j+1}^i - T_{j-1}^i) - \frac{w_o\Delta t}{m}\cos(\phi_j^i) - \frac{\Delta t}{m}\frac{1}{2}\rho_w D\pi C d_t u_{rj}^i|u_{rj}^i| \tag{3.8}$$

$$v_j^{i+1} = \bar{v}_j^i - \frac{m}{m_1}u_j^i(\phi_j^{i+1} - \bar{\phi}_j^i) - \frac{m_a}{m_1}[J_Y^{i+1}\cos(\phi_j^{i+1}) - J_Y^i\cos(\phi_j^i)] + \frac{w_o\Delta t}{m_1}\sin(\phi_j^i) - \frac{\lambda_r}{m_1}T_j^i(\phi_{j+1}^i - \phi_{j-1}^i) - \frac{\Delta t}{m_1}\frac{1}{2}\rho_w DC d_n v_{rj}^i|v_{rj}^i| \tag{3.9}$$

$$u_{j+1}^{i+1} - u_{j-1}^{i+1} = v_j^{i+1}(\phi_{j+1}^{i+1} - \phi_{j-1}^{i+1}) \tag{3.10}$$

22

Node N (backward-differences)

$$\phi_n^{i+1} = \bar{\phi}_n^i + \lambda_r[v_{n-2}^i - 4v_{n-1}^i + 3v_n^i] + u_n^i(\phi_{n-2}^i - 4\phi_{n-1}^i + 3\phi_n^i) \qquad (3.11)$$

$$u_n^{i+1} = prescribed \qquad (3.12)$$

$$v_n^{i+1} = prescribed \qquad (3.13)$$

$$u_{n-2}^{i+1} - 4u_{n-1}^{i+1} + 3u_n^{i+1} = v_n^{i+1}(\phi_{n-2}^{i+1} - 4\phi_{n-1}^{i+1} + 3\phi_n^{i+1}) \qquad (3.14)$$

Here the subscript j is used to denote the node number while the superscript i denotes the time step. The spacing ratio λ_r is given by $\lambda_r = \frac{\Delta t}{2\Delta s}$ and $m_1 = m + m_a$. The overbar is used to denote a term which has been modified to include the necessary artificial dissipation. If additional dissipation was not required, the overbar would simply be removed. In terms of the general variable q, $\bar{q}$ is given by

$$\begin{aligned}
\bar{q}_1^i &= q_1^i + \frac{2\lambda\alpha}{\Delta s}(q_1^i - 2q_2^i + q_3^i) \qquad (3.15)\\
\bar{q}_j^i &= q_j^i + \frac{2\lambda\alpha}{\Delta s}(q_{j-1}^i - 2q_j^i + q_{j+1}^i)\\
\bar{q}_n^i &= q_n^i + \frac{2\lambda\alpha}{\Delta s}(q_n^i - 2q_{n-1}^i + q_{n-2}^i).
\end{aligned}$$

It should be noted at this point that (3.10) and (3.14) are written as implicit statements. This is a necessary modification for the solution procedure. Briefly, the algorithm proceeds in the following manner. First the unknown angles are solved for directly using (3.3), (3.7) and (3.11). Next, (3.4), (3.5), (3.8), (3.9), (3.12), and (3.13) are introduced into (3.10) and (3.14). By including (3.6), a $n \times n$ matrix is formed with which to solve for the unknown tension values. These values are then used to solve directly for the velocities. This procedure is then repeated through the desired number of time steps. Within the algorithm, the banded structure of the matrix is exploited. Therefore, the matrix solution takes roughly n operations and is only performed once per time-step.

3.3.3 EXPLICIT SCHEME RESULTS

At the present time, the most widely used finite-difference solver for the cable equations without bending stiffness is the implicit routine first developed by Ablow and Schechter (1983). Therefore results obtained with the explicit scheme will be directly compared with this method. The implicit method will be discussed in greater detail in §3.4.

The three main concerns associated with the development of any numerical algorithm are accuracy, stability and computational efficiency. These topics are all closely related. On the basis of accuracy, the implicit scheme is superior in that second-order approximations are used for evaluating the time derivatives while the explicit scheme is only first-order in time (use of second-order differences in the explicit scheme proved highly unstable and was therefore abandoned). In addition, some error is introduced within the explicit scheme by the addition of numerical viscosity. Both methods prove stable provided sufficient numerical dissipation is added to the explicit scheme. Excessive amounts of dissipation will inhibit accuracy, however, therefore the explicit scheme is limited to some degree in choice of stepping parameters. With regard to efficiency, the explicit scheme appears to hold an advantage in that no iterations are required and the matrix problem is four times smaller.

23

Finite-Difference Method	# of Nodes	Time-step
Explicit	80	0.002
Implicit	80	0.016

Table 3.1: Case studies for hanging chain problem

Therefore, for comparable stepping increments, the implicit scheme requires at least eight times more operations, assuming only two iterations per time step and that solution of an $n \times n$ banded matrix problem is on the order of n operations.

A direct comparison between the methods was obtained by studying the motions of a hanging chain in air. For small motions, an analytic solution for the displacement $q(t, s)$ may be obtained in terms of Bessel functions, and is given by Triantafyllou and Triantafyllou (1991).

$$q_n(t, s) = J_o(2\omega_n \sqrt{s}) \sin(\omega_n t). \qquad (3.16)$$

The third mode was used in the analysis ($\omega_3 L = 4.327$) and the velocities were initialized within the algorithms according to (3.16). Several cases, involving a wide range of stepping increments were studied and two indicative cases are listed in 3.1. For the explicit method, the instability was generated near the top boundary, therefore additional dissipation was incorporated near this point. The stepping increments were chosen so as to keep the relative error in the explicit solution below 0.5 percent. The two cases are roughly comparable in computation effort.

The results obtained are shown in figures 3.2 and 3.3. The error measure is based on the rms difference between the analytic and numerical solutions, expressed as a percentage of the maximum displacement. As figure 3.2 shows, it is possible to obtain comparable results with the explicit scheme, in some cases, provided the dissipation is added correctly. Figure 3.3 depicts the cable shape at various times and shows the error incurred by both methods. For reduced stepping increments, both methods converge to the analytic result.

The two methods were applied to a second problem involving a positively buoyant cable, pinned at the bottom, subject to a sinusoidal current with a period of 1.0 seconds. The results are shown in figure 3.4. Computational time was roughly equivalent. As readily seen, both methods converge to the same result. Therefore, the explicit scheme provides a means with which to compare the results of the implicit scheme. In addition, unlike the implicit scheme, the explicit scheme does not become singular for zero intial tension. This is due to the fact that the tensions are deliberately cast as the unknowns in the matrix problem. The explicit scheme may therefore be used to study a wider range of initial value problems.

In general, for simulations with longer time spans, the artificial dissipation term may begin to affect the solution accuracy. Therefore, the explicit scheme is better suited for transient problems and can be used in conjunction with an implicit scheme to step-through computationally difficult periods. In submerged cable problems, however, the fluid drag provides additional damping, thereby helping to stabilize the explicit scheme. For such problems the explicit method retains its accuracy over long time spans.
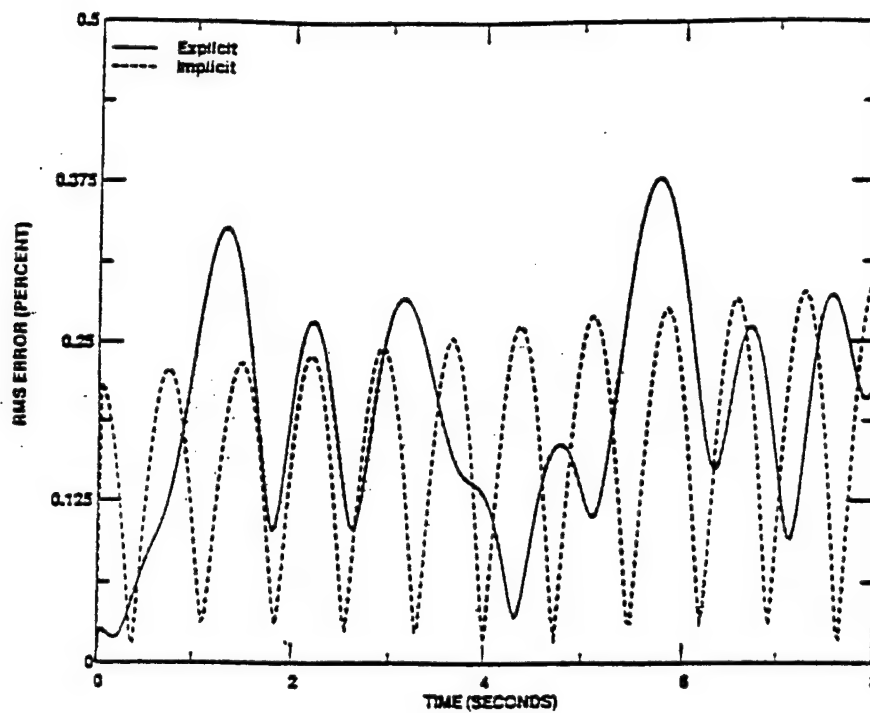
24

Figure 3.2: Comparison of calculated error associated with each case study.
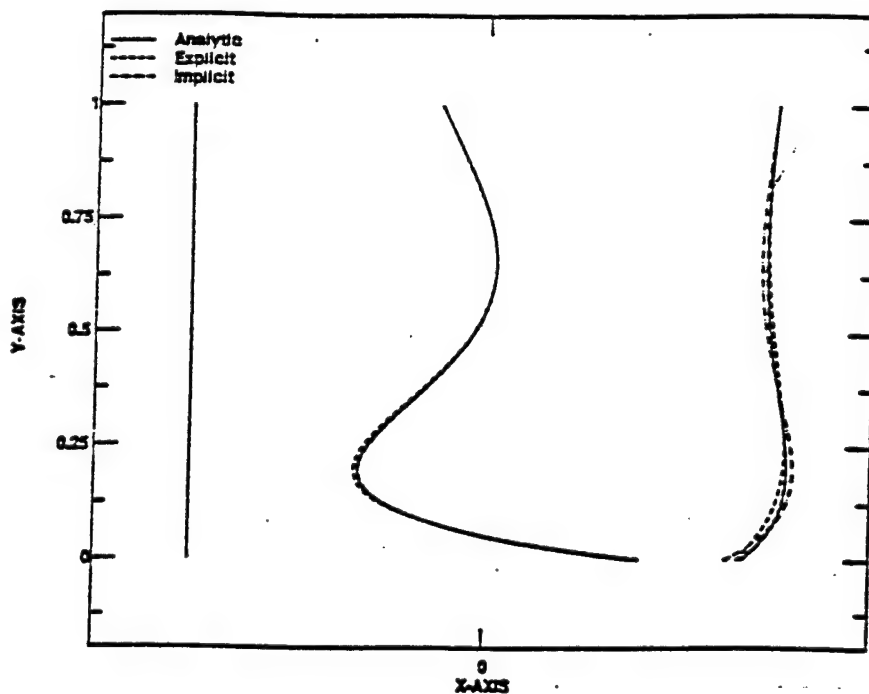

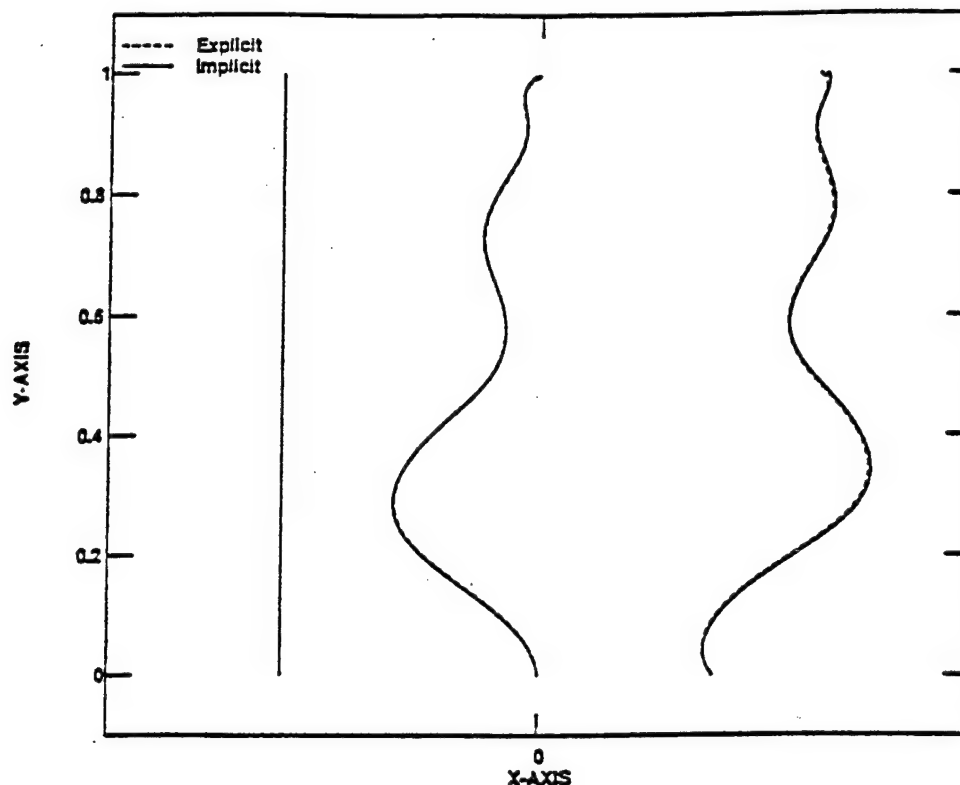Figure 3.3: Calculated cable shapes for hanging chain problem at times t=0.0, 4.0 and 6.5 seconds.

25

Figure 3.4: Calculated cable shape from explicit and implicit schemes for anchored cable subjected to a sinusoidal current, at times t=0.0, 6.0, and 15.5 seconds.

3.4 Implicit Formulation with Bending Stiffness

Little research has been conducted, in the past, on the effects of bending stiffness. This is attributable to the fact that for long taut cables, as typically studied, bending forces are often negligible. Sanders (1982) developed two criteria for analyzing the importance of bending stiffness. First the internal shear force must be significantly lower than the cable tension. Secondly, for a cable of constant curvature, in which the shear force vanishes, the tension in the fibers due to pure bending must be less than the cable tension. The nondimensional analysis conducted in §2 also provides guidance as to when bending effects can be neglected. For low-tension cables, large deformations can occur which give rise to shear forces that can be of equal magnitude as the cable tension. Therefore, bending stiffness must be included for such cases.

McCoy (1972) found that significant stress differences arise in the neighborhood of concentrating loadings if bending stiffness is retained. He found the magnitude of these differences was independent of the amount of bending stiffness, however the extent over which these differences occur diminishes wih decreased bending stiffness.

Ketchman and Lou (1975) developed a two-dimensional finite-element model with bending stiffness. They applied their method to towed cables and determined that the effects of bending stiffness were confined to a region near the free end of the cable, where the tension was lowest. Their approach, however, is limited in its applications as inertial forces

26

were neglected.

3.4.1 Equations of Motion and Boundary Conditions

The three-dimensional nonlinear equations of motion, as given by (2.41), can be expressed in matrix form as follows:

$$\mathbf{M}\frac{\partial \vec{Y}}{\partial s} = \mathbf{N}\frac{\partial \vec{Y}}{\partial t} + \vec{Q} \tag{3.17}$$

where

$$\vec{Y} = (T, S_n, S_b, u, v, w, \phi, \theta, \Omega_2, \Omega_3)^T \tag{3.18}$$

$$\mathbf{M} = \begin{bmatrix}
1 & 0 & 0 & 0 & 0 & 0 & 0 & 0 & 0 & 0 \\
0 & 1 & 0 & 0 & 0 & 0 & 0 & 0 & 0 & 0 \\
0 & 0 & 1 & 0 & 0 & 0 & 0 & 0 & 0 & 0 \\
0 & 0 & 0 & 1 & 0 & 0 & 0 & 0 & 0 & 0 \\
0 & 0 & 0 & 0 & 1 & 0 & 0 & 0 & 0 & 0 \\
0 & 0 & 0 & 0 & 0 & 1 & 0 & 0 & 0 & 0 \\
0 & 0 & 0 & 0 & 0 & 0 & \cos\theta & 0 & 0 & 0 \\
0 & 0 & 0 & 0 & 0 & 0 & 0 & 1 & 0 & 0 \\
0 & 0 & 0 & 0 & 0 & 0 & 0 & 0 & EI & 0 \\
0 & 0 & 0 & 0 & 0 & 0 & 0 & 0 & 0 & EI
\end{bmatrix}$$

$$\mathbf{N} = \begin{bmatrix}
0 & 0 & 0 & m & 0 & 0 & -mv\cos\theta & mw & 0 & 0 \\
0 & 0 & 0 & 0 & m+m_a & 0 & mu\cos\theta + mw\sin\theta & 0 & 0 & 0 \\
0 & 0 & 0 & 0 & 0 & m+m_a & -mv\sin\theta & -mu & 0 & 0 \\
\frac{1}{EA} & 0 & 0 & 0 & 0 & 0 & 0 & 0 & 0 & 0 \\
0 & 0 & 0 & 0 & 0 & 0 & (1+\frac{T}{EA})\cos\theta & 0 & 0 & 0 \\
0 & 0 & 0 & 0 & 0 & 0 & 0 & -(1+\frac{T}{EA}) & 0 & 0 \\
0 & 0 & 0 & 0 & 0 & 0 & 0 & 0 & 0 & 0 \\
0 & 0 & 0 & 0 & 0 & 0 & 0 & 0 & 0 & 0 \\
0 & 0 & 0 & 0 & 0 & 0 & 0 & 0 & 0 & 0
\end{bmatrix}$$

$$\vec{Q} = \begin{bmatrix}
S_n\Omega_3 - S_b\Omega_2 + w_o\cos\phi\cos\theta - R_{d1} \\
-\Omega_3(T + S_b\tan\theta) - w_o\sin\phi - R_{d2} + m_a\frac{\partial J_2}{\partial t} \\
S_n\Omega_3\tan\theta + T\Omega_2 + w_o\cos\phi\sin\theta - R_{d3} + m_a\frac{\partial J_3}{\partial t} \\
\Omega_3 v - \Omega_2 w \\
-\Omega_3(v + w\tan\theta) \\
\Omega_3 v\tan\theta + \Omega_2 u \\
\Omega_3 \\
\Omega_2 \\
EI\Omega_3^2\tan\theta + S_b(1+\frac{T}{EA}) \\
EI\Omega_2\Omega_3\tan\theta - S_n(1+\frac{T}{EA})
\end{bmatrix}$$

To complete the mathematical formulation we must consider boundary conditions. One end of the cable ($s = 0$) is considered as a free boundary while the other end ($s = L$) is

pinned to an anchor or ship. At the free boundary, the tension, moment, and shear forces are all zero. At the pinned end, the three velocities are prescribed and the moments are set equal to zero. Mathematically, these boundary conditions are expressed as follows:

$$T(t,0) = 0 \tag{3.19}$$
$$EI\Omega_2(t,0) = 0$$
$$EI\Omega_3(t,0) = 0$$
$$EI\frac{\partial \Omega_2(t,0)}{\partial s} = 0$$
$$EI\frac{\partial \Omega_3(t,0)}{\partial s} = 0$$
$$u(t,L) = U(t)$$
$$v(t,L) = V(t)$$
$$w(t,L) = W(t)$$
$$EI\Omega_2(t,L) = 0$$
$$EI\Omega_3(t,L) = 0$$

where $U(t)$, $V(t)$, and $W(t)$ are some known velocities. In this fashion, the required ten boundary conditions are imposed and an equal number are applied at each boundary.

3.4.2 FINITE-DIFFERENCE APPROXIMATION

As with any finite difference formulation the cable is first discretized into n nodes, separated by Δs, and time is divided into a series of steps of length Δt. The set of equations given by (3.18) are solved at the midpoint between nodes j and $j+1$, denoted by $j+\frac{1}{2}$, and at the time $i+\frac{1}{2}$. The partial derivatives in (3.18) are expressed using centered finite differences as follows:

$$\frac{\partial Y}{\partial t} = \frac{Y_j^{i+1} - Y_j^i}{\Delta t} \tag{3.20}$$
$$\frac{\partial Y}{\partial s} = \frac{Y_{j+1}^i - Y_j^i}{\Delta s}.$$

Introducing (3.20) into (3.18) and evaluating the equations at $j+\frac{1}{2}$ and $i+\frac{1}{2}$ yields

$$[M_{j+1}^{i+1} + M_j^{i+1}]\frac{Y_{j+1}^{i+1} - Y_j^{i+1}}{\Delta s} + [M_{j+1}^i + M_j^i]\frac{Y_{j+1}^i - Y_j^i}{\Delta s} =$$
$$[N_{j+1}^{i+1} + N_{j+1}^i]\frac{Y_{j+1}^{i+1} - Y_{j+1}^i}{\Delta t} + [N_j^{i+1} + N_j^i]\frac{Y_j^{i+1} - Y_j^i}{\Delta t} +$$
$$Q_{j+1}^{i+1} + Q_j^{i+1} + Q_{j+1}^i + Q_j^i. \tag{3.21}$$

This provides $10(n-1)$ equations with which to solve for the $10n$ unknowns. The remaining equations are provided by the 10 boundary conditions.

The set of difference equations given by (3.21), along with the boundary conditions, provide a coupled set of nonlinear equations with which to solve for the new time values. A Newton-Raphson (Dahlquist and Bjorck, 1974) iteration scheme is used to solve for the unknown variables. Several iterations per time-step may be required for convergence. However, the banded structure of the resulting matrix can be exploited, reducing the computations to roughly n operations per iteration.

Ablow and Schechter (1983) base the stability of their numerical scheme on the determinant of the **M** matrix. This is because this matrix is inverted within their algorithm. If bending stiffness is neglected, we find that

$$det \quad \mathbf{M} = -T^2 \cos \theta. \tag{3.22}$$

Therefore, if the cable loses tension during the computations, or if the tension is zero initially, their method becomes unstable. In the numerical scheme outlined here, the **M** is never actually inverted, however method still fails due the zero tension singularity in the equations of motion. The method will also become unstable if the cable becomes horizontal in the out-of-plane direction (i.e. $\theta = \frac{\pi}{2}$ or $\frac{3\pi}{2}$). This singularity stems from an ambiguity in the reference system and can be controlled, but not removed entirely, by selecting an alternative Euler rotation sequence.

A markedly different result is obtained if bending stiffness is retained. The determinant of the **M** matrix shown here is easily obtained by taking the product of the trace yielding

$$det \quad \mathbf{M} = (EI)^2 \cos \theta. \tag{3.23}$$

Therefore, provided the bending stiffness is finite, the matrix can be inverted, regardless of the cable tension magnitude. Howell (1992) has previously demonstrated that incorporating bending stiffness eliminates the zero tension singularity for the two-dimensional case.

3.4.3 IMPLICIT SCHEME RESULTS

The implicit scheme has been verified within the linear regime, and the effect of bending stiffness on the dynamics has been studied by Howell (1992). Figure 3.5 compares two-dimensional results for a cable, subjected to a sinusoidal current of period 1.0 seconds, with and without bending stiffness. A relatively large nondimensional bending stiffness term of $EI/mgL^3 = 10^{-3}$ was implemented for the analysis. As readily seen, the cable shape is significantly altered with the curvature being greatly reduced by bending stiffness. In particular, bending-stiffness effects were greatest over the top half of the cable. This is due to the lower cable tension in this region and demonstrates the physical importance of bending stiffness in regions of low tension.
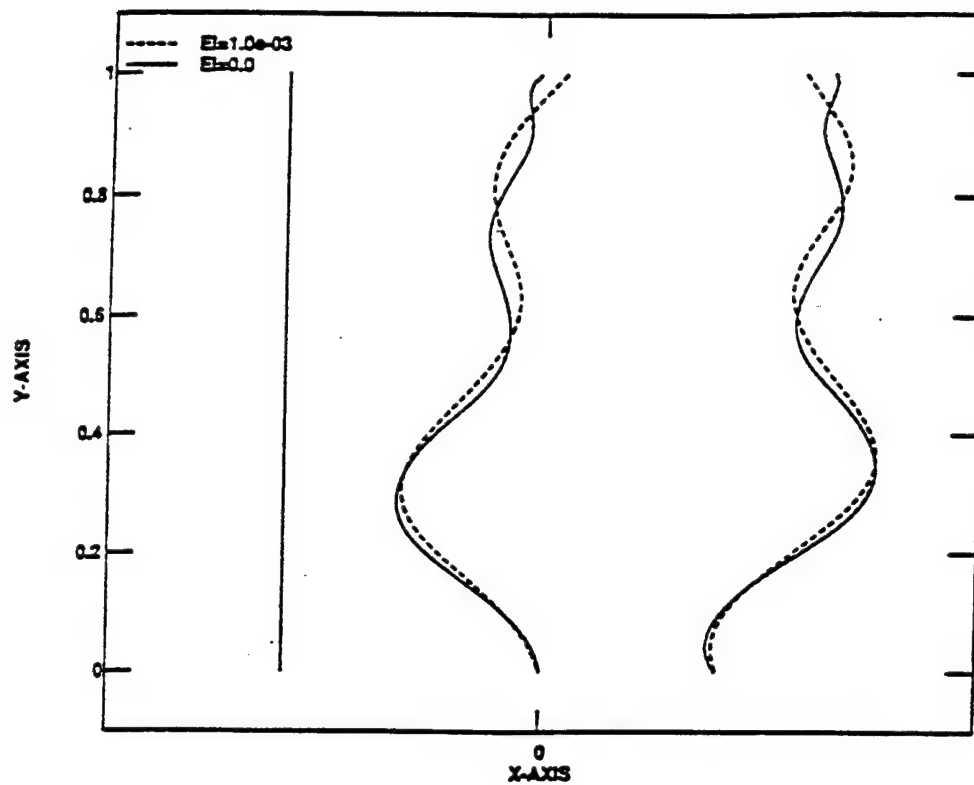
29

Figure 3.5: Effects of bending stiffness on anchored cable subjected to a sinusoidal current, at times t=0.0, 6.0 and 15.5 seconds.

IV. NONLINEAR IMPULSIVE MOTIONS

4.1 Introduction

In this section, we explore certain fundamental mechanisms of cable response intrinsic to low tension behavior by considering a cable under zero initial tension. Excitation of the cable is accomplished by the application of an impulsive load at one end and the resulting tension and velocity distribution along the cable is studied for a variety of initial configurations.

Understanding the dynamics of impulsively loaded cables is of importance as low tension cables are often more susceptible to this form of excitation than are taut cables. To understand why this occurs, consider that for low-tension cables, by definition the dynamic tension component is of equal or greater magnitude than the static tension. Therefore, it is very likely that the dynamic tension will act to cancel the static tension over a portion of the loading cycle, a phenomenon often referred to as tension clipping (Shin, 1991). This can occur even though the initial tension is high. Following the periods of zero tension, tensile forces initially build-up over a short time span and can therefore be considered impulsive. These forces, in turn, can lead to large cable accelerations and maximum cable forces nine times the static payload weight have been found to occur (Goeller, 1970).

Needless to say, this can become a highly dangerous situation in many marine operations such as towing. Several authors, including Shin (1987), Milgram et al. (1988), and Papazoglou et al. (1990), have described such dynamics, concentrating primarily on the snap condition, at which the tension is maximum.

Herein we concentrate on the tension distribution and resulting velocities immediately after the application of the impulsive load. The results presented here are summarized in a recent paper by Triantafyllou and Howell (1992).

4.2 Formulation of Impulsive Equations of Motion

The equations of motion for a cable under impulsive loading have been derived previously, first by Routh (1955) and then Lamb (1914), and more recently by Triantafyllou and Howell (1992). As with these previous authors, we consider the cable to be inextensible. This condition of inextensiblity is based on the following assumptions: 1) the static tension is of the order of the total weight of the cable; 2) the velocities applied impulsively on the cable are small compared to the speed of elastic waves; and 3) one end of the cable is free or the cable has large sag. The first assumption defines a low tension cable, the primary focus of this research. The second condition ensures that elastic waves will not be excited, while the third condition, combined with the second, ensures that the cable does not stretch considerably. In fact, if one cable end is free, the tension is zero at that point at all times. Therefore, for moderately long cables with high Young's modulus (such as metallic cables), the tension never builds to sufficiently large values to cause substantial stretching. If one end of the cable is not free, however the cable sag is large, elastic effects remain small, even for taut cables. This has been shown by Irvine and Caughey (1974). They determined that the relative parameter which quantifies the effects of elasticity is λ, where

$$\lambda^2 = \frac{EA}{H}\left(\frac{w_o L}{H}\right)^2. \tag{4.1}$$

Here H denotes the horizontal static force applied at the cable end points. The parameter λ^2 is proportional to the ratio of the elastic to catenary stiffness of the cable. This ratio is typically very large for large sag to span ratios, i.e. large values of $w_o L/H$. When the elastic stiffness is very large, the cable employs its catenary stiffness, thereby preserving the cable length. In §6 we formally derive the expression for λ.

As in §2, we derive the equations of motion using a lagrangian reference frame, fixed on the cable, and we adopt the same nomenclature defined previously. We neglect the effects of bending stiffness. However, forces in bending are treated in §4.4.

The inextensible cable governing equations are given by

$$m\frac{D\vec{V}}{Dt} = \frac{D(T\hat{t})}{Ds} + \vec{R}. \tag{4.2}$$

The impulsive equations of motion are determined by integrating (4.2). We denote $T_i(s)$ as the amplitude of the impulsive tension, developed at time $t = 0^+$, and define the cable's velocity immediately before and after the application of the impulsive tension as $\vec{V}^-$ and $\vec{V}^+$, respectively. Integrating (4.2) yields:

$$m(\vec{V}^+ - \vec{V}^-) = \frac{D(T_i\hat{t})}{Ds}. \tag{4.3}$$

We can express (4.3) in component form using the vector $\vec{\Omega}$ to represent the local curvature of the cable. At this point we define $\vec{\Omega} = (\Omega_1, \Omega_2, \Omega_3)$ as the Darboux vector of rotation (Hildebrand, 1976), which is given by the following:

$$
\begin{aligned}
\Omega_1 &= \frac{1}{\tau} \\
\Omega_2 &= 0 \\
\Omega_3 &= \frac{1}{\rho}
\end{aligned}
\tag{4.4}
$$

where ρ denotes the local radius of curvature and τ the local radius of torsion. Note that we have chosen to adopt the so-called principal directions (Hildebrand, 1976) for the unit vectors $(\hat{t}, \hat{n}, \hat{b})$. This is in contrast to the definitions used in §2, where the orientation of the normal and binormal directions about the tangent direction was chosen arbitrarily. This change has been made here because the use of principal coordinates greatly simplifies the impulsive equations.

Using (4.4), we can express (4.3) in component form yielding

$$
\begin{aligned}
m(u^+ - u^-) &= \frac{dT_i}{ds} \\
m(v^+ - v^-) &= T_i\Omega_3 \\
m(w^+ - w^-) &= 0
\end{aligned}
\tag{4.5}
$$

The compatibility relations are derived on the same basis as in §2, i.e.

$$\frac{D\vec{V}^\pm}{Ds} = \frac{D\hat{t}}{Dt}. \tag{4.6}$$

From (4.6), we find the following relations which are valid for both $t = 0^-$ and $t = 0^+$,

Figure 4.1: Cable in a straight line.

$$\frac{du}{ds} - \Omega_3 v = 0 \tag{4.7}$$

$$\frac{dv}{ds} + \Omega_3 u - \Omega_1 w = \omega_3$$

$$\frac{dw}{ds} + \Omega_1 v = -\omega_2.$$

Eliminating the velocities from (4.5) and (4.7) provides a single equation in terms of the impulsive tension.

$$\frac{d^2 T_i}{ds^2} - \Omega_3^2 T_i = 0 \tag{4.8}$$

Equation (4.8) is an important result which shows that the impulsive tension is independent of the geometric torsion, Ω_1, and depends entirely on the local curvature of the cable given by Ω_3. From (4.5) we find that the binormal velocity remains constant, while the tangential and normal velocities depend exclusively on the curvature and magnitude of the impulsive tension.

4.3 Solution of Impulsive Dynamics

We use (4.8) to derive closed form analytic results for several initial configurations. These results are used to identify the impulsive tension distribution along the cable, as well as the velocities that develop due to the impulsive loading.

4.3.1 CABLE IN A STRAIGHT LINE

Perhaps the most simple example to consider is a cable of length L, sitting at rest in a straight line configuration on a horizontal frictionless table (figure 4.1). For this case $\Omega_3 = 0$ because the radius of curvature is infinite. One end of the cable is suddenly pulled at an amplitude $T_i(L) = T_o$ while the other end is free, i.e. $T_i(0) = 0$. Using these boundary conditions and (4.8), the solution is obtained as
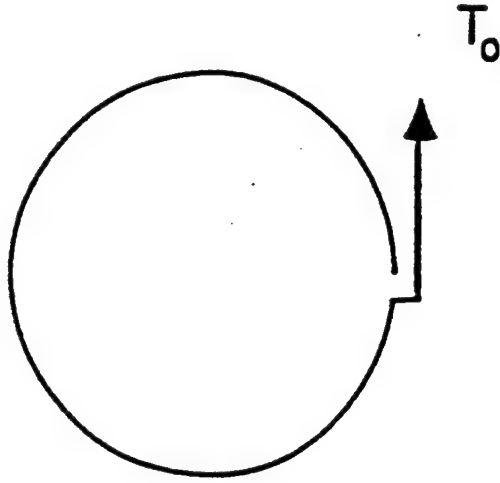
Figure 4.2: Cable in the form of a circle.

$$
\begin{aligned}
T_i(s) &= \frac{T_o s}{L} \\
u^+(s) &= \frac{T_o}{mL}.
\end{aligned}
\tag{4.9}
$$

All other quantities are zero. From these results we find that if the cable is initially straight, the impulsive tension distribution varies linearly along the cable and the entire cable begins to move in the tangential direction at the same velocity.

4.3.2 CABLE IN THE FORM OF A CIRCLE

Another simple example which can be solved exactly is the case of a cable of length L sitting, at rest along a full arc of a circle of radius a, on a horizontal frictionless table (figure 4.2). One end of the cable is suddenly pulled at an amplitude T_o and the boundary conditions are given by $T_i(0) = 0$ and $T_i(L) = T_o$. The solution of (4.8) is given by

$$
\begin{aligned}
T_i(s) &= T_o \frac{sinh(s/a)}{sinh(L/a)} \\
u^+(s) &= \frac{T_o}{ma} \frac{cosh(s/a)}{sinh(L/a)} \\
v^+(s) &= \frac{T_o}{ma} \frac{sinh(s/a)}{sinh(L/a)}
\end{aligned}
\tag{4.10}
$$

The second compatibility relation in (4.7) provides the angular velocity

34

$$\omega_3(s) = \frac{2T_o}{ma^2} \frac{cosh(s/a)}{sinh(L/a)}. \tag{4.11}$$

4.3.3 CABLE IN THE FORM OF A HELIX

To show that the initial development of tension is independent from torsion, we consider a cable with a three-dimensional initial configuration resting in the form of a helix, i.e. $\rho = a$ and $\tau = b$, where a and b are constants. Again one end of the cable is suddenly pulled and we impose the same boundary conditions as in the previous example. The exact solution is obtained as follows:

$$T_i(s) = T_o \frac{sinh(s/a)}{sinh(L/a)} \tag{4.12}$$

$$u^+(s) = \frac{T_o}{ma} \frac{cosh(s/a)}{sinh(L/a)}$$

$$v^+(s) = \frac{T_o}{ma} \frac{sinh(s/a)}{sinh(L/a)}$$

$$w^+(s) = 0$$

$$\omega_3(s) = \frac{2T_o}{ma^2} \frac{cosh(s/a)}{sinh(L/a)}$$

$$\omega_2(s) = -\frac{T_o}{mab} \frac{sinh(s/a)}{sinh(L/a)}$$

As readily seen, the same tension and velocity distribution develops as with the two-dimensional case of a chain in a circle, the only exception being that ω_2 is nonzero. This shows the independence of initially developing tension from torsion.

4.3.4 CABLE OF REVERSING CURVATURE

We next consider a cable of length $2L$ at rest on a frictionless horizontal table. The cable configuration is comprised of two circular arcs of radius a and opposite curvature, as shown in 4.3. The curvature Ω_3 is discontinuous at the origin, which is fixed at the midpoint of the cable, jumping from the value $-\frac{1}{a}$ to the value $\frac{1}{a}$. When one end of the cable is suddenly pulled with the impulsive force T_o, the solution can be obtained as done previously, and we find

$$T_i(s) = T_o \frac{sinh([s+L]/a)}{sinh(2L/a)}. \tag{4.13}$$

This is the same result obtained in the two previous examples, with the exception that here the origin has been shifted and the length of the cable doubled. The tangential velocity is also easily obtained. However, when we proceed to derive the normal velocity, a physically impossible discontinuity appears in the velocity $v^+(s)$ at the point where the curvature is discontinuous. This can be shown by examining the governing equation in the normal direction given by
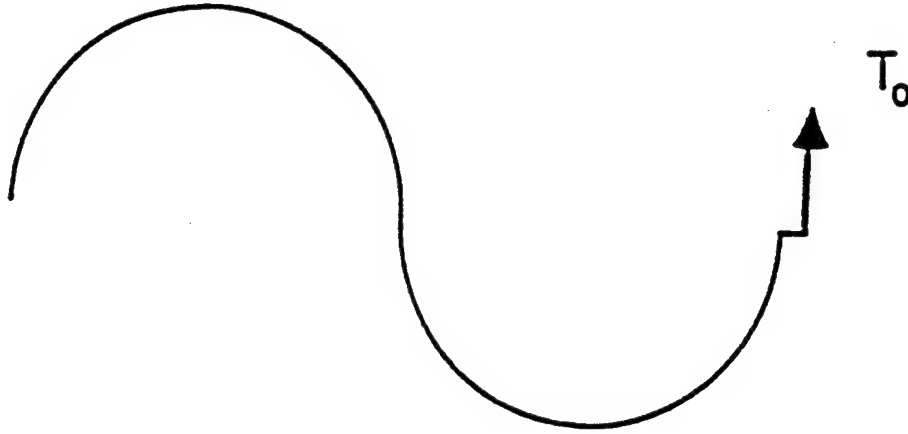
Figure 4.3: Cable of reversing curvature.

$$v^+(s) = \frac{1}{m}\Omega_3(s)T_i(s). \qquad (4.14)$$

Furthermore, the angular velocity ω_3 develops a singularity, as evidenced in (4.7), when $v(s)$ is discontinuous.

A discontinuity in the curvature is possible only for a perfectly flexible cable. This discontinuity can be removed by introducing the bending stiffness of the cable, which ensures a smooth initial configuration. However, if the singularity identified in the case of reversing curvature is related to a basic cable mechanism, than the manner of smoothing of the solution is of importance.

To determine if in fact this is the case, we consider the same example of a cable with reversing curvature at rest on a horizontal frictionless table, but we make the curvature reversal smooth. The initial curvature is chosen as

$$\Omega_3(s) = \begin{array}{ll} -1/a & -L \leq s \leq -\epsilon \\ s/a\epsilon & -\epsilon \leq s \leq \epsilon \\ 1/a & \epsilon \leq s \leq L \end{array}$$

where a, ϵ are constants and $\epsilon \ll L$. The solution when one end is impulsively loaded can be obtained separately in the three regions defined above. In the first and third regions the solution for the tension can be obtained explicitly as before, with two unknown constants in each region. In the middle region the equation for the tension becomes:

$$\frac{d^2T_i}{ds^2} - \frac{s^2}{a^2\epsilon^2}T_i = 0. \qquad (4.15)$$

Using the substitution $s = x\delta$, with $\delta = \sqrt{a\epsilon/2}$, (4.15) can be brought into the standard form of the parabolic cylinder functions:

36

$$\frac{d^2 T_i}{dx^2} - \frac{x^2}{4} T_i = 0. \tag{4.16}$$

The solution of (4.16) can be expressed as the sum of two independent solutions of the parabolic cylinder equation, scaled with two unknown constants. Since $|x| \leq \sqrt{2\epsilon/a}$, we use the small argument power series expression of the parabolic cylinder functions (Abramowitz and Stegun, 1970) and match asymptotically the two outer regions with the inner (middle) region. This provides four matching conditions which combined with the two boundary conditions, the same conditions imposed in the previous examples, allows for the solution of all six unknown constants. As ϵ tends to zero, we obtain the following asymptotically valid results:

$$T_i(s) = T_o \frac{sinh([s+L]/a)}{sinh(2L/a)} \tag{4.17}$$

$$u^+(s) = \frac{T_o}{ma} \frac{cosh([s+L]/a)}{sinh(2L/a)}$$

$$v^+(s) = \Omega_3(s) \frac{T_o}{m} \frac{sinh([s+L]/a)}{sinh(2L/a)}$$

The rotational velocity suffers from a discontinuity at the edges of the middle region. The expression for ω_3 in the middle region is, asymptotically

$$\omega_3(s) = \frac{T_o}{ma\epsilon} \frac{sinh(L/a)}{sinh(2L/a)}. \tag{4.18}$$

The discontinuity at the edges can be removed by requiring that the first derivative of the curvature is everywhere continuous. The importance of (4.18), however, lies in identifying a mechanism for building large rotational velocities. We have found here that at the point of curvature reversal, ω_3 is inversely proportional to the width of the transition region.

4.4 Impulsive Motion of a Cable with Bending Stiffness

We have shown the importance of the manner in which the cable curvature is made continuous. For cables, the physical mechanism by which the curvature is made continuous, prior to the application of any load, is bending stiffness. After the cable is loaded, tension also acts to smooth the cable shape. Therefore, because the bending stiffness magnitude affects how the cable is initially made smooth, it is natural to extend the analysis by incorporating bending stiffness. Although the value of the bending stiffness only indirectly affects the dynamic response, for completeness we include bending forces in the dynamic equations as well, to study the direct effects of bending on the impulsive response.

As derived in §2, the governing equations incorporating bending stiffness, are given as

$$m \frac{D\vec{V}}{Dt} = \frac{D\vec{T}}{Ds} + \vec{R}. \tag{4.19}$$

$$\rho_c \mathbf{I} \frac{D\vec{\omega}}{Dt} = \frac{D\mathbf{M}}{Ds} + \hat{t} \times \vec{T} + \vec{Q}. \tag{4.20}$$

37

Due to the selection of principal coordinates, the moment vector $\mathbf{M}$ differs slightly from previously presented and is given by

$$
\begin{aligned}
M_1 &= GI_p\Omega_1 \\
M_2 &= 0 \\
M_3 &= EI\Omega_3.
\end{aligned}
\tag{4.21}
$$

Note that Ω_1 in (4.21) is the material torsion, which is, in general, different from the geometric torsion.

A nondimensional analysis of (4.20) was conducted in §2.3.2, based on which it was concluded that the inertial forces are negligible. In the context of impulsive forces, however, the relevant time scale is very short and large angular accelerations may develop, depending on the initial configuration. Therefore, we choose to retain these terms here.

If equation (4.20) is integrated in time from $t = 0^-$ to 0^+, we find that the contribution of the term involving $\mathbf{M}$ vanishes, assuming the length of integration is such that insufficient time has elapsed for the cable to alter its initial configuration. As a result, the shear forces may become impulsive as they must balance a step change in the rotational velocity. Otherwise, (4.20) will not be satisfied. One may explain the mechanism generating an impulsive shear force as a limiting process of infinitesimal shear deformation and large shear modulus, in complete analogy with the development of impulsive tension which involves infinitesimal extension and large Young's modulus.

Based on these considerations, we find that when the cable is subject to a forced motion, both the tension and shear forces become impulsive. Therefore, integrating (4.19) and (4.20) over the time period in which the impulsive load is applied yields the following equations of impulsive motion:

$$
\begin{aligned}
m(\vec{V}^+ - \vec{V}^-) &= \frac{D\vec{T_i}}{Ds} \\
\rho_c\mathbf{I}(\vec{\omega}^+ - \vec{\omega}^-) &= \hat{t} \times \vec{T}.
\end{aligned}
\tag{4.22}
$$

Expanding these equations along the $(\hat{t}, \hat{n}, \hat{b})$ system gives

$$
\begin{aligned}
m(u^+ - u^-) &= \frac{dT_i}{ds} - S_{ni}\Omega_3 \\
m(v^+ - v^-) &= \frac{dS_{ni}}{ds} + T_i\Omega_3 - S_{bi}\Omega_1 \\
m(w^+ - w^-) &= \frac{dS_{bi}}{ds} + S_{ni}\Omega_1 \\
\rho_c I_p(\omega_1^+ - \omega_1^-) &= 0 \\
\rho_c I(\omega_2^+ - \omega_2^-) &= -S_{bi} \\
\rho_c I(\omega_3^+ - \omega_3^-) &= S_{ni}
\end{aligned}
\tag{4.23}
$$

together with the compatibility relations (4.7). It is interesting to note that ω_1 did not appear explicitly in the previous equations which neglect bending. The results here show that ω_1 is in fact zero, independent of the initial configuration.

38

By eliminating the translation and angular velocities in (4.23) and (4.7), we find three equations in terms of the impulsive tension and shear forces (note that, for brevity, the subscript i is omitted).

$$\frac{d^2T}{ds^2} - T\Omega_3^2 - 2\Omega_3\frac{dS_n}{ds} - S_n\frac{d\Omega_3}{ds} + \Omega_1\Omega_3 S_b = 0 \qquad (4.24)$$

$$\frac{d^2S_n}{ds^2} - (\delta^2 + \Omega_1^2 - \Omega_3^2)S_n - 2\Omega_1\frac{dS_b}{ds} - S_b\frac{d\Omega_1}{ds} + 2\Omega_3\frac{dT}{ds} + T\frac{d\Omega_3}{ds} = 0$$

$$\frac{d^2S_b}{ds^2} - (\delta^2 + \Omega_1^2)S_b + 2\Omega_1\frac{dS_n}{ds} + S_n\frac{d\Omega_1}{ds} + \Omega_1\Omega_3 T = 0$$

where $\delta^2 = m/(\rho_c I)$.

For a cable of circular cross-section, $\delta^2 = 4/r^2$, where r is the radius of the cable cross-section. As a result, we find $\delta \gg (\Omega_1, \Omega_3)$ since neither the radius of curvature nor the radius of geometric torsion can be as small as the radius of the cable. As we will show, this implies the formation of boundary layers in shear.

4.5 Solution of the Cable Equations with Bending Stiffness

As an application we consider the two-dimensional impulsive motion of a cable, and reduce (4.24) to the following:

$$\frac{d^2T}{ds^2} - T(\frac{d\phi}{ds})^2 - S_n\frac{d^2\phi}{ds^2} - 2\frac{d\phi}{ds}\frac{dS_n}{ds} = 0 \qquad (4.25)$$

$$\frac{d^2S_n}{ds^2} - S_n(\delta^2 - (\frac{d\phi}{ds})^2) + T\frac{d^2\phi}{ds^2} + 2\frac{d\phi}{ds}\frac{dT}{ds} = 0$$

where $\phi(s)$ denotes the initial angle of the tangential vector of the cable with respect to a fixed direction.

We now reconsider the problem of a cable initially at rest in the form of a circle of radius a (figure 4.2). The boundary conditions described previously are imposed, as well as $S_n = 0$ at $s = 0, L$. To provide greater insight into the form of the equations of motion, we normalize the spatial variable s by the radius of curvature and set $x = s/a$. In addition, we define the quantity $\alpha = 4r^2/a^2$, where by physical considerations, $\alpha \ll 1$.

In terms of these quantities, the equations of motion are given as

$$\frac{d^2T}{dx^2} - T - 2\frac{dS_n}{dx} = 0 \qquad (4.26)$$

$$\alpha\frac{d^2S_n}{dx^2} - (1-\alpha)S_n + 2\frac{dT}{dx} = 0. \qquad (4.27)$$

The form of (4.27) clearly suggests the formation of boundary layers in shear because the highest-order derivative term is multiplied by α, meaning that, in general, it is not possible to obtain a solution which satisfies both boundary conditions if the equations are not reformulated near the boundaries. By conducting an asymptotic expansion in terms of α and a boundary layer analysis near $s = 0, L$, we find the following asymptotic solution, valid for $\alpha \ll 1$:
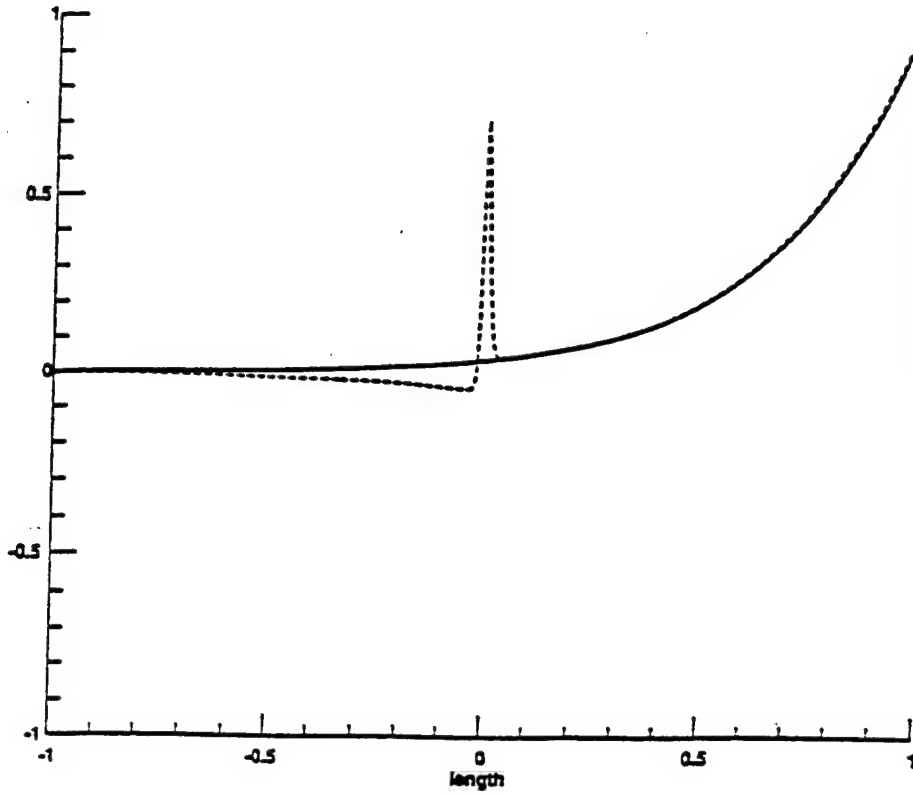
Figure 4.4: Tension (solid line) and angular velocity (dotted line) developing along a cable of reversing curvature (figure 4.3).

$$T(s) = T_o \frac{sinh(s/a)}{sinh(L/a)} \qquad (4.28)$$

$$u^+(s) = \frac{T_o}{ma} \frac{cosh(s/a)}{sinh(L/a)}$$

$$v^+(s) = \frac{T_o}{ma} \frac{sinh(s/a)}{sinh(L/a)}$$

$$S_n(s) = \frac{2\rho_c I T_o}{ma^2 sinh(L/a)}(cosh(s/a) - e^{-2s/r} - e^{-2(L-s)/r}cosh(L/a))$$

$$\omega_3(s) = \frac{2T_o}{ma^2 sinh(L/a)}(cosh(s/a) - e^{-2s/r} - e^{-2(L-s)/r}cosh(L/a)).$$

The correction, therefore, with respect to solution (4.10) is restricted to the boundary layers formed at the two ends, affecting only the shear force, which is order α, and the rotational velocity. Here we find $\omega_3 = 0$ at $s = 0, L$, which differs form the solution given in (4.11). The width of the boundary layer was found to be $1/\delta$.

Next we consider the cable with reversing curvature (figure 4.3), which is the prime example which motivated this analysis. We consider a smooth initial curvature, in the form:
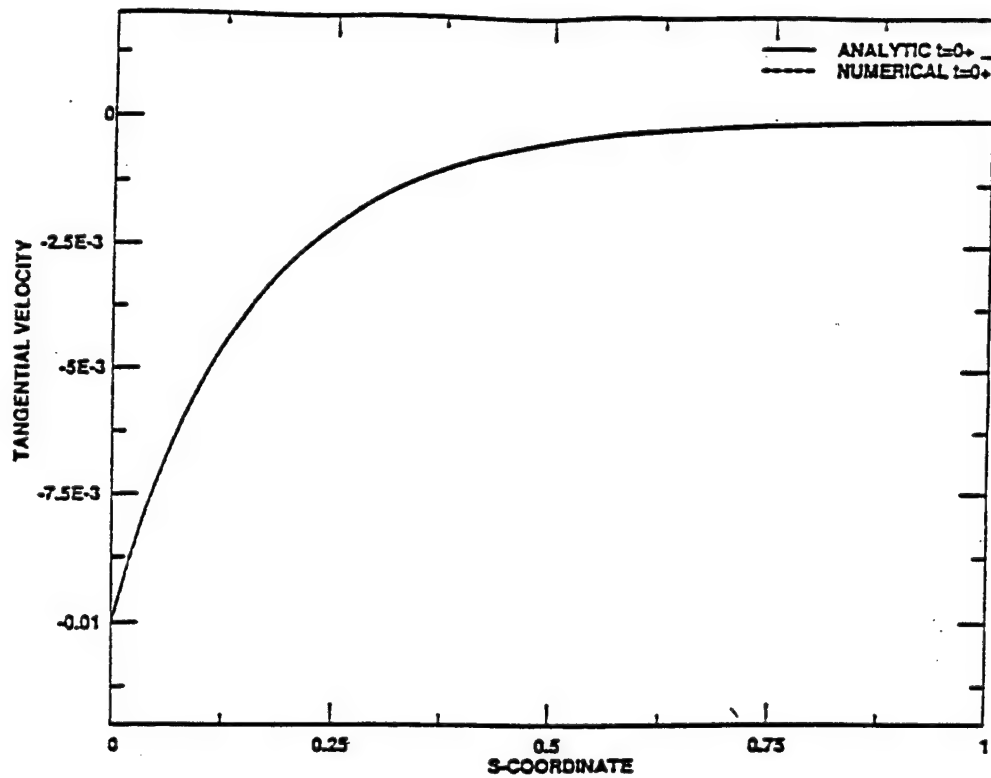
$$\frac{d\phi}{ds} = \frac{tanh(s/\epsilon)}{a} \qquad (4.29)$$

40
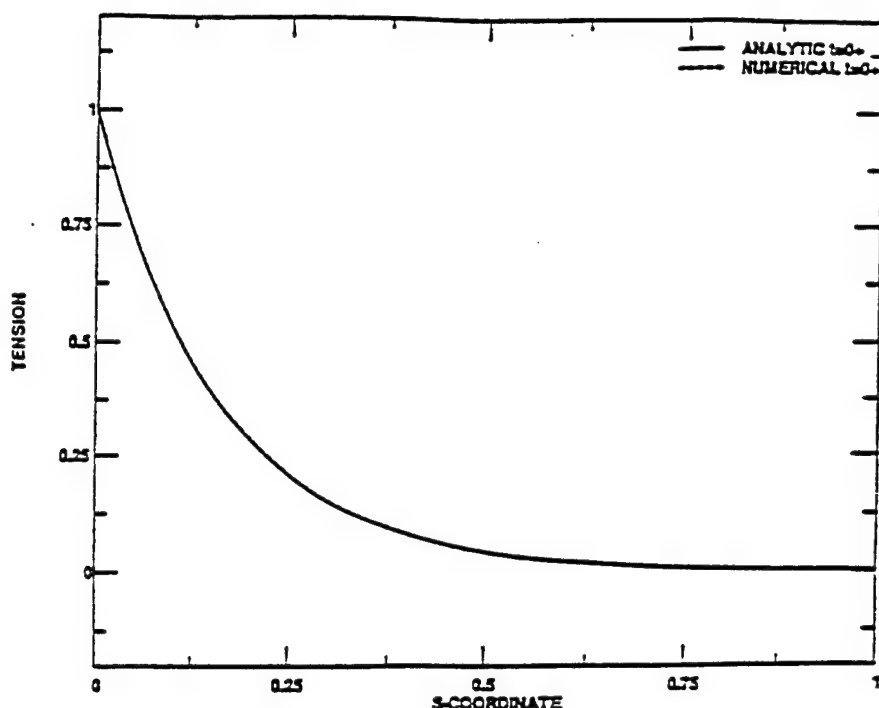
Figure 4.5: Analytically and numerically predicted tension along a cable lying in a circle (figure 4.2) immediately after the application of impulsive loading.

where $\epsilon \ll L$, i.e. the reversal in curvature occurs within a small region. Obviously, ϵ is directly related to the length of the transition region of changing curvature, which in turn depends on the value of the (usually small) bending stiffness of the cable. The initial configuration requires a (small) distributed moment in order to sustain the static shape in the presence of bending stiffness. This moment, however, has an insignificant effect on the developing dynamic response.

A numerical solution of (4.25) for the curvature specified in (4.29) was obtained using centered finite differences. Figure 4.4 shows the tension and rotational velocity along the cable for $\epsilon = 0.01$ and $\delta = 1,000$. The cable length is set equal to 2. As readily seen, a large peak in the rotational velocity occurs at the curvature reversing region, which is inversely proportional to the length over which the curvature reversal occurs (ϵ). Once again the solution for ω_3 contains boundary layers near $s = L$ and the width of the boundary layer depends on δ.

4.6 Comparison of Analytic and Numerical Results

The numerical techniques presented in §3 were used to simulate the examples discussed previously. In particular, the explicit finite difference algorithm was used extensively to model the dynamics in the absence of bending stiffness.

Numerical results were obtained for the cable initially in the form of a circle (figure 4.2). Figures 4.5, 4.6, and 4.7 show simulation results for the tension and normal and tangential velocities, respectively, shortly after the impulsive tension was applied at one end. Also shown are the analytic results derived in §4.3.2. As shown, the two results are nearly indistinguishable.

41
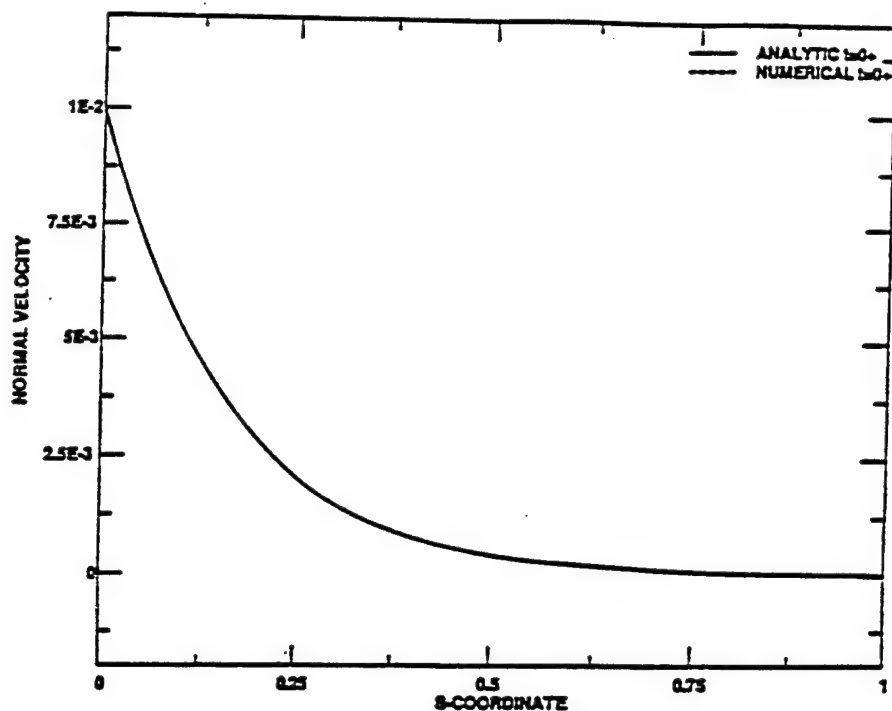
Figure 4.6: Analytically and numerically predicted normal velocity along a cable lying in a circle (figure 4.2) immediately after the application of impulsive loading.

The example involving a cable of reversing curvature (figure 4.3) was simulated numerically as well. A curvature change, as described in §4.3.4 was implemented, using a moderately small value of $\epsilon = 0.01$ to avoid the development of sharp boundary layers. Figure 4.8 shows the normal velocity immediately after the application of the impulsive load (solid line). This solution coincides with the analytic results, provided a sufficient number of nodes are used in the numerical scheme to ensure adequate treatment of the boundary layer-type behavior. As predicted analytically, a steep change in the normal velocity occurs at the point of changing curvature. Also shown is the response at several times after the initial loading. We find that the effect of the large angular velocity imparted at the cable midpoint spreads over an increasingly larger region with time, demonstrating the significance of the mechanism, particularly for small values of ϵ.

In the next section, impulsive tension forces are addressed further, in the context of a harmonically excited hanging chain. In this case, the tension prior to loading varies linearly along the chain length.

42

Figure 4.7: Analytically and numerically predicted tangential velocity along a cable lying in a circle (figure 4.2) immediately after the application of impulsive loading.
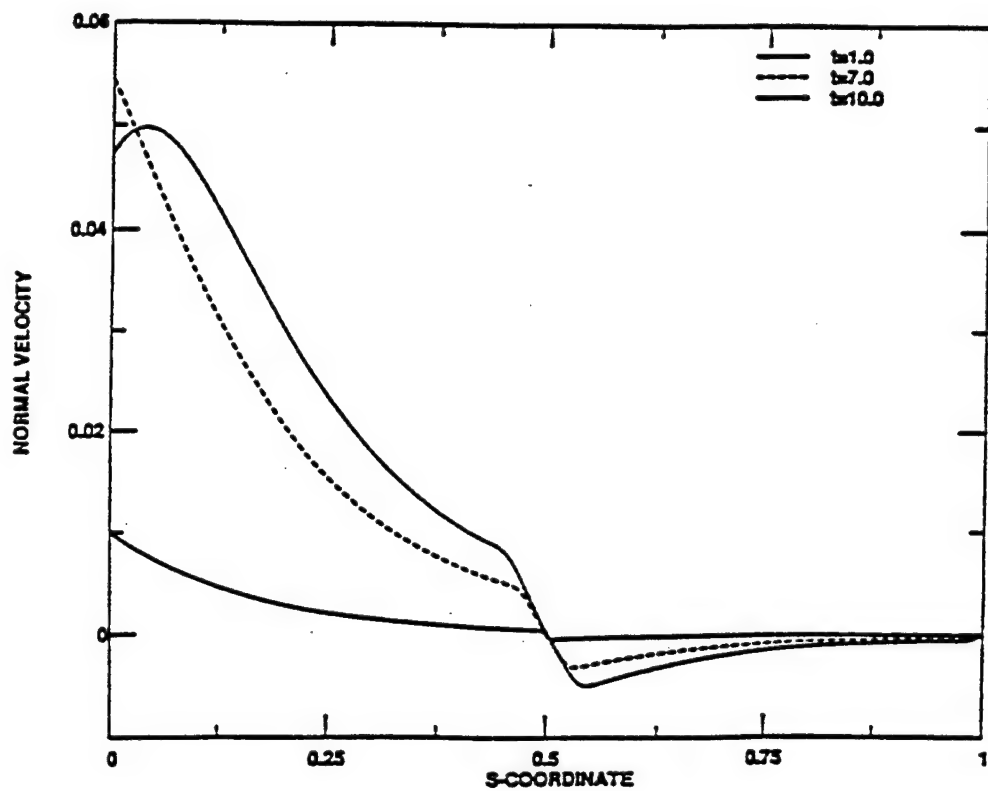
Figure 4.8: Transverse velocity along cable having initial configuration shown in figure 4.3, at three time intervals.

V. ANALYSIS OF RESPONSE OF HANGING CHAIN

5.1 Introduction

A chain hanging freely under its own weight is subject to a static tension component which varies linearly over the chain length, beginning with zero tension at the free boundary. As such, a hanging chain exhibits both high tension behavior (near the top boundary) and low tension behavior (near the free boundary) along its span. Therefore, the hanging chain problem affords an opportunity to study the dynamics in both tension regions as well as the transition between high and low tension behavior.

Herein we investigate the nonlinear dynamics of a hanging chain, driven by a planar harmonic excitation at the top, first analytically and numerically and then experimentally. We consider the dynamics of the chain in air to isolate and study the effects of geometric non-linearities. As detailed by Triantafyllou and Howell (1993), asymptotic results demonstrate a sensitive dependence on excitation frequency and amplitude. Results for moderately large excitation amplitudes identify the existence of separate regions of stable two-dimensional and stable three-dimensional response as a function of frequency, as well as a distinct region in which all steady state solutions are found to be unstable. Numerical and experimental studies were conducted to confirm these findings.

The finding of a three-dimensional response to a planar excitation has been shown previously by other researchers studying the nonlinear dynamics of cables or strings as well. Nayfeh (1979) and then Miles (1984) studied the nonlinear dynamics of a stretched string, pinned at one end and subject to a harmonic planar excitation over its length. They found that three-dimensional whirling motions develop over a discrete range of excitation frequencies. Perkins (1991) found similar results for a suspended shallow sag cable subject to an end point excitation. These previously studied problems differ from the present analysis in that they each involved a constant static tension along the cable or string. To the author's knowledge, this is the first asymptotic analysis of a chain with variable static tension.

In this section, we develop in detail the principal derivations and asymptotic results first presented by Triantafyllou and Howell (1993). In addition, numerical and experimental results which were used to verify the asymptotic solutions are discussed. These results have been summarized in a second paper by Triantafyllou and Howell (1992). Finally, we concentrate on the response of the chain for larger excitation amplitudes.

5.2 Formulation of the Problem

The problem under consideration is the three-dimensional dynamics of a chain, hanging freely under its own weight, as shown in figure 5.1. Here we simplify the governing equations derived in §2 in the following manner. First, chains, unlike cables, are perfectly flexible and therefore no forces arise due to bending stiffness. Secondly, because we are considering the dynamics in air, the hydrodynamic effects of added mass and drag are neglected. This creates some complications in that in the absence of damping, transient motions will not decay. We therefore will consider the affect of incorporating a linear drag model in §5.3.2. Finally, the chain is considered to be inextensible. Due to the condition for zero tension at the lower end, this assumption is valid provided the excitation frequencies
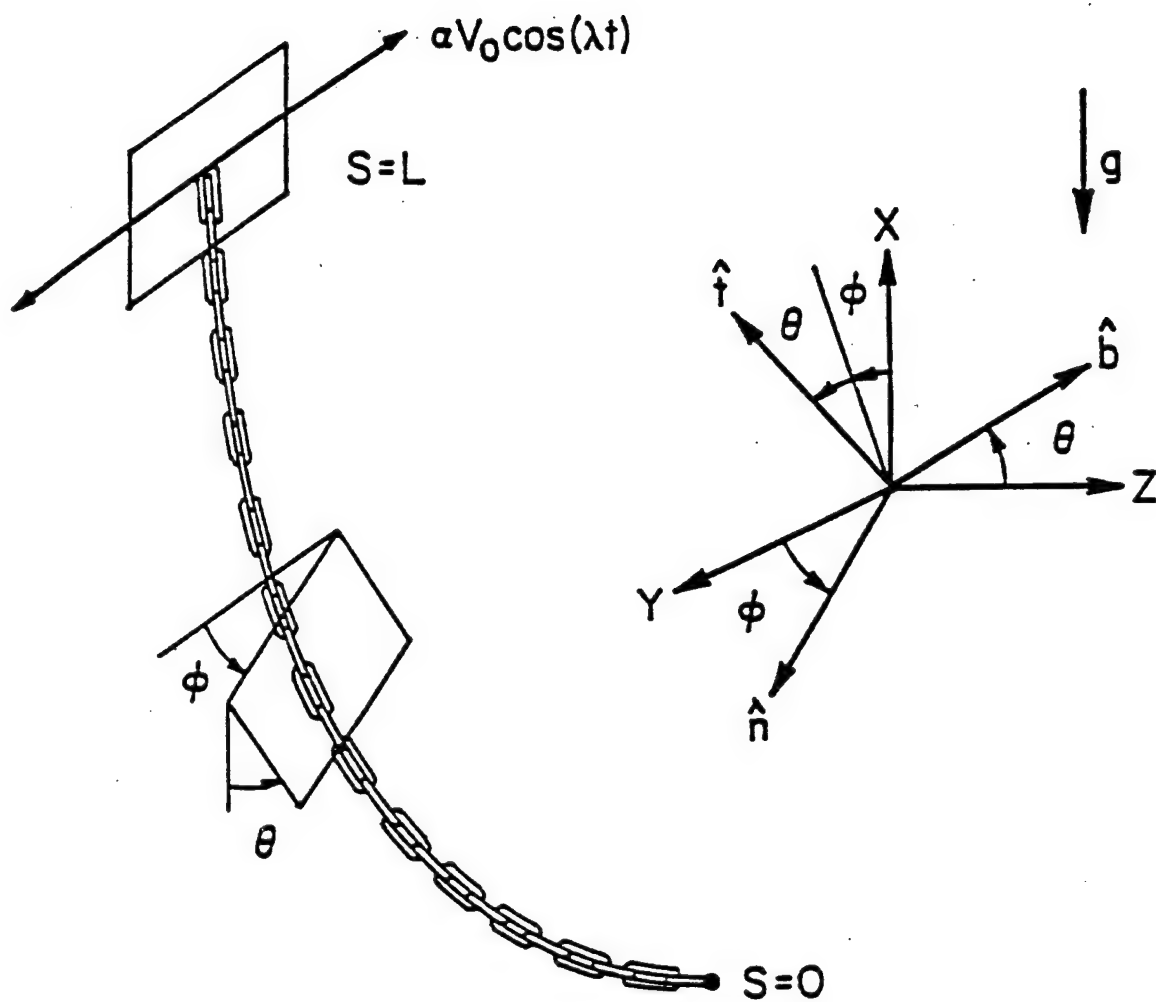
Figure 5.1: Cable configuration and coordinate system.

are small compared to the first elastic natural frequency and the imposed velocities are small compared to the speed of elastic waves (Triantafyllou and Howell, 1992).

The governing equations and compatibility relations for the hanging chain problem are found to be

$$m(\frac{\partial u}{\partial t} + \frac{\partial \theta}{\partial t} w - \frac{\partial \phi}{\partial t} v \cos(\theta)) = \frac{\partial T}{\partial s} - mg \cos(\phi) \cos(\theta) \qquad (5.1)$$

$$m(\frac{\partial v}{\partial t} + \frac{\partial \phi}{\partial t} u \cos(\theta) + \frac{\partial \phi}{\partial t} w \sin(\theta)) = T \frac{\partial \phi}{\partial s} \cos(\theta) + mg \sin(\phi)$$

$$m(\frac{\partial w}{\partial t} - \frac{\partial \phi}{\partial t} v \sin(\theta) - \frac{\partial \theta}{\partial t} u) = -T \frac{\partial \theta}{\partial s} - mg \cos(\phi) \sin(\theta)$$

$$\frac{\partial v}{\partial s} + \frac{\partial \phi}{\partial s} u \cos(\theta) + \frac{\partial \phi}{\partial s} w \sin(\theta) = \frac{\partial \phi}{\partial t} \cos(\theta)$$

$$\frac{\partial w}{\partial s} - \frac{\partial \phi}{\partial s} v \sin(\theta) - \frac{\partial \theta}{\partial s} u = -\frac{\partial \theta}{\partial t}$$

$$\frac{\partial u}{\partial s} + \frac{\partial \theta}{\partial s} w - \frac{\partial \phi}{\partial s} v \cos(\theta) = 0.$$

The chain is considered to be excited harmonically at the top. This excitation is confined to the global x-y plane and the excitation frequency λ is chosen close to one of the natural frequencies, defined as ω. A small transverse velocity is imposed at the top, given by:

$$v(t, s = L) = \alpha V_o cos(\lambda t). \qquad (5.2)$$

where V_o is the velocity amplitude corresponding to a motion amplitude $Y_o = V_o/\lambda$ and α is a small positive number, $\alpha \ll 1$. In addition, zero tension is imposed at the lower end ($s = 0$) and the velocities, u and w are set to zero at the upper boundary ($s = L$).

Due to the direction of the excitation, we adopt the terminology that v and ϕ represent the in-plane velocity and angle, respectively, while w and θ represent these quantities in the out-of-plane direction.

5.3 Analytic Analysis

We derive the analytic solutions using asymptotic techniques. The main goal of the analytic studies was to determine the response of the chain to a wide range of excitation frequencies and amplitudes. In particular, the motions at the free end of the chain are discussed.

5.3.1 ASYMPTOTIC SOLUTION

The first step toward obtaining an analytic solution of the hanging chain equations was to employ a perturbation expansion. This expansion is made in terms of the small parameter ϵ, where ϵ is given by $\alpha = \epsilon^3$. The nature of the equations dictates that the tangential velocity and tension are even functions in ϵ while the remaining variables include only odd terms. Therefore, incorporating the static solution, the perturbation expansion can be written as follows:

47

$$u(s,t) = \epsilon^2 u_2(s,t) + \epsilon^4 u_4(s,t) + O(\epsilon^6) \qquad (5.3)$$

$$v(s,t) = \epsilon v_1(s,t) + \epsilon^3[v_3(s,t) + V_o cos(\lambda t)\frac{s}{L}] + O(\epsilon^5)$$

$$w(s,t) = \epsilon w_1(s,t) + \epsilon^3 w_3(s,t) + O(\epsilon^5)$$

$$\phi(s,t) = \epsilon\phi_1(s,t) + \epsilon^3[\phi_3(s,t) + \frac{Y_o}{L}sin(\lambda t)] + O(\epsilon^5)$$

$$\theta(s,t) = \epsilon\theta_1(s,t) + \epsilon^3\theta_3(s,t) + O(\epsilon^5)$$

$$T(s,t) = mgs + \epsilon^2 T_2(s,t) + \epsilon^4 T_4(s,t) + O(\epsilon^6).$$

The expanded variables given by (5.3) are substituted into the governing equations and compatibility relations and terms of each order in ϵ are grouped together. The equations to first order in ϵ are found to be

$$m\frac{\partial v_1}{\partial t} = mgs\frac{\partial \phi_1}{\partial s} + mg\phi_1 \qquad (5.4)$$

$$\frac{\partial \phi_1}{\partial t} = \frac{\partial v_1}{\partial s}$$

$$m\frac{\partial w_1}{\partial t} = -mgs\frac{\partial \theta_1}{\partial s} - mg\theta_1$$

$$\frac{\partial \theta_1}{\partial t} = -\frac{\partial w_1}{\partial s}.$$

With regard to the first-order equations, two points are worthy of note. First, as expected, these equations represent the linear solution of the hanging chain problem. Secondly, no coupling between in-plane and out-of-plane motions exists to first order.

The first-order equations can be reduced to the following:

$$\frac{\partial^2 \phi_1}{\partial t^2} = 2g\frac{\partial \phi_1}{\partial s} + gs\frac{\partial^2 \phi_1}{\partial s^2} \qquad (5.5)$$

$$\frac{\partial^2 \theta_1}{\partial t^2} = 2g\frac{\partial \theta_1}{\partial s} + gs\frac{\partial^2 \theta_1}{\partial s^2}.$$

These equations are straight-forward to solve using the method of separation of variables (Carrier and Pearson, 1988) and the solution is given by

$$\phi_1 = A(t)\frac{J_1(z)}{z} \qquad (5.6)$$

$$\theta_1 = B(t)\frac{J_1(z)}{z}.$$

where $z = 2\omega\sqrt{s/g}$, $J_n(z)$ denotes the Bessel function of the first kind and order n, and $A(t)$ and $B(t)$ represent time dependent amplitudes. In concurrence with the method of multiple time scales (Bender and Orszag, 1978) the unknown amplitudes are decomposed into functions of two time scales, t and τ, where τ represents the long time scale, which is given by $\tau = \epsilon^3 t$, anticipating the final result. This relation between time scales was selected because secular terms first arise at order ϵ^3. The amplitudes are then expressed as follows:

48

$$A(t) = A_1(\tau)e^{i\omega t} + cc \tag{5.7}$$
$$B(t) = B_1(\tau)e^{i\omega t} + cc$$

where i is the imaginary unit, cc denotes the complex conjugate of the preceding quantity. Using these results, we may now solve for the first-order velocities.

$$v_1 = -\frac{g}{2\omega}(iA_1e^{i\omega t} + cc)J_0(z) \tag{5.8}$$
$$w_1 = \frac{g}{2\omega}(iB_1e^{i\omega t} + cc)J_0(z).$$

The natural frequencies are obtained from the requirement that, to first order in ϵ, the transverse velocities v and w are zero at $s = L$. This results in the classical equation for the natural frequencies of a hanging chain, as given by

$$J_0(z_o) = 0 \tag{5.9}$$

where

$$z_o = 2\omega\sqrt{\frac{L}{g}}. \tag{5.10}$$

The second order equations in ϵ are found to be given by

$$m(\frac{\partial u_2}{\partial t} + w_1\frac{\partial \theta_1}{\partial t} - v_1\frac{\partial \phi_1}{\partial t}) = \frac{\partial T_2}{\partial s} + mg\frac{{\phi_1}^2 + {\theta_1}^2}{2} \tag{5.11}$$
$$\frac{\partial u_2}{\partial s} = v_1\frac{\partial \phi_1}{\partial s} - w_1\frac{\partial \theta_1}{\partial s}.$$

Solving these equations for T_2 and u_2 and imposing $u_2(t, s = L) = 0$, we find

$$u_2 = \frac{g}{4\omega}((A^2 + B^2)e^{2i\omega t} + cc)h_1(z) \tag{5.12}$$
$$T_2 = \frac{mg^2}{8\omega^2}[(2AA^* + 2BB^*)J_1(z)^2 - ((A^2 + B^2)e^{2i\omega t} + cc)h_2(z)]$$

where $*$ denotes the complex conjugate and the functions $h_1(z)$ and $h_2(z)$ are defined as follows:

$$h_1(z) = J_1(z)^2 - J_2(z)J_0(z) - J_1(z_o)^2$$
$$h_2(z) = 2z^2(J_0(z)^2 + J_1(z)^2) - J_1(z)^2 - 2zJ_1(z)J_0(z) - z^2J_1(z_o)^2.$$

Finally, we proceed to investigate the third-order equations in ϵ. The third-order equations are found to be given by

$$\frac{\partial v_3}{\partial t} - gs\frac{\partial \phi_3}{\partial s} - g\phi_3 = \frac{Y_o}{2L}(s\lambda^2 + g)(ie^{i\lambda t} + cc)$$
$$-\frac{\partial v_1}{\partial \tau} - \frac{\partial \phi_1}{\partial t}(u_2 + \theta_1 w_1) + \frac{T_2}{m}\frac{\partial \phi_1}{\partial s} - gs\frac{{\theta_1}^2}{2}\frac{\partial \phi_1}{\partial s} - g\frac{{\phi_1}^3}{6} \tag{5.13}$$

49

$$\frac{\partial w_3}{\partial t} + gs\frac{\partial \theta_3}{\partial s} + g\theta_3 =$$

$$-\frac{\partial w_1}{\partial \tau} + u_2\frac{\partial \theta_1}{\partial t} + \theta_1 v_1\frac{\partial \phi_1}{\partial t} - \frac{T_2}{m}\frac{\partial \theta_1}{\partial s} + g\left(\frac{\theta_1{}^3}{6} + \frac{\theta_1\phi_1{}^2}{2}\right)$$

$$\frac{\partial \phi_3}{\partial t} - \frac{\partial v_3}{\partial s} = -\frac{\partial \phi_1}{\partial \tau} + \frac{\theta_1{}^2}{2}\frac{\partial \phi_1}{\partial t} + \frac{\partial \phi_1}{\partial s}(u_2 + \theta_1 w_1)$$

$$\frac{\partial \theta_3}{\partial s} + \frac{\partial w_3}{\partial s} = -\frac{\partial \theta_1}{\partial \tau} + u_2\frac{\partial \theta_1}{\partial s} + \theta_1 v_1\frac{\partial \phi_1}{\partial s}$$

The expressions given by (5.6), (5.8), and (5.12) are introduced into (5.13) and the spatial dependence is eliminated using a Galerkin procedure in which the resulting equations are multiplied by the zeroth order Bessel function, corresponding to the nearest natural frequency, and then integrating along the chain length. Finally, the secular terms are removed from the resulting equations by imposing the following conditions:

$$\frac{1}{\omega}\frac{dA_1}{d\tau} = -[f_1(\sigma+1)^2 + f_2]e^{i\sigma\tau} + i[\gamma_0 A_1^2 A_1^* + \gamma_1 B_1^2 A_1^*] \qquad (5.14)$$

$$\frac{1}{\omega}\frac{dB_1}{d\tau} = i[\gamma_0 B_1^2 B_1^* + \gamma_2 A_1^2 B_1^* + \gamma_3 A_1 A_1^* B_1].$$

Here the following definitions are used:

$$f_1 = \frac{Y_o\alpha_2}{4\alpha_1 L}$$

$$f_2 = \frac{Y_o\alpha_0}{\alpha_1 L}$$

$$\gamma_0 = \frac{\alpha_3}{2\alpha_1}$$

$$\gamma_1 = \frac{\alpha_4}{2\alpha_1}$$

$$\gamma_2 = \frac{\alpha_5}{2\alpha_1}$$

$$\gamma_3 = \frac{\alpha_6}{2\alpha_1}$$

where

$$\alpha_0 = \int_0^{z_o} z J_0(z)dz$$

$$\alpha_1 = \int_0^{z_o} z J_0(z)^2 dz$$

$$\alpha_2 = \int_0^{z_o} z^3 J_0(z)dz$$

$$\alpha_3 = \int_0^{z_o} z J_0(z)h_3(z)dz.$$

$$\alpha_4 = \int_0^{z_o} \frac{J_0(z)}{z}[h_2(z)J_2(z) + J_2(z)J_1(z)^2 - zh_1(z)J_1(z) - 2J_0(z)J_1(z)^2]dz$$

$$\alpha_5 = \int_0^{z_o} \frac{J_0(z)}{z^2}[zh_2(z)J_2(z) - 2J_1(z)^3 - z^2h_1(z)J_1(z) - 2zJ_0(z)J_1(z)^2]dz$$

$$\alpha_6 = \int_0^{z_o} \frac{J_0(z)}{z^2}[4zJ_0(z)J_1(z)^2 - 4J_1(z)^3 - 2zJ_1(z)^2J_2(z)]dz$$

50

$$h_3(z) = -\left[\frac{J_1(z)h_1(z)}{z} + (2J_1(z)^2 - h_2(z))\frac{J_2(z)}{z^2} + \frac{2J_1(z)^3}{z^3}\right].$$

Note that the amplitude of excitation Y_o is incorporated in the terms f_1 and f_2 and the excitation frequency is expressed in terms of the detuning σ, where

$$\sigma = (\frac{\lambda}{\omega} - 1). \tag{5.15}$$

The amplitudes are further decomposed as follows:

$$\begin{aligned} A_1(\tau) &= a(\tau)e^{i\xi_1(\tau)} \\ B_1(\tau) &= b(\tau)e^{i\eta_1(\tau)}. \end{aligned} \tag{5.16}$$

Substitution of these expressions into (5.14) and grouping real and imaginary terms yields:

$$\frac{1}{\omega}\frac{dp}{d\tau} = q[\sigma - \gamma_0(q^2 + p^2) - \gamma_1(s^2 - r^2)] - 2\gamma_1 prs \tag{5.17}$$

$$\frac{1}{\omega}\frac{dq}{d\tau} = -[f_1(\sigma + 1)^2 + f_2] - p[\sigma - \gamma_0(q^2 + p^2) + \gamma_1(s^2 - r^2)] + 2\gamma_1 qrs$$

$$\frac{1}{\omega}\frac{dr}{d\tau} = s[\sigma - \gamma_0(r^2 + s^2) - \gamma_2(q^2 - p^2) - \gamma_3(p^2 + q^2)] - 2\gamma_2 pqr$$

$$\frac{1}{\omega}\frac{ds}{d\tau} = -r[\sigma - \gamma_0(r^2 + s^2) + \gamma_2(q^2 - p^2) - \gamma_3(p^2 + q^2)] - 2\gamma_2 pqs.$$

Note that following Miles (1984), the phase angles have been removed by setting

$$\begin{aligned} p &= a(\tau)sin(\xi) \\ q &= a(\tau)cos(\xi) \\ r &= b(\tau)sin(\eta) \\ s &= b(\tau)cos(\eta) \end{aligned} \tag{5.18}$$

where $\xi = \sigma\tau - \xi_1$ and $\eta = \sigma\tau - \eta_1$.

Steady state solutions are given by the fixed points of (5.17). Setting the time derivatives equal to zero, two classes of fixed points are determined. The first class corresponds to a 2-D response, where

$$p = \pm a \tag{5.19}$$

$$q = r = s = 0. \tag{5.20}$$

From these fixed points, the 2-D solution is given by the following:

$$\sigma a \pm [f_1(\sigma + 1)^2 + f_2] - \gamma_0 a^3 = 0. \tag{5.21}$$

The second class of fixed points correspond to 3-D motions. The fixed points are given by

$$\begin{aligned} p &= \pm a \\ q &= 0 \\ r &= \pm b\cos(\frac{N\pi}{2}) \\ s &= \pm b\sin(\frac{N\pi}{2}). \end{aligned} \tag{5.22}$$

51

Substitution of these fixed points into (5.17) yields the following:

$$\sigma \pm \frac{[f_1(\sigma+1)^2 + f_2]}{a} - \gamma_0 a^2 - \gamma_1 b^2 (-1)^N = 0 \qquad (5.23)$$
$$\sigma - \gamma_0 b^2 - \gamma_2 a^2 (-1)^N - \gamma_3 a^2 = 0.$$

The solutions given by (5.21) and (5.23) are used to generate response amplitude versus frequency (or detuning) curves for a fixed excitation amplitude. However, we must first determine if the corresponding solutions are stable.

5.3.2 STABILITY ANALYSIS

Stability of the solutions is determined by investigating the eigenvalues of the Jacobian matrix formed from (5.17). In general, the real part of all four eigenvalues must be less than zero for the solution to be stable to small perturbations (Jordan and Smith, 1987). Otherwise, small perturbations will not decay in time.

In the absence of damping, the Jacobian matrix for this problem has zeros along the main diagonal and is separable into two 2×2 matrices. As such, all eigenvalues occur in complex conjugate pairs. Therefore, the only solutions which do not grow exponentially in time are those in which the eigenvalues are purely imaginary. Generally, solutions with purely imaginary eigenvalues are considered neutrally stable and are sensitive to nonlinearities.

Incorporating a small degree of linear damping into the governing equations introduces negative terms along the main diagonal of the Jacobian matrix. The net effect is that all purely imaginary eigenvalues develop a negative real component. In other words, all neutrally stable centers become stable spirals or stable nodes, depending on the amount of damping. This finding is demonstrated in figure 5.2 in which the eigenvalues near a saddle-node bifurcation are shown with and without damping. As a result, for this analysis all solutions with purely imaginary eigenvalues will also be considered as stable.

5.3.3 RESULTS

Analytic results, for detuning values near the second natural frequency, are presented for an excitation amplitude of 0.0087L. Figures 5.3 and 5.4 show the in-plane and out-of-plane velocities, respectively, at the free end of the chain. The velocities are nondimensionalized by $\sqrt{gL}$, which is directly proportional to ωL. Note that for clarity, only one branch of the two-dimensional solution is shown in figure 5.4.

As shown, several bifurcations, labeled from A to D, were found to occur. The bifurcations at A and B are saddle-node bifurcations, while a pitchfork bifurcation occurs at D. At C, the stability of the three-dimensional branch changes suddenly for increasing detuning values. The variation of the eigenvalues along the associated three-dimensional branch is shown in figure 5.5. Based on the variation of the eigenvalues, the stability transition at C is identified as a Hamiltonian-Hopf bifurcation. This class of bifurcation has been identified by other researchers in the past (Tsai et al., 1990).

As a result of the bifurcations that occur, a region develops in which no stable response is predicted. For the example shown, this region lies between $-0.08 \leq \sigma \leq -0.035$. The dynamics within this region were investigated through numerical and experimental means, as discussed later in this section.
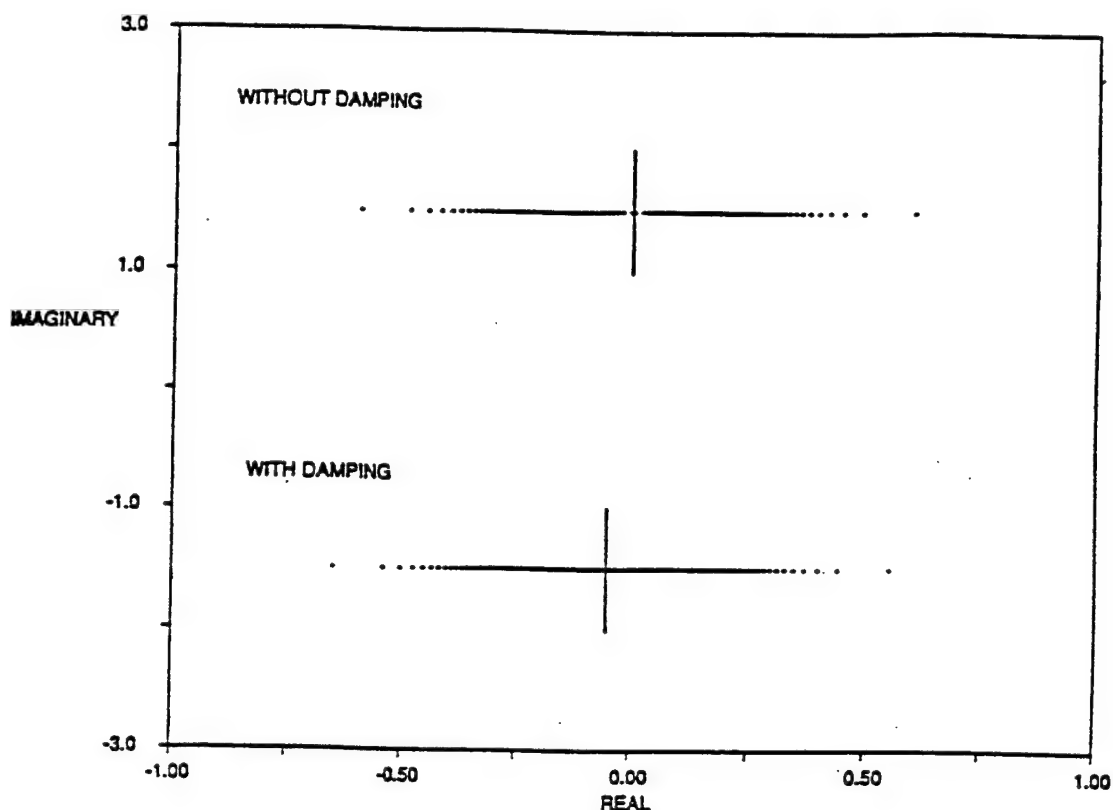
Figure 5.2: Effect of linear damping on eigenvalues near a saddle-node bifurcation.

As the excitation amplitude is increased, the unstable region increases and shifts to a lower frequency range. This is demonstrated in figure 5.6, in which the excitation amplitude is shown versus the unstable frequency region. As one would expect, the size of the region vanishes as the excitation amplitude approaches zero.

5.4 Numerical Solution

The purpose of the numerical analysis was twofold. First, verification of the stable response regions determined analytically was sought. By solving the fully nonlinear equations, the effect of higher-order correction terms beyond ϵ^3 could be determined. Secondly, the numerical approach provides a means with which to verify the existence of the unstable response region and investigate the dynamics within the region.

The second-order implicit finite difference approximation scheme described in §3 was applied to the set of equations given by (5.1). For simulations involving moderately large excitation amplitudes the tension remains finite; however, for larger excitation amplitudes, as discussed in §5.6, the tension does vanish and a small amount of bending stiffness was incorporated for stability.

Numerical studies were first conducted for detuning values at which the analytic technique predicted a stable response. As shown in figure 5.7, good agreement was obtained between the analytical and numerical solutions. Both the character of the response, i.e. stable 2-D or 3-D, and the magnitude compared favorably. It should be noted that a small amount of linear damping, corresponding to less than 1 percent critical, was incorporated to eliminate starting transients.

53
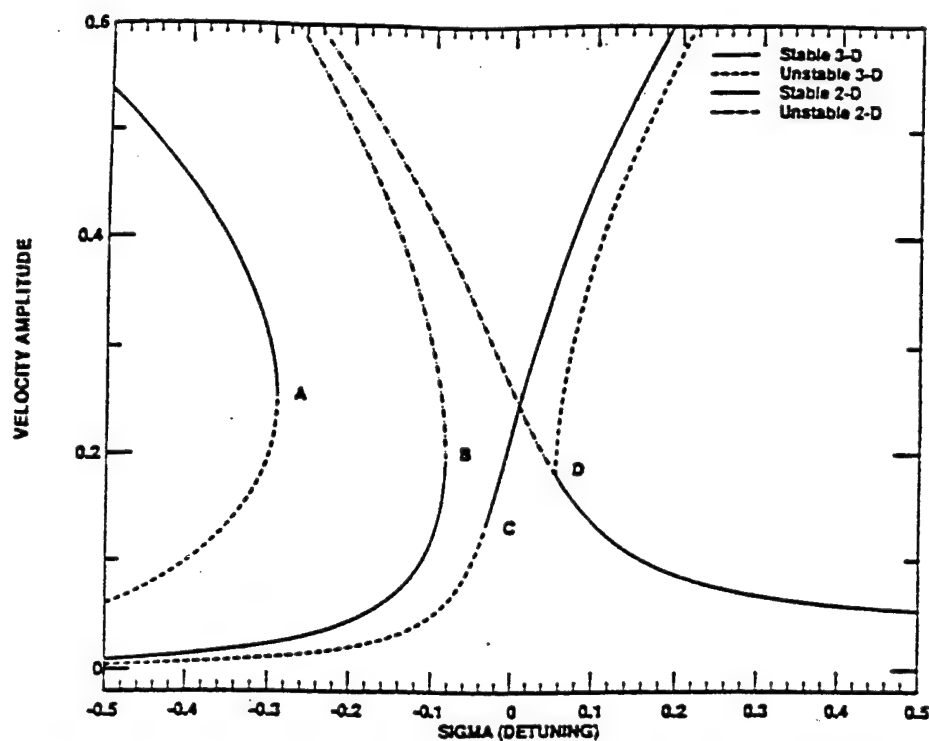
Figure 5.3: Stability curves: In-plane velocity at lower end versus detuning for excitation amplitude $Y_o = 0.0087L$, near the second natural frequency.
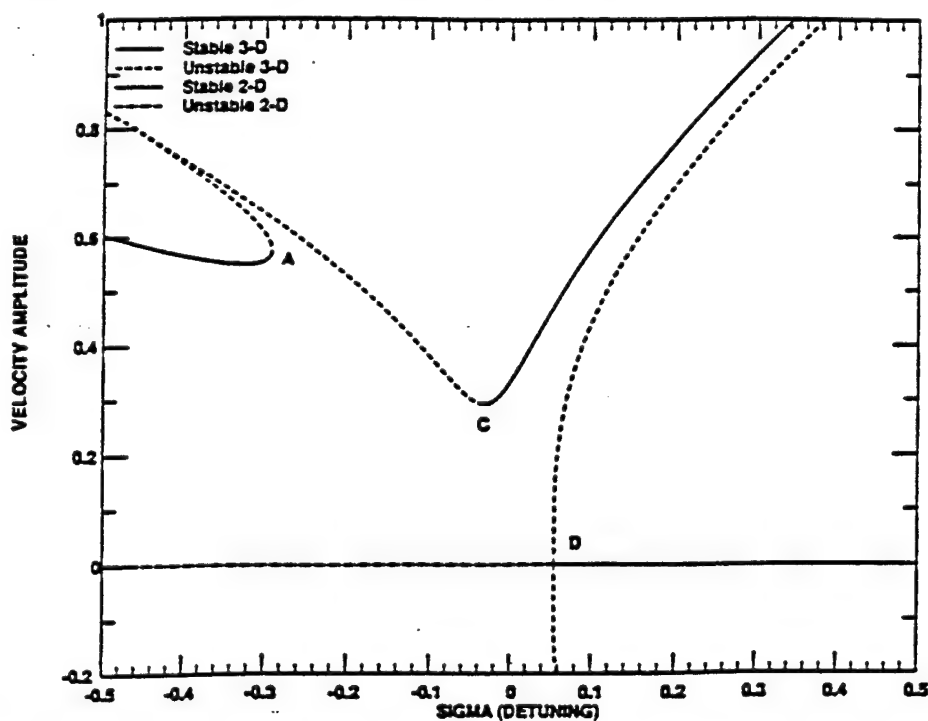
Figure 5.4: Stability curves: Out-of-plane velocity at lower end versus detuning for excitation amplitude $Y_o = 0.0087L$, near the second natural frequency.
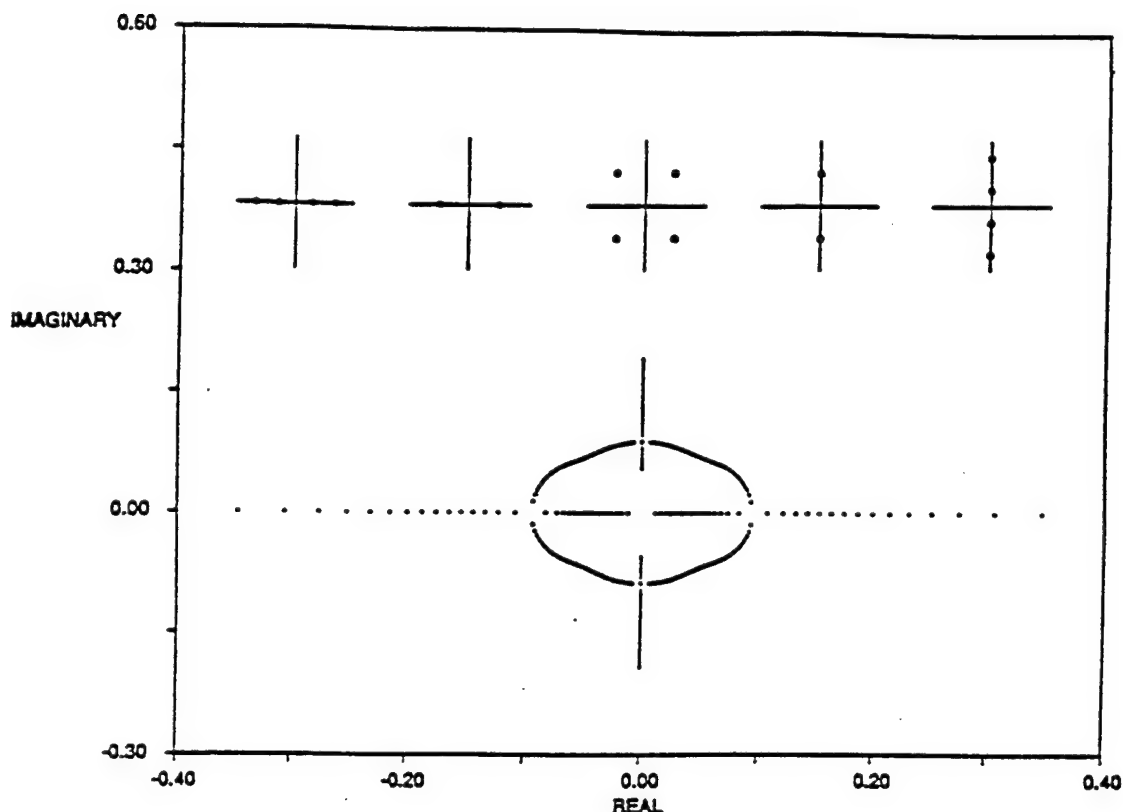
Figure 5.5: Hamiltonian-Hopf bifurcation: Variation of eigenvalues along 3-D branch.

A numerical analysis of the unstable region ($-0.08 \leq \sigma \leq -0.035$) was also conducted and results are presented for σ = -0.06 and -0.05. Figure 5.8 shows the time series records for the in-plane and out-of-plane transverse velocities at the free end of the chain for σ = -0.06. The response is characterized by slightly irregular beating, despite the fact that sufficient time has elapsed to eliminate starting transients. The power spectrum for the in-plane response (figure 5.9) shows a widening of the frequency content around the frequency of excitation. Further insight into the nature of the response is provided by constructing a Poincare plot (figure 5.10) (Berg et al., 1984). As shown, at this excitation frequency the beating motion is only slightly irregular and the response is close to quasi-periodic.

Time series records for the detuning value σ = -0.05, which lies further inside the unstable response region, are shown in figure 5.11. As shown, the response is characterized by irregular beating and the associated power spectra (figure 5.12) also demonstrates a widening of the spectrum near the excitation frequency. The Poincare plot (figure 5.13) exhibits a much more detailed structure than for the previous case.

Simulations were also conducted in which, after the starting transients had decayed, damping was removed using a linear ramping function. Steady state solutions were found to be only slightly affected. However, for simulations within the unstable frequency region, the chain was found to lose tension and collapse. This prevented obtaining long time series records, as required for Poincare plots. This topic is addressed further in §5.6.

55
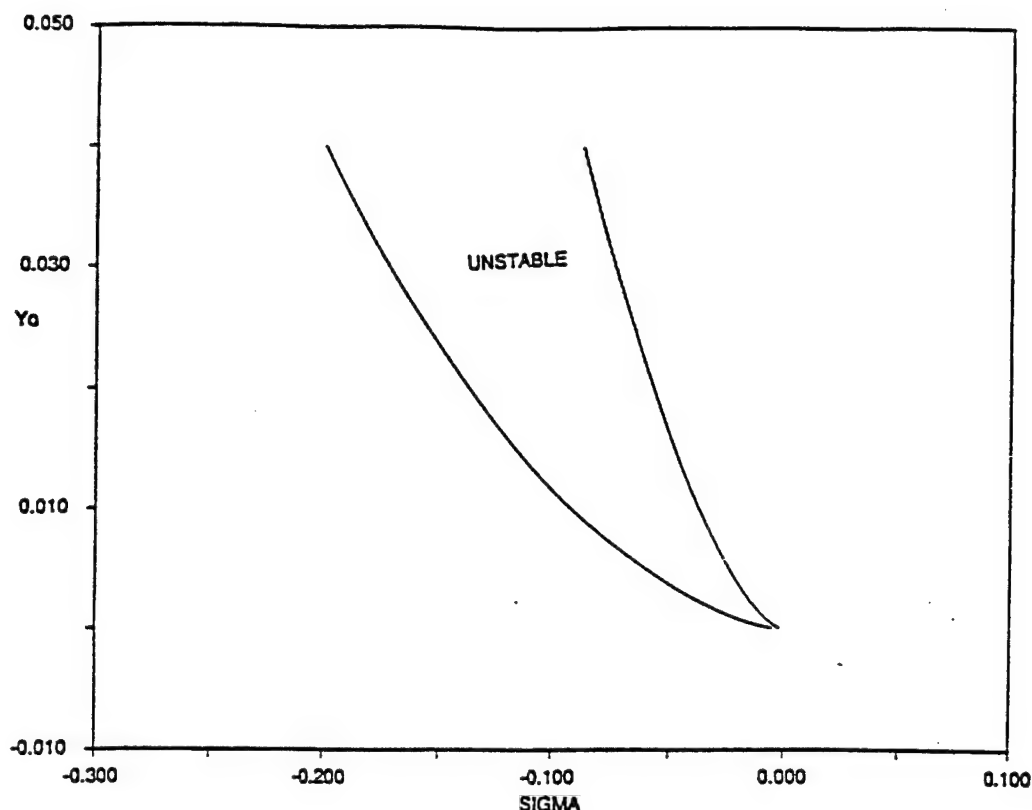
Figure 5.6: Bifurcation diagram: Excitation amplitude versus frequency region in which all stationary solutions are predicted to be unstable.

5.5 Experimental Study

Experiments were conducted to verify the analytic and numerical results. The relative simplicity of the physical problem under study allowed for a simple experimental setup. However, the analytic results show a sensitive dependence on the excitation frequency and amplitude, therefore, strict control was maintained over these two input parameters.

5.5.1 EXPERIMENTAL SETUP

Experiments were conducted at the MIT Ocean Engineering Testing Facility. A 1.75 meter chain was selected, having its second natural frequency at 1.04 hertz. Excitation of the chain was accomplished by a LINTECH leadscrew positioning table, with a travel of ±8.5 centimeters, driven by a microprocessor-controlled SEIBERCO AIM-3400 closed-loop digital servomotor. The tracking signal input to the servo controller (corresponding to the desired motion at the top of the chain) was calculated in real time, by a NEC Powermate 1 286-class computer, from an initial user specified set of parameters and generated with the help of an onboard METRABYTE DASH-16 12 bit D/A converter. An analysis of the system determined that errors in the excitation frequency and amplitude were maintained below 1 and 5 percent, respectively. An overview of the experimental setup is shown in figure 5.14..

Several points along the chain were illuminated, using cotton balls soaked in a light emitting fluid, and their in-plane and out-of-plane displacements recorded on video tape

56
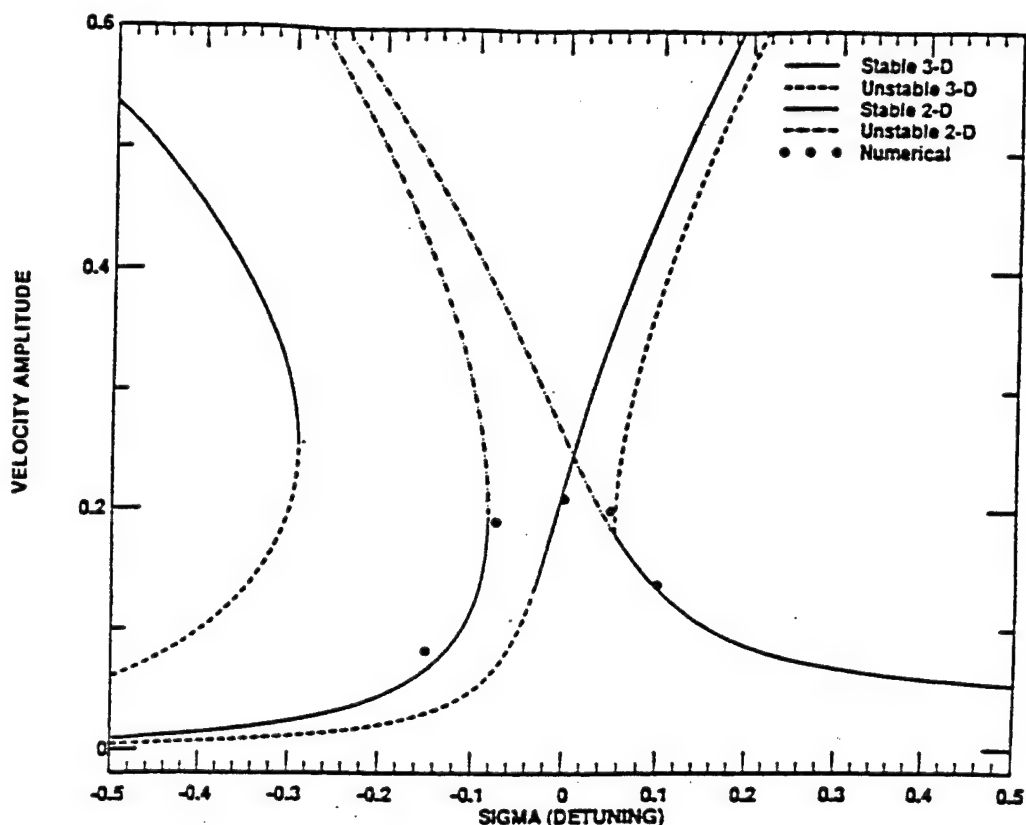
Figure 5.7: Numerical results (circles) compared with perturbation results (lines): In-plane velocity at lower end for excitation amplitude $Y_o = 0.0087L$.

using two separate PANASONIC PV160 video cameras. Displacement time series records were then generated from the video data using a MOTION ANALYSIS VP110 motion analyzer, located at the Woods Hole Oceanographic Institute, which calculates the center of intensity and resulting motion of each light source on the chain.

5.5.2 EXPERIMENTAL DATA

A number of experimental runs were conducted for detuning values at which a stable response was predicted analytically. Good agreement was obtained between methods, as shown in figure 5.15. The character of the response, as well as the amplitude, matched favorably and the results proved stable to perturbations.

Based on preliminary experimental runs, the frequency region characterized by irregular response appeared to be shifted to slightly higher frequency values than predicted analytically. This trend is apparent in figure 5.15. Overall, however, the shift in frequency was found to be less than 2 percent.

Time series records, presented in figures 5.16 and 5.17, show the experimentally obtained in-plane and out-of-plane velocities at the free-end for detuning values of -0.028 and -0.047, respectively. As shown, the response is irregular, despite ramping the excitation amplitude up to the desired value and allowing sufficient time for starting transients to decay. The associated power spectra (figures 5.18 and 5.19) show a marked widening of the spectrum, around the excitation frequency. This is in contrast to the narrow banded
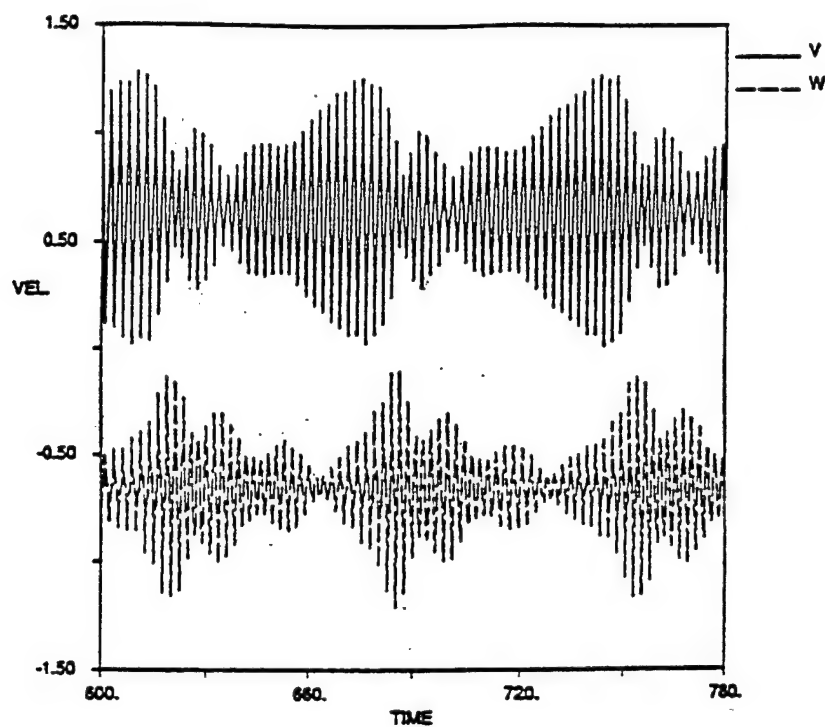
Figure 5.8: Numerical results: Time series record for in-plane and out-of-plane velocities at free end, with excitation amplitude $Y_o = 0.0087L$ and detuning $\sigma = -0.06$
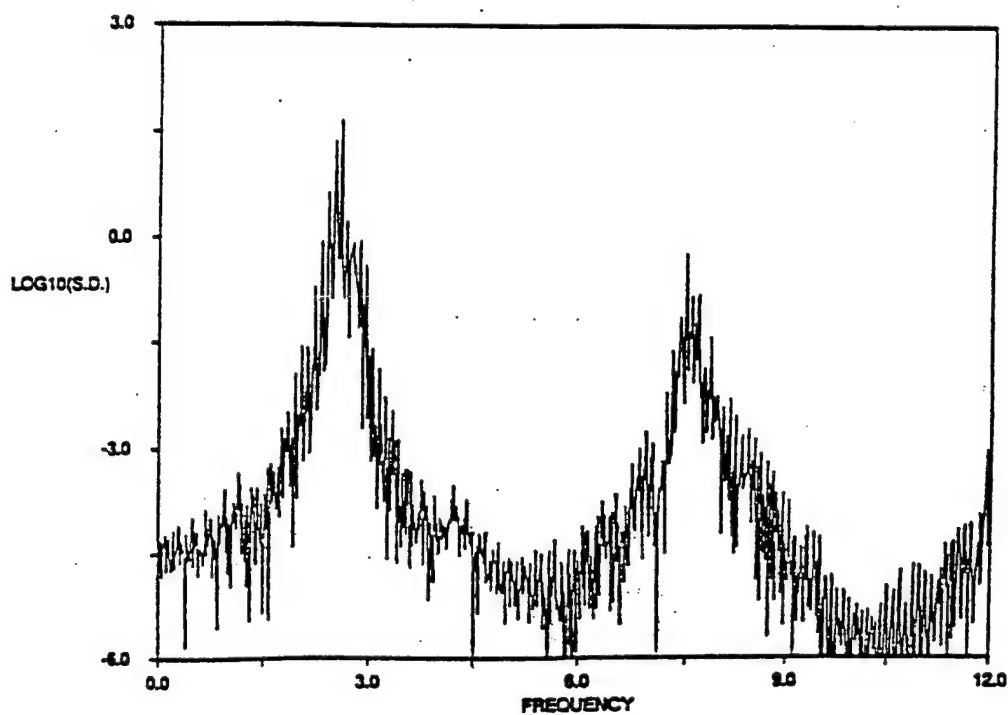
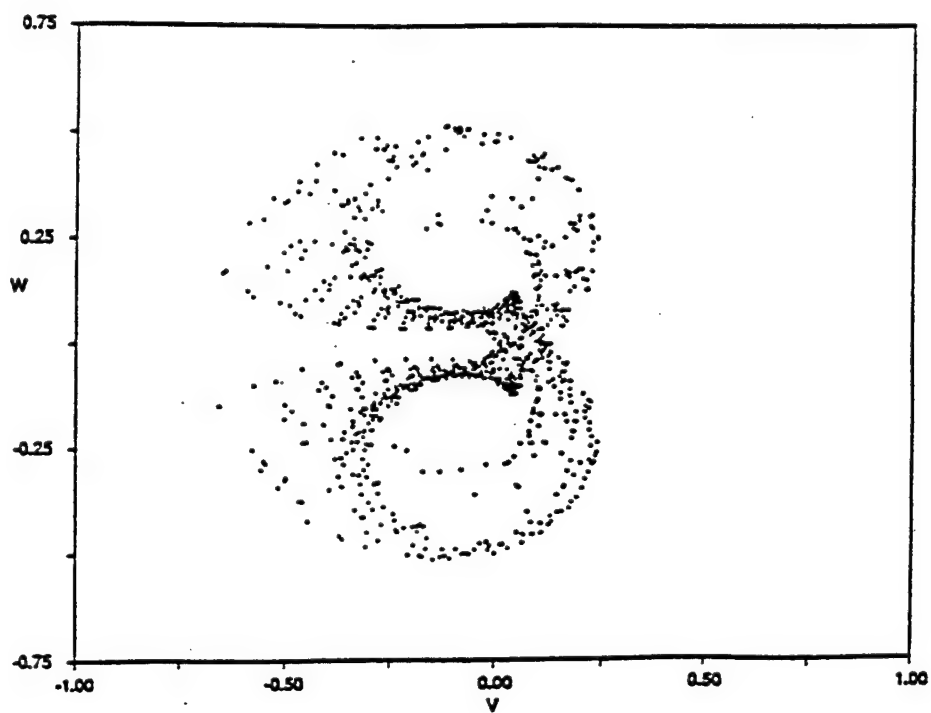Figure 5.9: Power spectrum of in-plane velocity shown in 5.8.

58
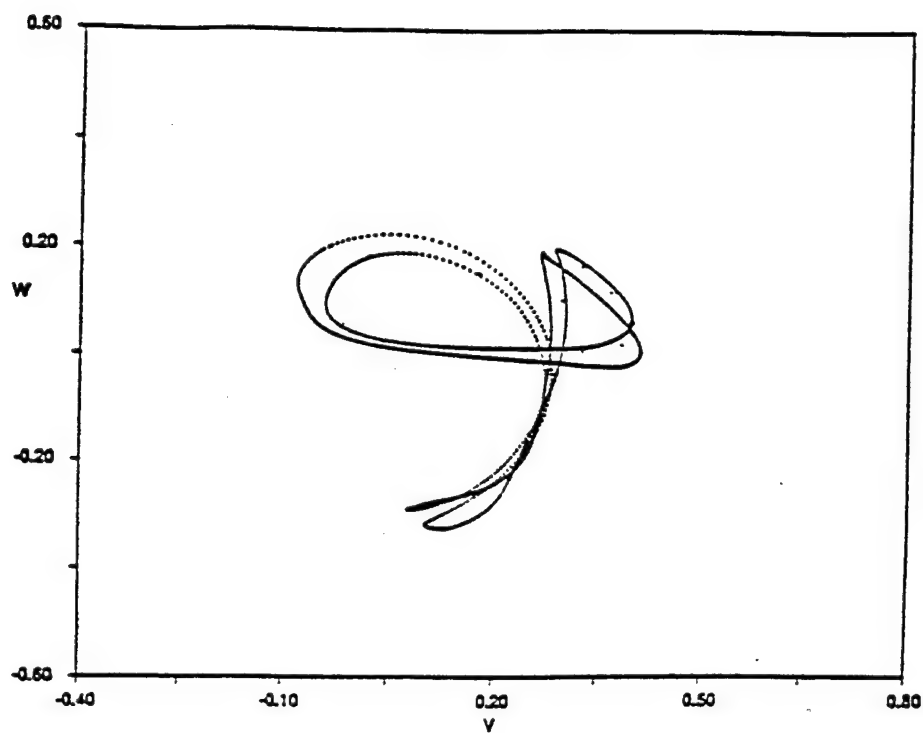
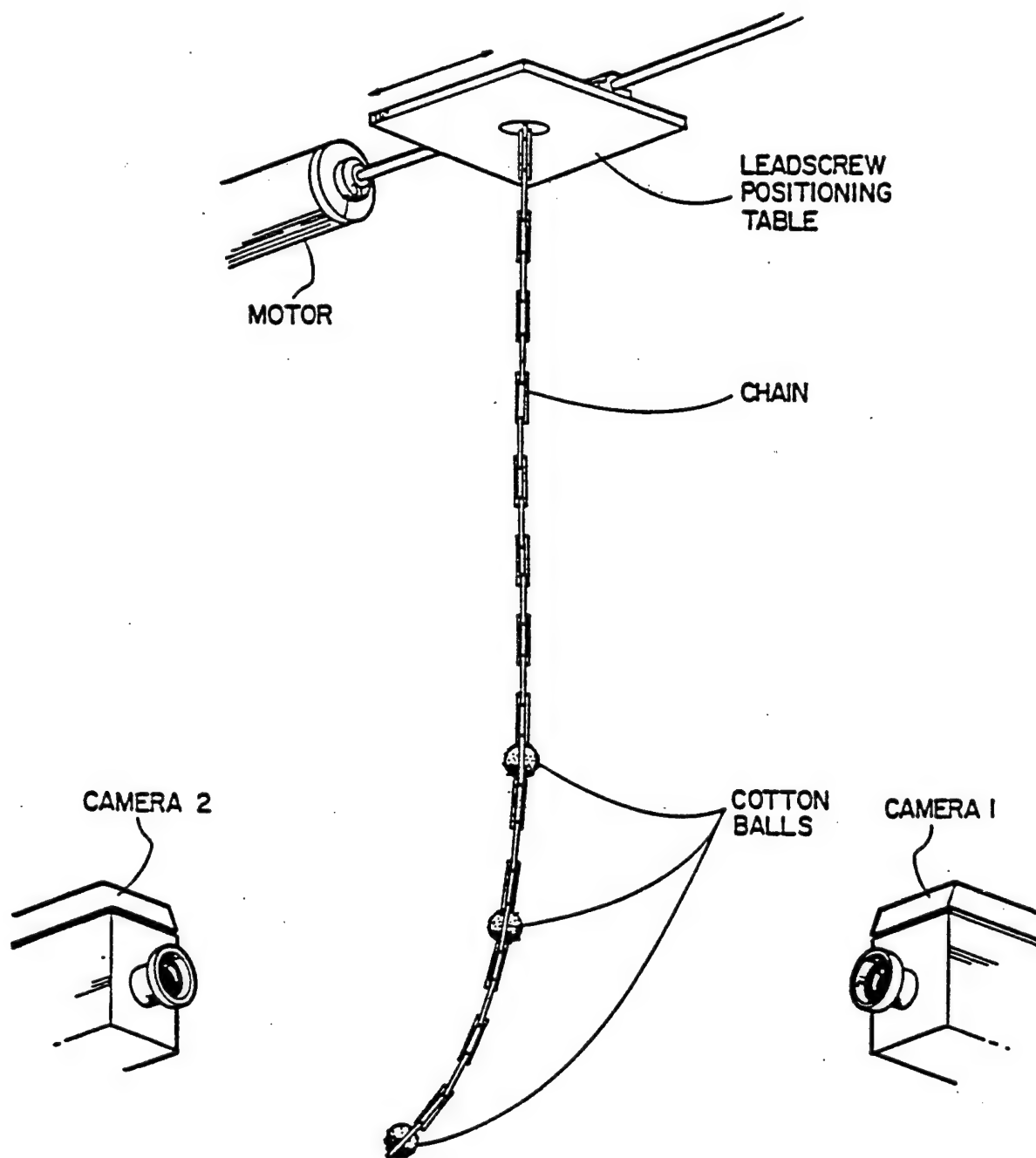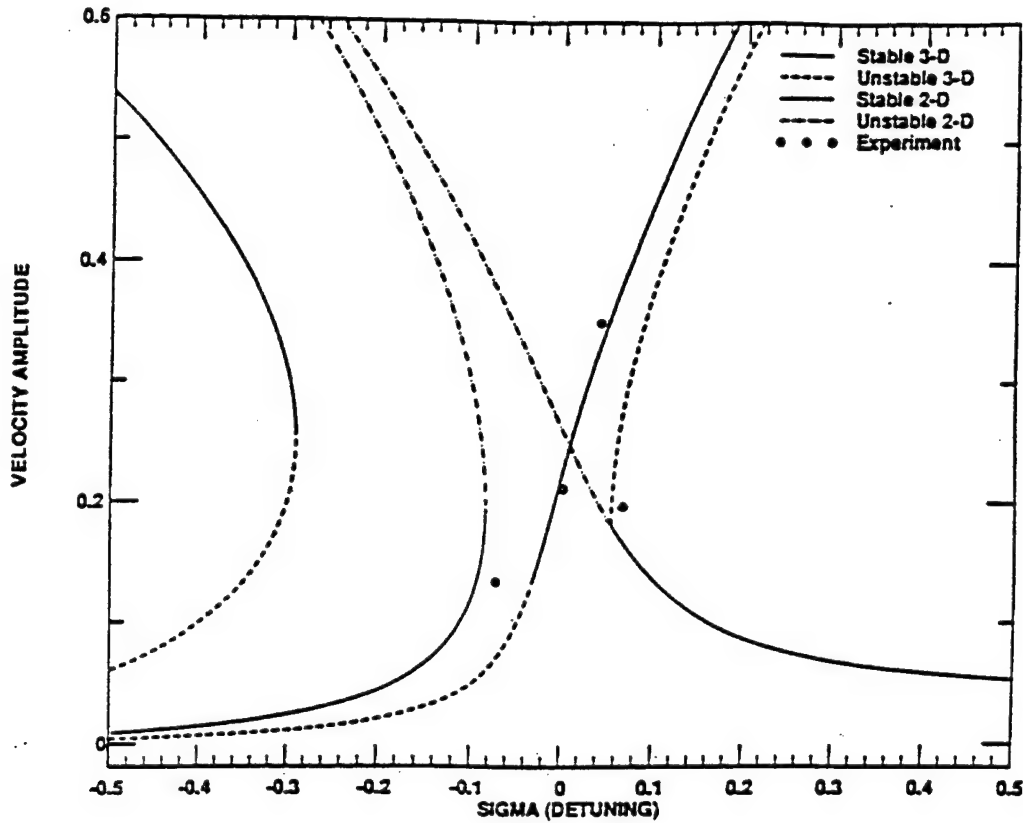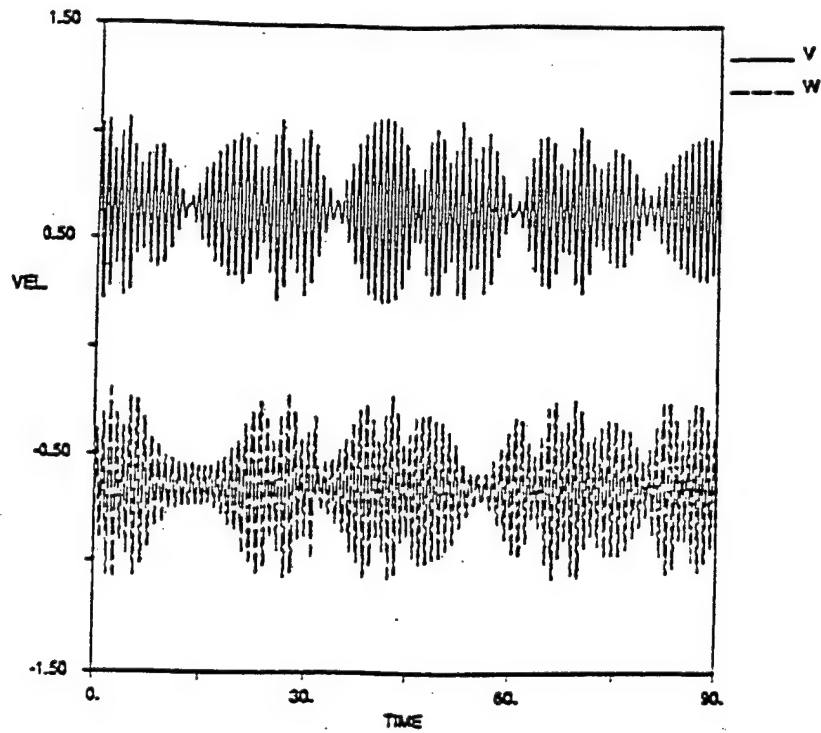Figure 5.10: Poincare plot of in-plane velocity shown in 5.8.
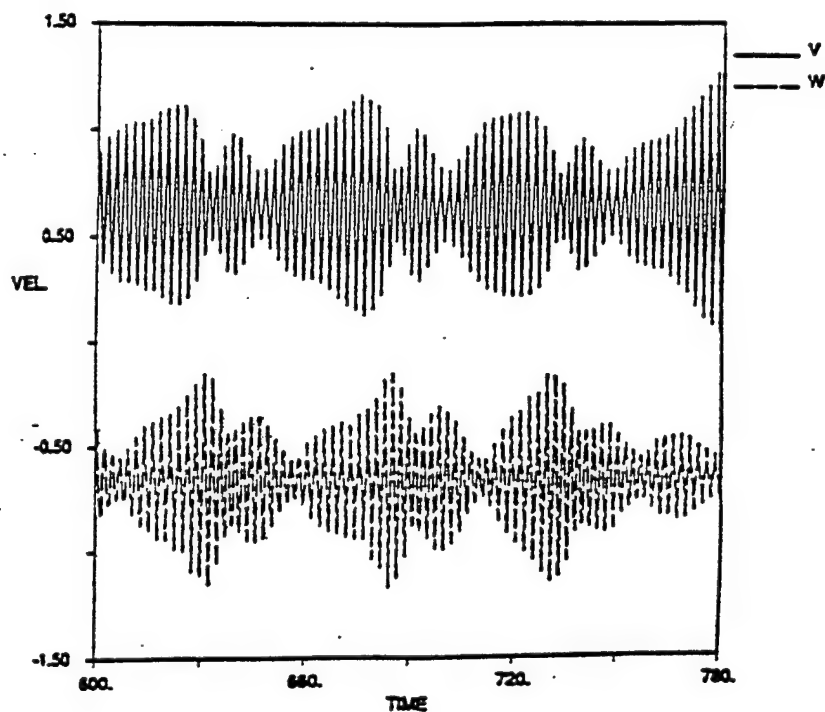
Figure 5.11: Numerical results: Time series record for in-plane and out-of-plane velocities at free end, with excitation amplitude $Y_o = 0.0087L$ and detuning $\sigma = -0.05$
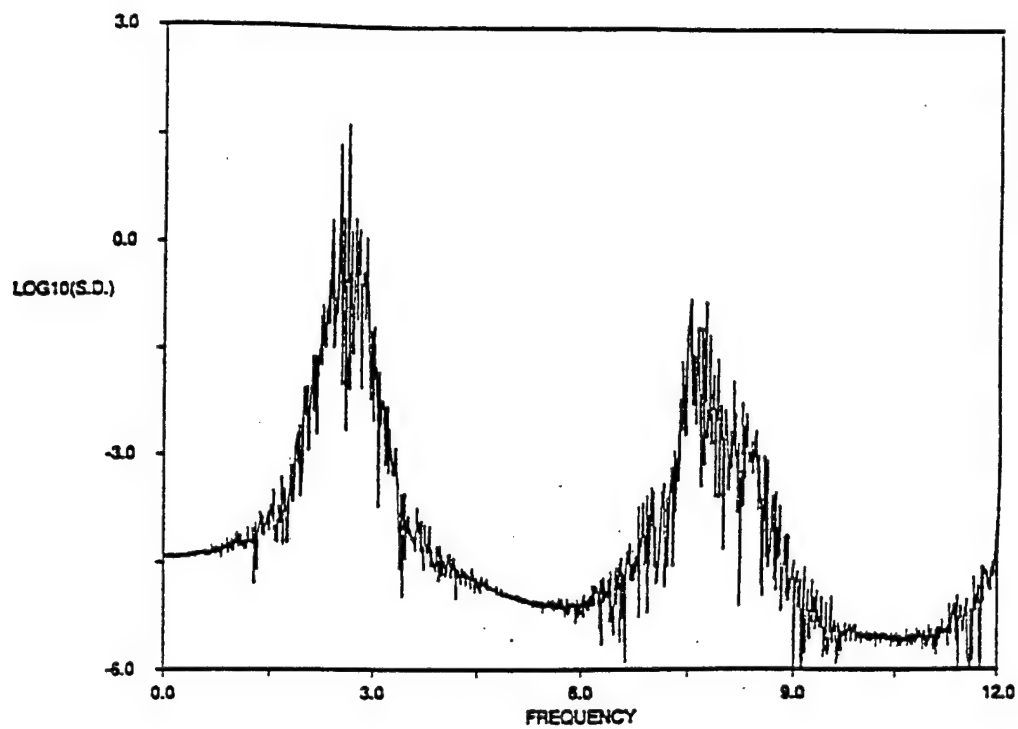
Figure 5.12: Power spectrum of in-plane velocity shown in 5.11.

Figure 5.13: Poincare plot of in-plane velocity shown in 5.11.

Figure 5.14: Experimental setup.

Figure 5.15: Experimental results (circles) compared with perturbation results (lines): In-plane velocity at lower end for excitation amplitude $Y_o = 0.0087L$.

spectra obtained at other excitation frequencies.

5.6 Response to Large Amplitude Excitation

We investigate the response of the chain to excitation amplitudes in excess of those studied previously. Much of the work detailed here is summarized in a paper by Howell (1992).

As discussed earlier the asymptotic analysis results predict that increased excitation amplitude widens the frequency region in which all steady state solutions are determined to be unstable. Therefore it is logical to investigate unsteady solutions for larger excitation amplitudes. However, the numerical scheme was found to encounter stability problems when bending stiffness was neglected. In addition, solutions within the unstable frequency range were found to be unobtainable numerically when damping was removed. To understand why this occurs, we further investigate the perturbation results to determine if it is possible for the dynamic tension to cancel the static tension, thereby causing the chain to lose tension over a portion of its length. Here we simplify the analysis by concentrating on the region near the lower boundary because that is the location where it is most likely that tension will be lost.

Using the previously obtained results we find that

$$\lim_{s \to 0} \frac{T_2(s,t) + mgs}{mgs} = \frac{a^2[1 \pm (3 - 4J_1(z_o)^2)] + 4}{4}.$$

62

Figure 5.16: Experimental results: Time series record for in-plane and out-of-plane velocities at free end, with excitation amplitude $Y_o = 0.0087L$ and detuning $\sigma = -0.028$
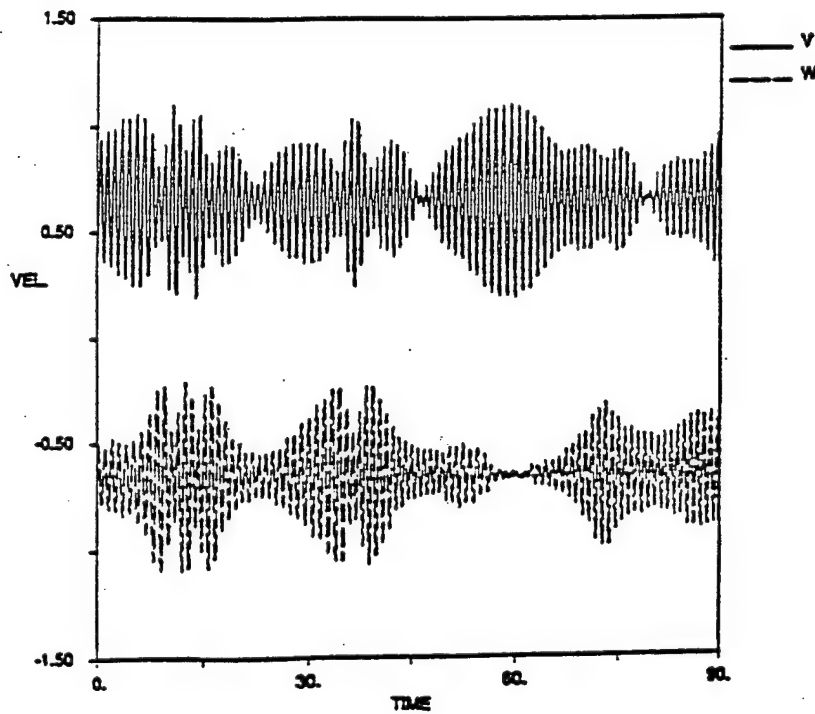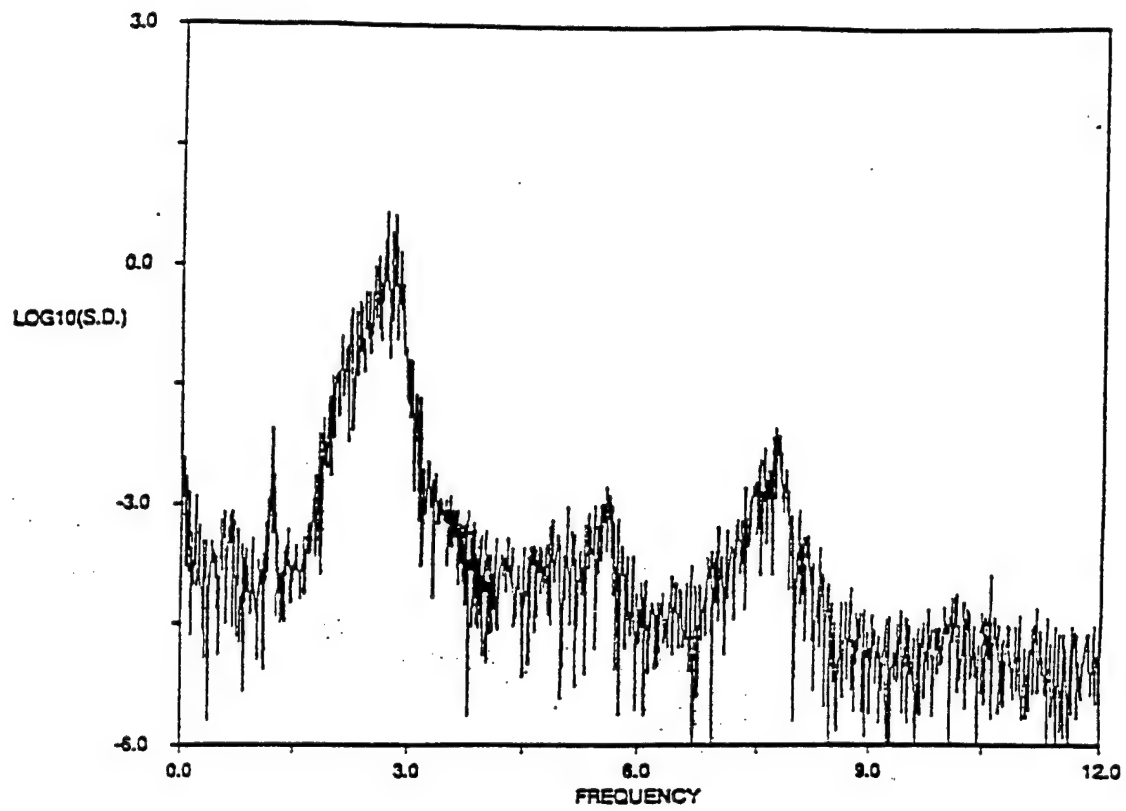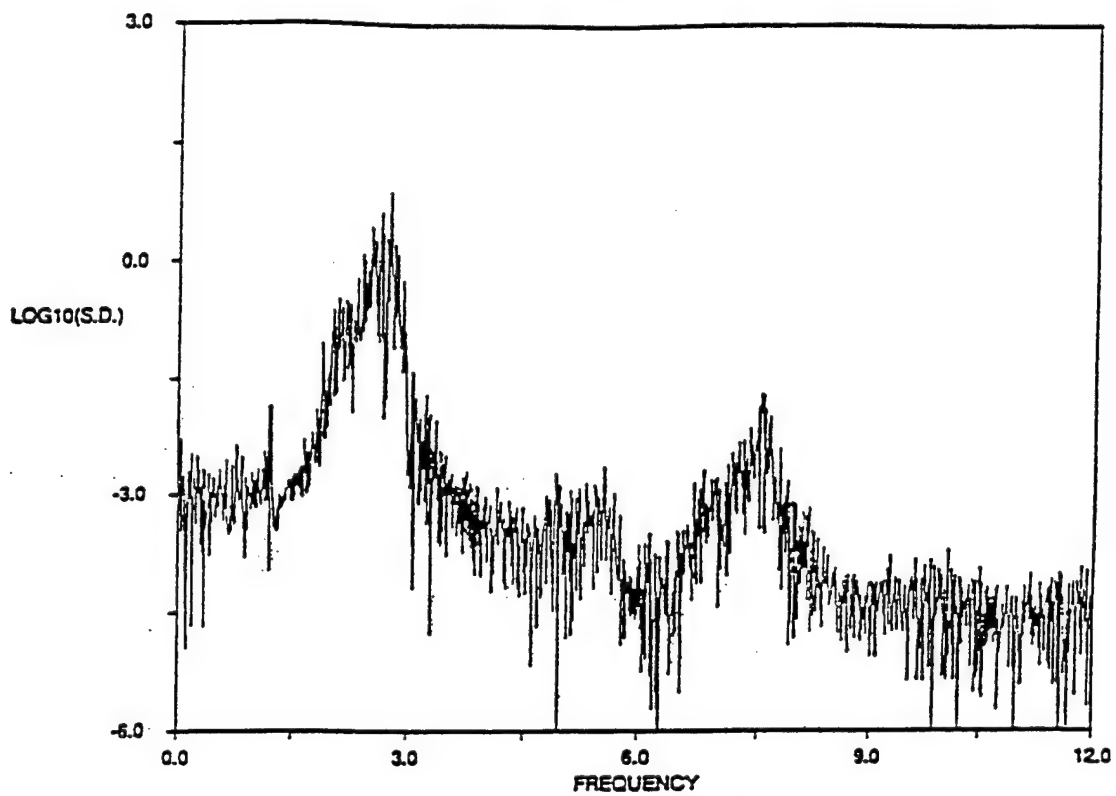

Figure 5.17: Experimental results: Time series record for in-plane and out-of-plane velocities at free end, with excitation amplitude $Y_o = 0.0087L$ and detuning $\sigma = -0.047$

63

Figure 5.18: Power spectrum of in-plane velocity shown in 5.16.

Figure 5.19: Power spectrum of in-plane velocity shown in 5.17.

Therefore, if we express the condition for negative tension values to occur in terms of the angle at the free-end we find

$$a > \sqrt{\frac{2}{1 - 2J_1(z_o)^2}} \qquad (5.24)$$

In terms of solutions near the second natural frequency, this means the angle must exceed 1.61 radians for the tension to become negative. This corresponds to the free-end of the cable slightly exceeding a horizontal orientation.

This analysis shows that, according to the perturbation technique, above a certain level of response amplitude, and near resonance, negative tension occurs near the free end. Since negative tensions cannot be sustained, the chain loses tension over a portion of its length. This leads to increased angles, eventually resulting in the chain collapsing.

Numerical and experimental tests were conducted at larger excitation amplitudes aimed at verifying the numerical model so that it could be used as a tool for studying the dynamics leading to the collapse of the chain. Results are presented herein for an excitation amplitude of $0.017L$ and a frequency of 1.5 hertz, corresponding to a detuning of 0.44. The excitation amplitude was ramped linearly in time over 2.0 seconds. This short ramping interval was chosen to simplify the analysis by not allowing sufficient time for exciting dynamics out-of-plane. A number of ramping intervals were investigated and quantitatively similar results were obtained in each case. Therefore, the ramping interval selected is not of importance.

Numerical studies were first conducted neglecting bending stiffness. Numerical results for the chain shape at several different time steps, prior to the loss of tension, are shown in figure 5.20. The lower one-fifth of the chain has been enlarged to show that only a small segment of the chain loses tension. After tension is lost, the numerical scheme becomes unstable and fails to converge.

As discussed previously, the cable equations are singular for zero tension if bending stiffness is neglected. There is an additional singularity, however, when the tension becomes zero which appears in the compatibility relations.

The compatibility relations derived in §2 are based on spatial and temporal continuity of the position vector $\vec{r}(t, s)$.

Once tension is lost, however, there is no physical mechanism that enforces slope continuity in the line. It is possible for a perfectly flexible cable to form corners in its configuration. As a result the compatibility relations in differential form, as derived in §2, are invalid once tension is lost and a new set of compatibility relations must be devised to preserve the chain length. One could also model the chain as a series of rigid links, however, this would require an inordinate number of degrees of freedom thereby significantly reducing the computational efficiency.

Both problems, i.e. the singularity in the equations of motion and the discontinuities in slope, are eliminated by incorporating bending stiffness. Bending stiffness smooths out discontinuities, as addressed in §4, and provides a physical mechanism for energy propagation in the absence of tension. For cables bending stiffness is the actual physical mechanism that must be included for accurate modeling. For chains the link interaction is far more complex to model, so we treat the chain as a highly flexible cable by adopting a small value of bending stiffness as a mathematical fix of the singularities encountered. The numerical procedure for incorporating bending stiffness presented in §3 was adopted for this analysis.

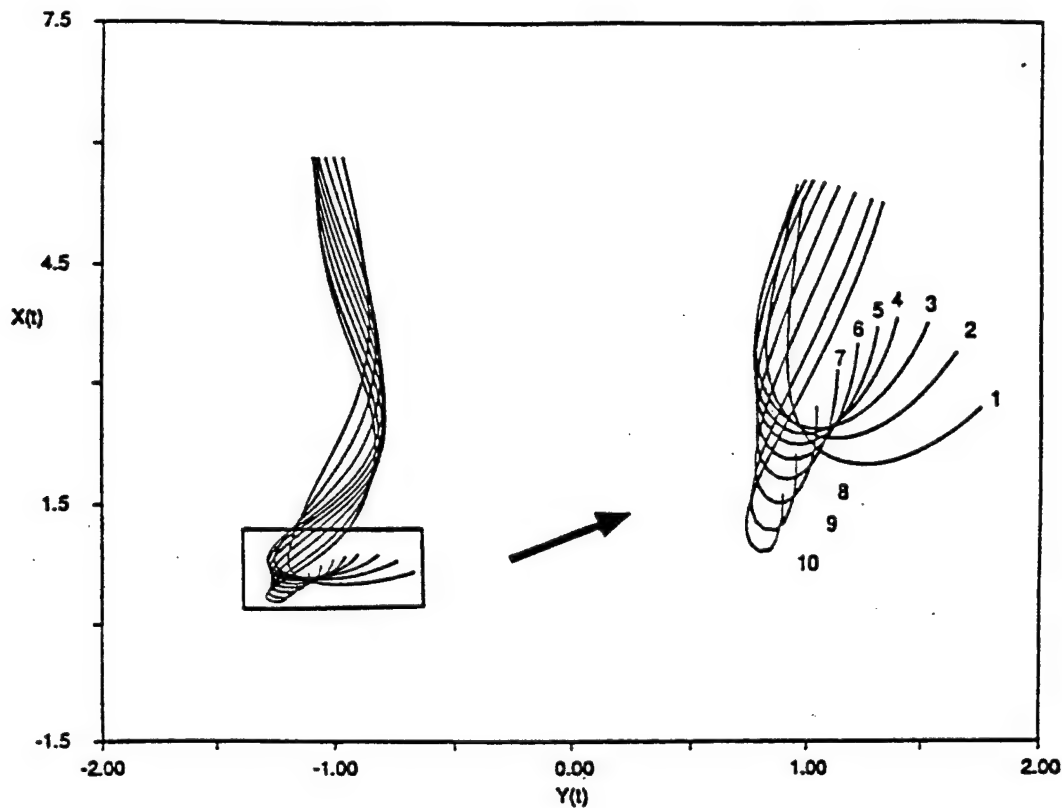Numerical results after the chain has lost tension and collapsed were obtained using

Figure 5.20: Numerical results: Chain configuration at several times prior to the collapse of the lower region. Segment in box enlarged on the right.

a nondimensional bending stiffness value of $EI/mgL^3 = EI^* = 10^{-6}$. Computations proceeded through the onset of zero tension, eventually determining one-half cycle later that, after tension has been restored, the chain intersects itself as shown in figure 5.21.

To demonstrate that incorporating bending a small degree of bending stiffness eliminates the zero tension singularities, while not significantly altering the solution, figure 5.22 shows numerical results for two values of EI^*. As shown, similar results are obtained for an order of magnitude variation in flexural stiffness. Note that this is attributable to the magnitude of the bending stiffness incorporated.

Figures 5.23 through 5.26 show the numerically obtained time series records for the tension, tangential velocity, normal velocity, and angle, at four locations along the chain. Figure 5.23 clearly depicts the transition from low to high tension. Near the lower boundary, impulse-like tension peaks are exhibited, followed by periods in which the tension is nearly zero. These tension peaks result in rapid variations in velocity, as shown in figures 5.24 and 5.25. Further up the chain, the response remains regular and behaves like the response of a taut cable. In contrast, at the lower end the angle increases beyond the value of π, at which time an entire segment of the chain loses tension and collapses (figure 5.26).

The normal velocity along the chain is shown in figure 5.27 for four different times. As shown an energy wave is generated at the top which amplifies as it travels toward the free end. Steep gradients in velocity develop which in turn give rise to large angular accelerations. Eventually the angular momentum builds to where the tension is canceled and the angle increases beyond π.
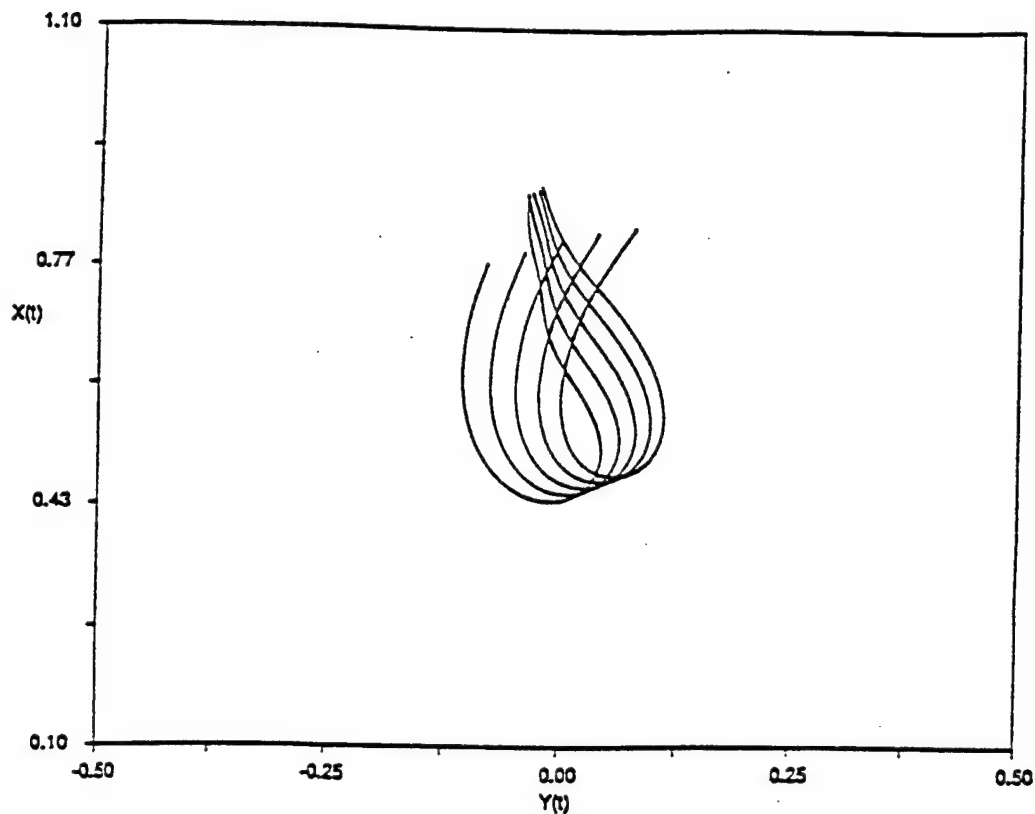
66

Figure 5.21: Numerical results: Predicted chain configuration as free-end intersects the chain.

The dynamic tension along the chain, obtained by removing the static tension from the total tension, is shown in figure 5.28 for the listed times. Figure 5.28 clearly demonstrates that low tension effects are confined to a region encompassing less than 10 percent of the total chain length, while the remaining chain exhibits a taut cable response.

Figures 5.29 and 5.30 compare experimental and numerical results for the chain displacement at three different times. The lower half of the chain is isolated in figure 5.29, while the lower one-eighth is shown in figure 5.30. Note that the numerical results were obtained using the small value of bending stiffness discussed previously. As readily seen the numerical technique accurately predicts the displacement up to the point where tension was lost and good agreement was found at the point where the chain intersects itself (t=3.8 s, figure 5.30).

Figure 5.31 depicts the experimental results for the chain intersection with itself. This intersection was found to occur at the same time predicted numerically. It should be noted that the experimental tests did remain two-dimensional as demonstrated by the free-end colliding with the chain.

67
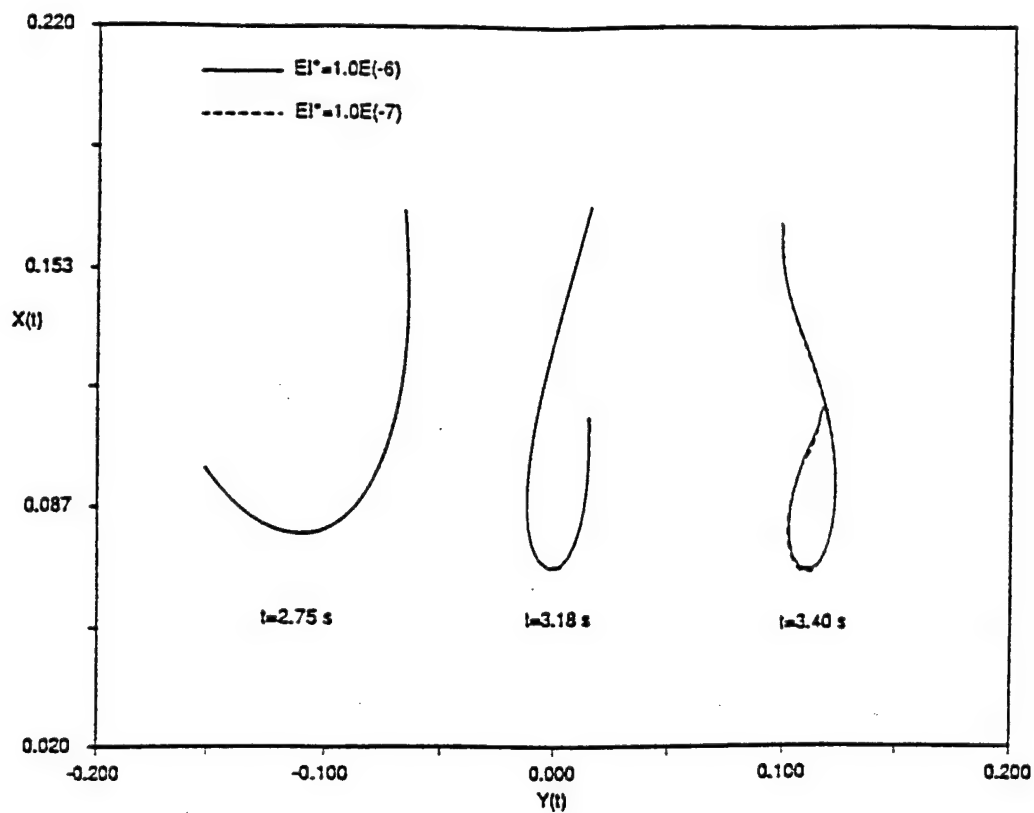
Figure 5.22: Comparison of simulation results for two values of EI^*.
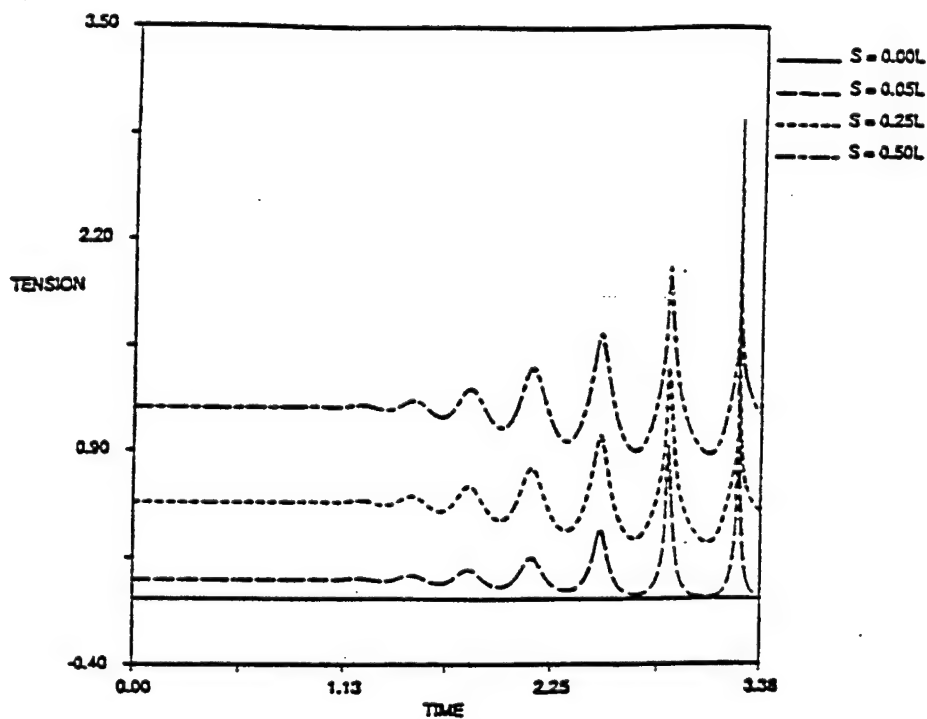

Figure 5.23: Numerical results: Total tension at four locations along the chain, for case under study.
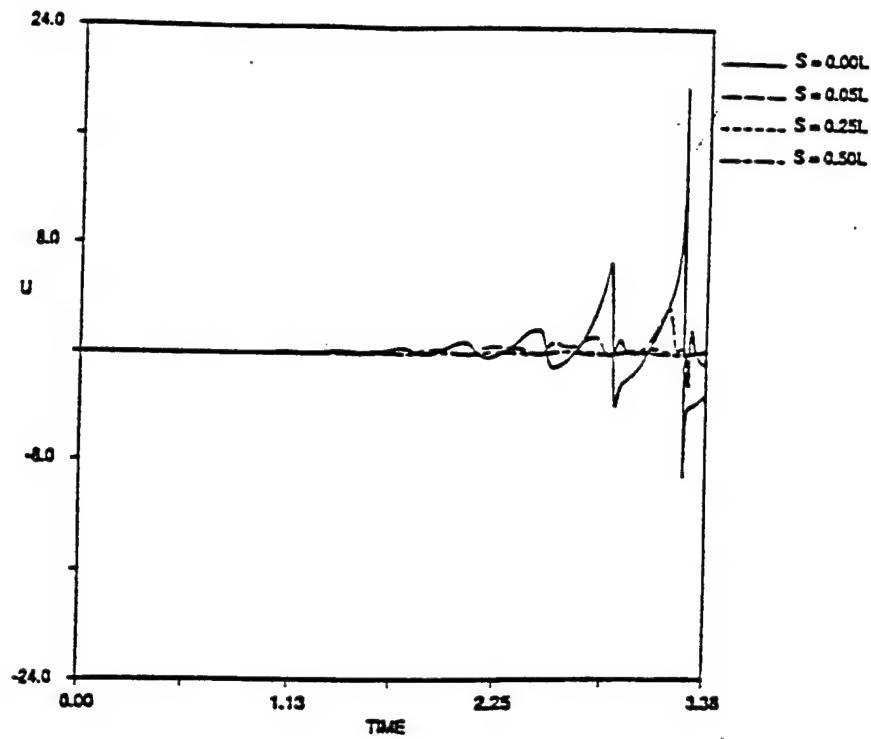
Figure 5.24: Numerical results: Tangential velocity at four locations along the chain, for case under study.
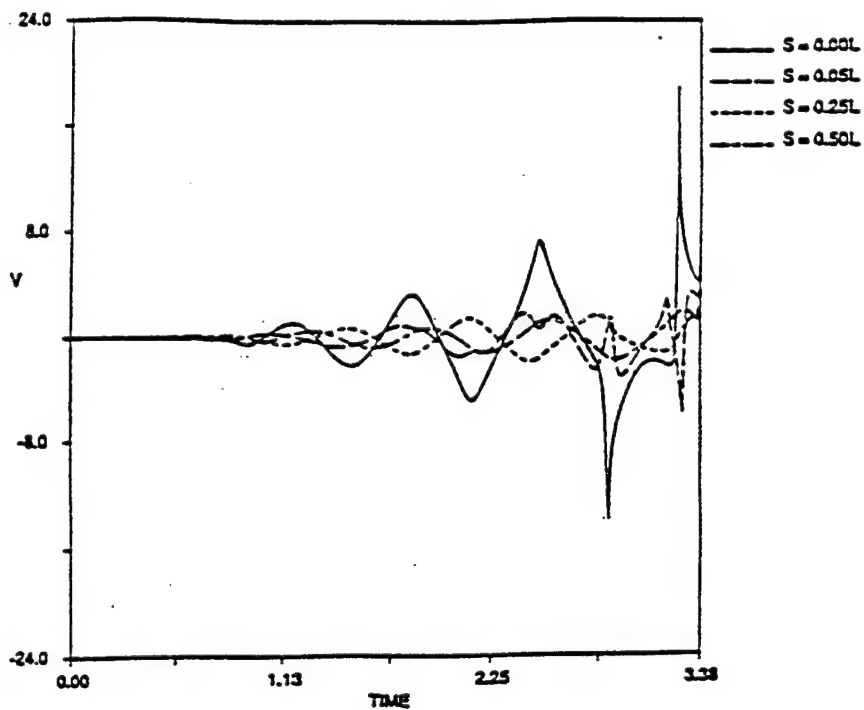

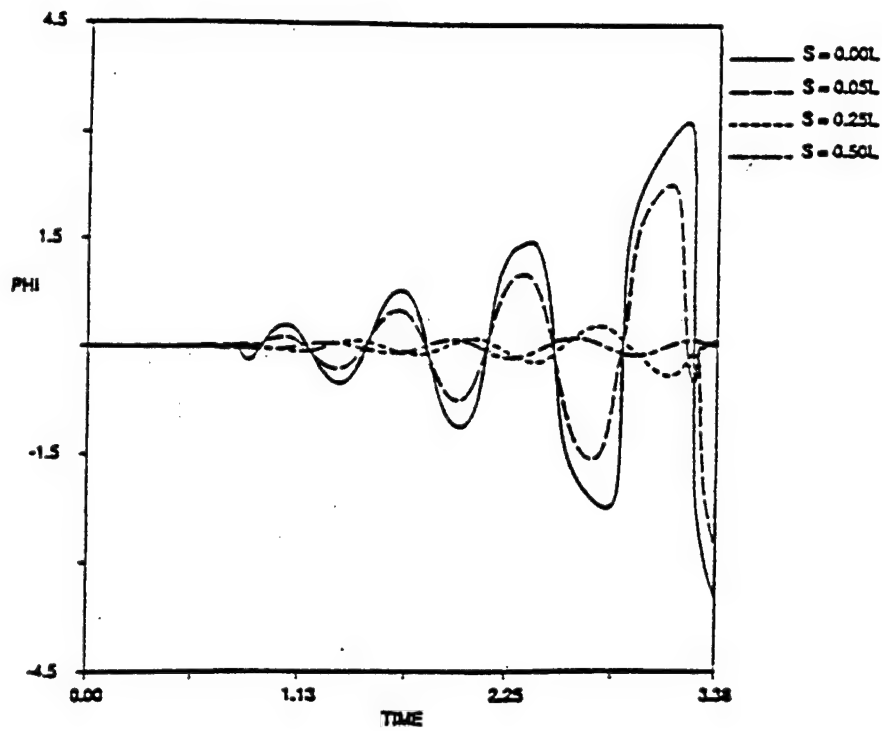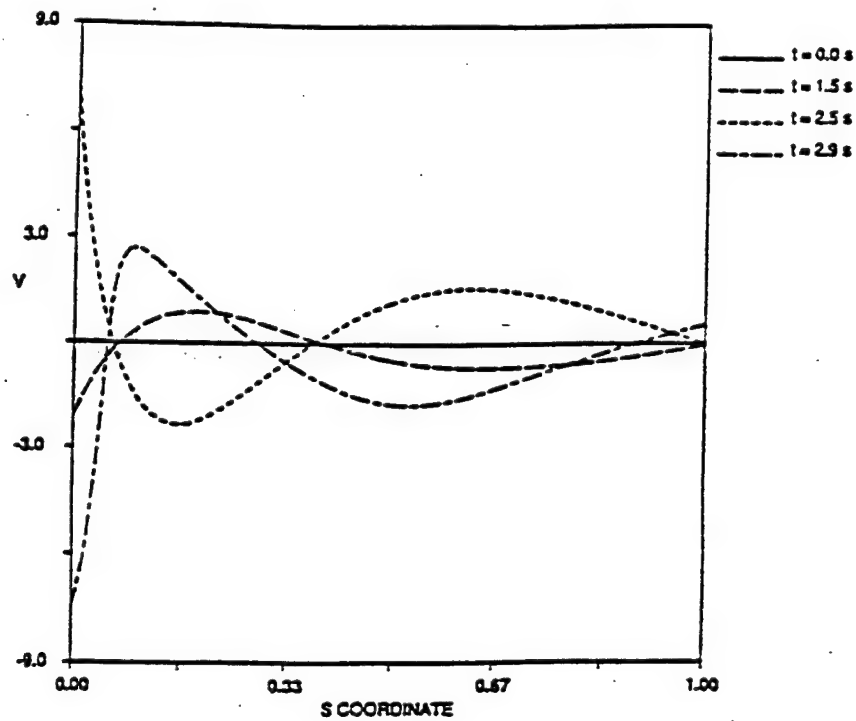Figure 5.25: Numerical results: Normal velocity at four locations along the chain, for case under study.

Figure 5.26: Numerical results: Angle (radians) at four locations along the chain, for case under study.

Figure 5.27: Numerical results: Normal velocity along chain at four different times, for case under study.
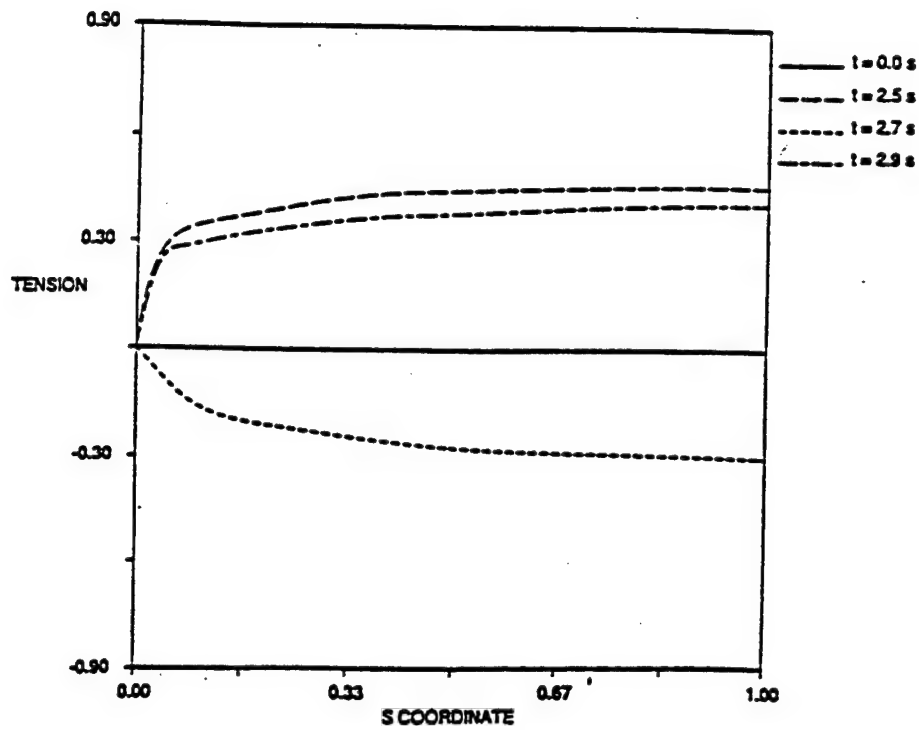
Figure 5.28: Numerical results: Dynamic tension along chain at four different times, for case under study.
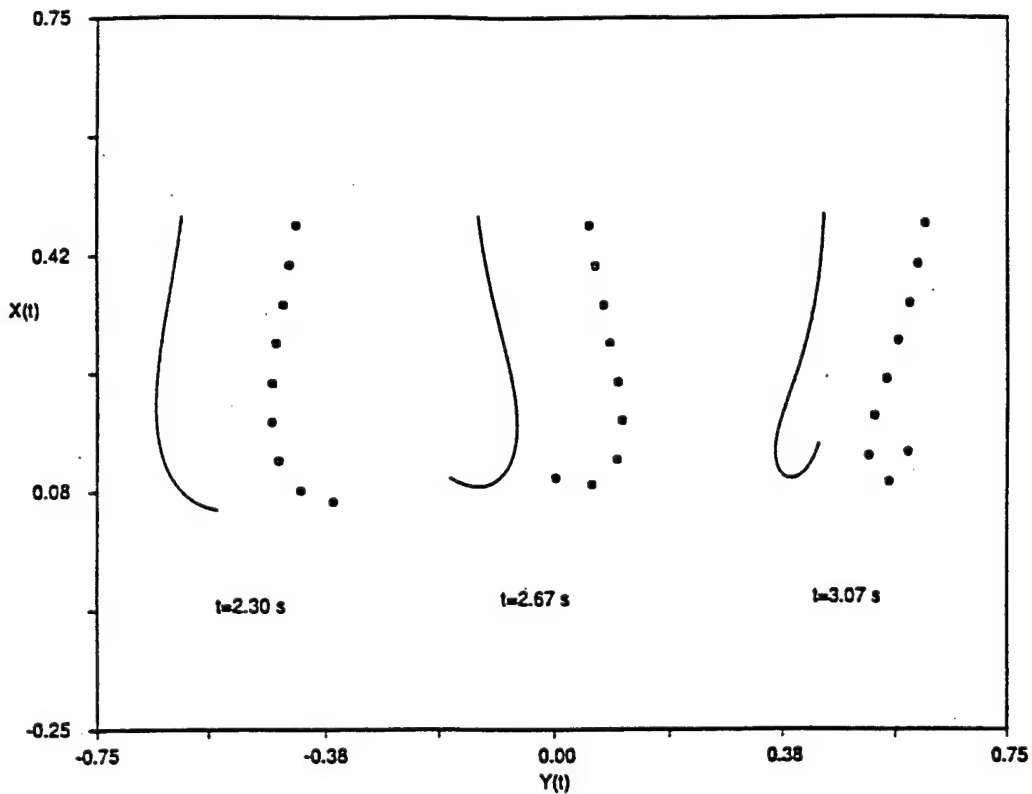

Figure 5.29: Comparison of experimental and numerical results for collapsing chain: lower half of chain.
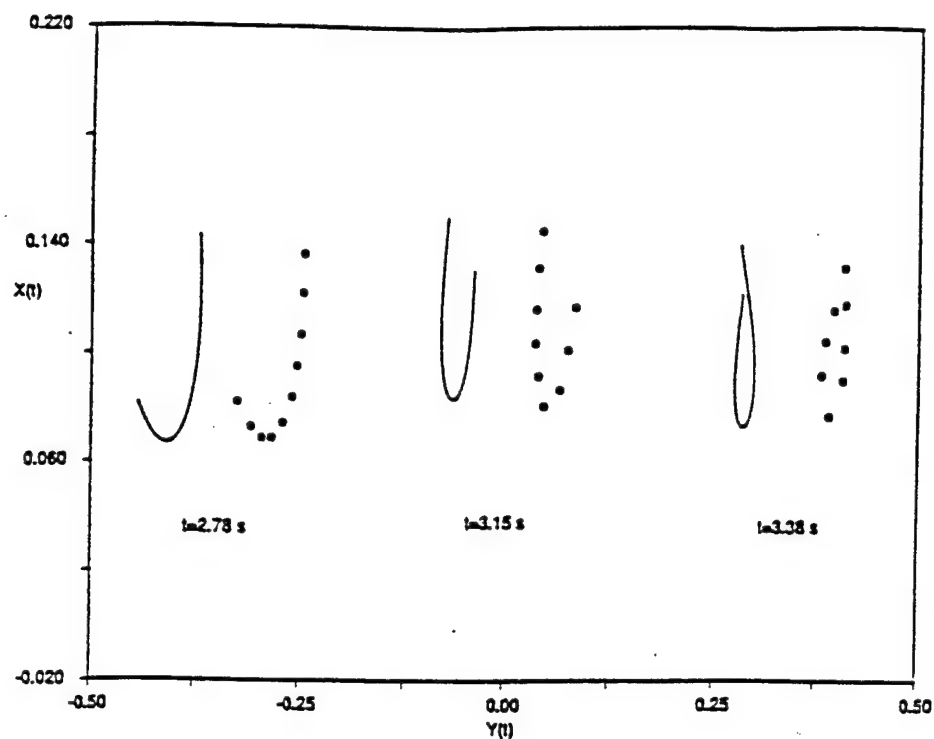
71

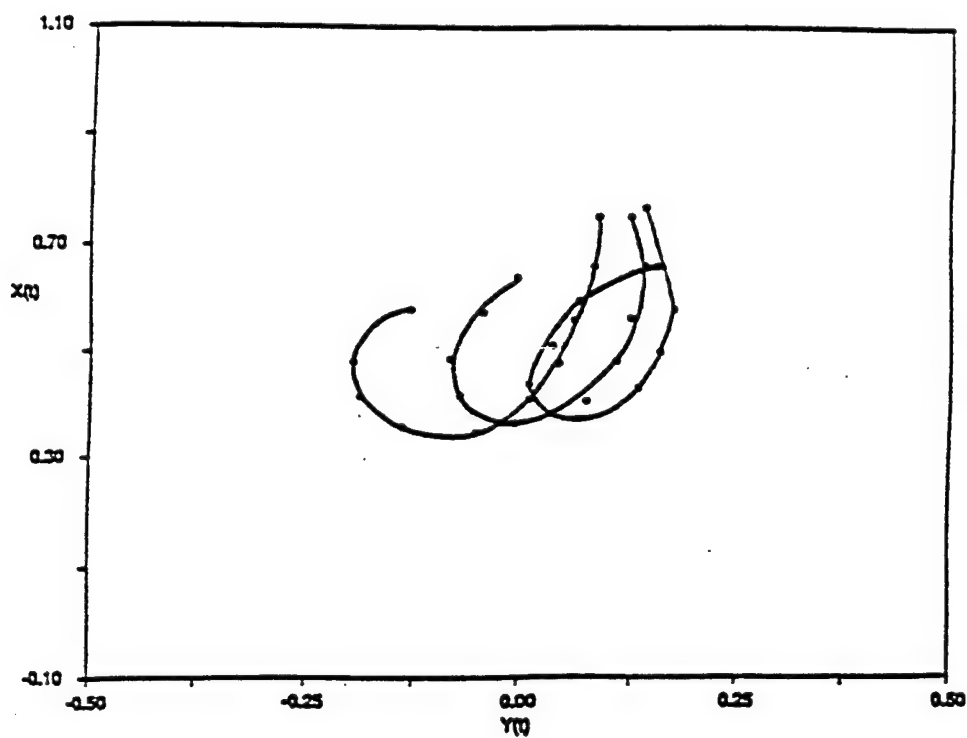Figure 5.30: Comparison of experimental and numerical results for collapsing chain: lower one-eighth of chain.

Figure 5.31: Experimental results: Chain configuration at several times prior to the collapse of the lower region.

72

VI. ANALYSIS OF ELASTIC CABLE BEHAVIOR

6.1 Introduction

Up to this point, we have considered the dynamics of cables with infinite elastic stiffness. In this chapter we relax this restriction and incorporate elasticity in the equations of motion.

The effects of elasticity can be separated into two categories; quasi-static stretching and elastic or longitudinal waves. The significance of quasi-static stretching has been the subject of extensive research in the past (Irvine and Caughey, 1974; Shin, 1987; Triantafyllou, 1984) and will be addressed in §6.2. Insight into the importance of elastic waves can be gained by considering the relative magnitudes of transverse and elastic wave speeds. Bliek (1984), using the method of characteristics, derived expressions for the transverse and elastic wave speeds C_{tr} and C_{el}, respectively, for an elastic cable. Assuming a linear stress-strain relation, the expressions are given by

$$C_{tr} = \pm \left[\frac{T}{(m+m_a)(1+e)} \right]^{1/2} \tag{6.1}$$

$$C_{el} = \pm \left[\frac{EA}{m} \right]^{1/2} \tag{6.2}$$

Therefore, the ratio of wave speeds is roughly given by

$$\frac{C_{el}}{C_{tr}} \simeq \left[\frac{EA}{T} \right]^{1/2} \tag{6.3}$$

For low tension values this ratio is very large, therefore, the fundamental frequency of elastic waves corresponds to a very high-order transverse mode. If the cable tension is large, it must still remain below an upper bound given by the breaking stress. For metallic cables, the upper bound is given by

$$\frac{T}{A} = \mu < \mu_b \ll E \tag{6.4}$$

where μ and μ_b denote the axial and breaking stress, respectively. Therefore, for metallic cables, the ratio of wave speeds remains high regardless of the cable tension (Triantafyllou, 1986).

For the reasons discussed above, if the excitation frequency is narrow-banded and corresponds to a low-order transverse mode, it can be assumed that elastic vibrations will not be excited. However, if the excitation frequency is broad-banded, sufficient energy may exist at high frequency to excite elastic waves.

The results derived in §5.6 (figure ??) demonstrate that the response of the hanging chain to large amplitude excitation is characterized by impulse-like tension peaks. The energy content of these tension peaks is broad-banded, which brings into question the validity of neglecting elasticity in this case.

To resolve this question, a linear stress-strain model was incorporated into the implicit finite-difference algorithm discussed in §3. An implicit time domain routine is necessary as the high propagation speed of elastic waves would require prohibitively small time-step

73

increments in an explicit algorithm (Sanders, 1982). To validate the model, we consider the linear dynamics of an elastic catenary.

It should be reiterated that a major reason for the increase in low-tension systems is the frequent use of synthetic cables. Aside from the decrease in density, the modulus of elasticity E of synthetic cables is appreciably less than that of metallic cables. As a result, synthetic cables have reduced axial and flexural stiffness than metallic cables of equivalent size. The reduction in flexural stiffness simplifies storage and handling of the cable. This in fact is one of the major benefits of synthetic cables. The low axial stiffness, however, can result in substantial stretching and thus a large buildup of potential energy. This makes synthetic cables extremely dangerous in failure. For this reason, and the fact that the dynamics of highly extensible cables are not fully understood, large safety factors are used in design and the diameters selected are often much greater than necessary, thereby reducing their benefits to some degree.

6.2 Elastic Motions of Shallow Sag Cables

The elastic dynamics of suspended cables undergoing quasi-static stretching, i.e. no elastic waves are excited, has received considerable attention. Much of the research was aimed at resolving a discrepancy between taut-string results and inelastic horizontal catenary solutions in the limit that the cable sag to span ratio approaches zero. A clear explanation of the phenomena involved was presented by Irvine and Caughey (1974). Their results demonstrate that the significance of elastic effects is governed by the ratio of elastic to catenary stiffness, denoted as λ^2. Also shown was that for shallow sag cables, the fundamental natural frequency of symmetric modes crosses the fundamental frequency of antisymmetric modes at a critical value of λ^2, the so-called mode cross-over phenomena. Triantafyllou and Grinfogel (1986) show that the dynamics of inclined cables are distinctly different than those of horizontal cables in that frequency cross-overs do not occur and that large dynamic tension amplification occurs in the region of avoided crossings. Their results are based on more general asymptotic solutions, also derived by Triantafyllou (1984), in which elastic waves are retained.

For completeness, we derive the linear solutions presented by Irvine and Caughey (1974) in terms of body-fixed coordinates. These results are then used to verify the accuracy of the numerical algorithm.

6.2.1 DERIVATION OF LINEAR EQUATIONS

We consider the dynamics of a perfectly flexible cable supported by two frictionless end supports at the same level, as shown in figure 6.1. The cable is assumed to have a small sag to span ratio, i.e. $\delta/S < 1/8$ where δ and S denote the cable sag and span respectively. Irvine and Caughey (1974) have shown that within the linear regime, i.e. small motions, the out-of-plane dynamics decouple from in-plane dynamics. This is because, to first-order, out-of-plane motions involve not additional cable tension. In addition, Rega et al. (1984) demonstrated that for nonlinear motions, planar oscillations are stable, with the exception of the case where the in-plane linear frequency is twice the out-of-plane natural frequency. As such, we restrict our attention to two-dimensional dynamics. The two-dimensional governing equations and compatibility relations for an elastic cable, as derived in §2, are given by
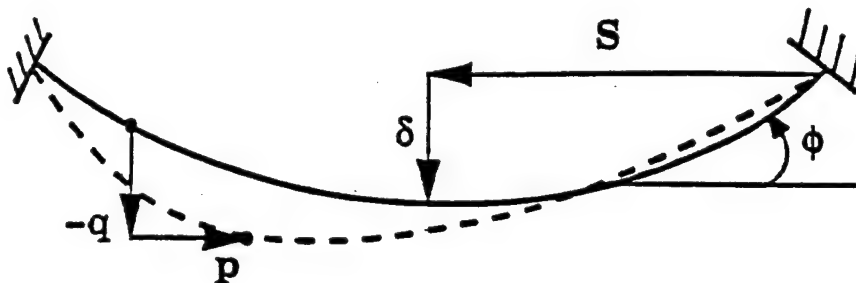
74

Figure 6.1: Cable suspended between two endpoints.

$$
\begin{aligned}
m\left(\frac{\partial u}{\partial t} - v\frac{\partial \phi}{\partial t}\right) &= \frac{\partial T}{\partial s} - w_o \sin \phi \\
m\left(\frac{\partial v}{\partial t} + u\frac{\partial \phi}{\partial t}\right) &= T\frac{\partial \phi}{\partial s} - w_o \cos \phi \\
\frac{\partial u}{\partial s} - v\frac{\partial \phi}{\partial s} &= \frac{\partial e}{\partial t} \\
\frac{\partial v}{\partial s} + u\frac{\partial \phi}{\partial s} &= \frac{\partial \phi}{\partial t}(1 + e) \\
T &= EAe.
\end{aligned}
\tag{6.5}
$$

Here we have adopted the same nomenclature defined in §2, with the exception that the angle ϕ is measured with respect to the horizontal, rather than the vertical, as shown in figure 6.1.

We seek to study the linear dynamics of the cable by considering small motions from the static configuration. Toward this end, we decompose the variables into static and dynamic terms as follows:

$$
\begin{aligned}
T &= T_0 + T_1 \\
\phi &= \phi_0 + \phi_1 \\
e &= e_0 + e_1
\end{aligned}
\tag{6.6}
$$

where the subscripts 0 and 1 denote static and dynamic quantities, respectively, and all dynamic quantities are assumed to be of order $O(\epsilon)$, where $\epsilon \ll 1$.

Eliminating all dynamic quantities from (6.5) yields the equations of static equilibrium.

$$\frac{\partial T_0}{\partial s} = w_o \sin \phi_0 \tag{6.7}$$

$$T_0 \frac{\partial \phi_0}{\partial s} = w_o \cos \phi_0$$

$$T_0 = EAe_0.$$

The solution of (6.7) gives the shape of the catenary. These equations can be written in a more convenient form as follows:

$$T_0 = \frac{H}{\cos \phi_0} \tag{6.8}$$

$$\frac{\partial \phi_0}{\partial s} = \frac{\alpha}{L} \cos^2(\phi_0)$$

where H is the horizontal component of the static tension and α is given by

$$\alpha = \frac{w_o L}{H}. \tag{6.9}$$

For cables with small sag to span ratios, the slope of the cable is everywhere small. Therefore, $\cos(\phi_0) \simeq 1$ and the static solution can be expressed as

$$T_0 \simeq H \tag{6.10}$$

$$\sin \phi_0 \simeq \phi_0 \simeq \frac{\alpha}{L}s.$$

For small motions we can approximate the velocities in terms of small displacements from the static configuration, as follows:

$$u \simeq \frac{\partial p}{\partial t} \tag{6.11}$$

$$v \simeq \frac{\partial q}{\partial t}$$

where p and q are the tangential and normal displacements from the static configuration, respectively.

Substitution of (6.6), (6.10), and (6.11) into (6.5), removing the static solution, and retaining only first-order quantities yields

$$m\frac{\partial^2 p}{\partial t^2} = \frac{\partial T_1}{\partial s} - \phi_1 \frac{\alpha H}{L} \tag{6.12}$$

$$m\frac{\partial^2 q}{\partial t^2} = T_1 \frac{\alpha}{L} + H\frac{\partial \phi_1}{\partial s}$$

$$\frac{\partial p}{\partial s} - q\frac{\alpha}{L} = \frac{T_1}{EA}$$

$$\frac{\partial q}{\partial s} + p\frac{\alpha}{L} = \phi_1.$$

Note that we have removed the time derivatives from the compatibility relations by integrating the two equations in time. For small displacements, longitudinal motions are small compared to transverse motions. As such,

$$p\frac{\alpha}{L} \ll \frac{\partial q}{\partial s}, \phi_1 \tag{6.13}$$

76

therefore, we can neglect this term form the final equation in (6.12).

We eliminate the time dependence in (6.12) by considering harmonic motions, and express the variables as follows:

$$p_1 = \tilde{p}e^{i\omega t} \tag{6.14}$$
$$q_1 = \tilde{q}e^{i\omega t}$$
$$\phi_1 = \tilde{\phi}e^{i\omega t}$$
$$T_1 = \tilde{T}e^{i\omega t}$$

where ω is the natural frequency of vibration. Introducing (6.14) into (6.12) yields

$$
\begin{aligned}
-m\omega^2\tilde{p} &= \frac{\partial \tilde{T}}{\partial s} - \tilde{\phi}\frac{\alpha H}{L} \\
-m\omega^2\tilde{q} &= \tilde{T}\frac{\alpha}{L} + H\frac{\partial \tilde{\phi}}{\partial s} \\
\frac{\partial \tilde{p}}{\partial s} - \tilde{q}\frac{\alpha}{L} &= \frac{\tilde{T}}{EA} \\
\frac{\partial \tilde{q}}{\partial s} &= \tilde{\phi}.
\end{aligned}
\tag{6.15}
$$

Finally, we integrate the first equation in (6.15) with respect to space yielding

$$\tilde{T}(s) = h + \int_0^s (\tilde{\phi}\frac{\alpha H}{L} - m\omega^2\tilde{p})ds \tag{6.16}$$

where h is a constant. Assuming quasi-static stretching, no significant longitudinal dynamics are excited. The basis of this assumption is that for metallic cables, transverse wave speeds are, in general, much smaller than those of longitudinal waves (Bliek, 1984). Therefore, for low frequencies, longitudinal wavelengths are much greater than the overall cable length. However, for high excitation frequencies, longitudinal wavelengths may be less than L, and the quasi-static stretching assumption is no longer valid. This is an important consideration which must be taken into account in considering synthetic cables, which have a smaller Young's modulus than metallic cables, and therefore, smaller longitudinal wave speeds.

Introducing (6.16) into (6.15) and combining expressions yields

$$\frac{\partial^2 \tilde{q}}{\partial s^2} + \beta^2\tilde{q} = -\frac{h\alpha}{HL} \tag{6.17}$$

$$\frac{\partial \tilde{p}}{\partial s} - \tilde{q}\frac{\alpha}{L} = \frac{h}{EA} \tag{6.18}$$

where

$$\beta = \omega\sqrt{\frac{m}{H}}. \tag{6.19}$$

These equations are equivalent to the linear equations derived by Irvine and Caughey (1974) and can be combined to form a single equation in $\tilde{q}(s)$. Toward this end we integrate (6.18) along the cable and impose the boundary conditions $\tilde{p}(-L/2) = \tilde{p}(L/2) = 0$, which yields

$$h = -\frac{EA\alpha}{L^2}\int_{-L/2}^{L/2} \tilde{q}ds. \tag{6.20}$$

77

Substitution of (6.20) into (6.17) yields the linear equation for transverse motions.

$$\frac{\partial^2 \tilde{q}}{\partial s^2} + \beta^2 \tilde{q} = -\frac{\lambda^2}{L^3} \int_{-L/2}^{L/2} \tilde{q} ds \tag{6.21}$$

where

$$\lambda^2 = (\frac{EA}{H})(\frac{w_o L}{H})^2 \tag{6.22}$$

6.2.2 ANALYTIC SOLUTION OF LINEAR EQUATIONS

Solutions of (6.17) and (6.18) can be separated into two classes of mode shapes, i.e. symmetric and antisymmetric modes. Herein, a symmetric in-plane mode is defined as a mode in which the vertical component of the mode is symmetric, and vice-versa. We will treat the two classes separately.

We first consider antisymmetric modes. According to (6.20), the additional tension component h is zero, independent of the cable elasticity. Therefore, (6.17) reduces to

$$\frac{\partial^2 \tilde{q}}{\partial s^2} + \beta^2 \tilde{q} = 0. \tag{6.23}$$

Solving this equation and imposing the boundary conditions $\tilde{q}(0) = \tilde{q}(L/2) = 0$ yields

$$\tilde{q}_n(s) = A_n \sin(\frac{2\pi n s}{L}) \tag{6.24}$$

where the nondimensional frequencies are given by $\beta_n L = 2n\pi$ and $n = 1, 2, 3 \ldots$.

We next consider antisymmetric modes. Solving (6.17) and imposing the boundary conditions $\tilde{q}(-L/2) = \tilde{q}(L/2) = 0$ yields the following expression for $\tilde{q}(s)$:

$$\tilde{q}(s) = \frac{h\alpha}{LH\beta^2}(\frac{\cos(\beta s)}{\cos(\beta L/2)} - 1). \tag{6.25}$$

In order to determine the natural frequencies, (6.25) is substituted into (6.21), providing the following transcendental equation for βL:

$$\tan(\beta L/2) = \beta L/2 - \frac{4}{\lambda^2}(\beta L/2)^3 \tag{6.26}$$

As stated by Irvine and Caughey (1974), (6.26) "is of fundamental importance in the theory of cable vibrations." In physical terms, λ^2 expresses the ratio of elastic to catenary stiffness. For cables with low elastic stiffness, i.e. $\lambda^2 \to 0$, we recover the classic solution of the taut string equation, where

$$\lim_{\lambda^2 \to 0} \beta_n L = (2n-1)\pi, \quad n = 1, 2, 3 \ldots \tag{6.27}$$

For large values of λ^2, the cable can be considered inextensible, and (6.26) reduces to the transcendental equation for an inextensible catenary, where

$$\tan(\frac{\beta L}{2}) = \frac{\beta L}{2} \tag{6.28}$$

This equation was first derived by Rohrs (1851) and the first two roots are given by

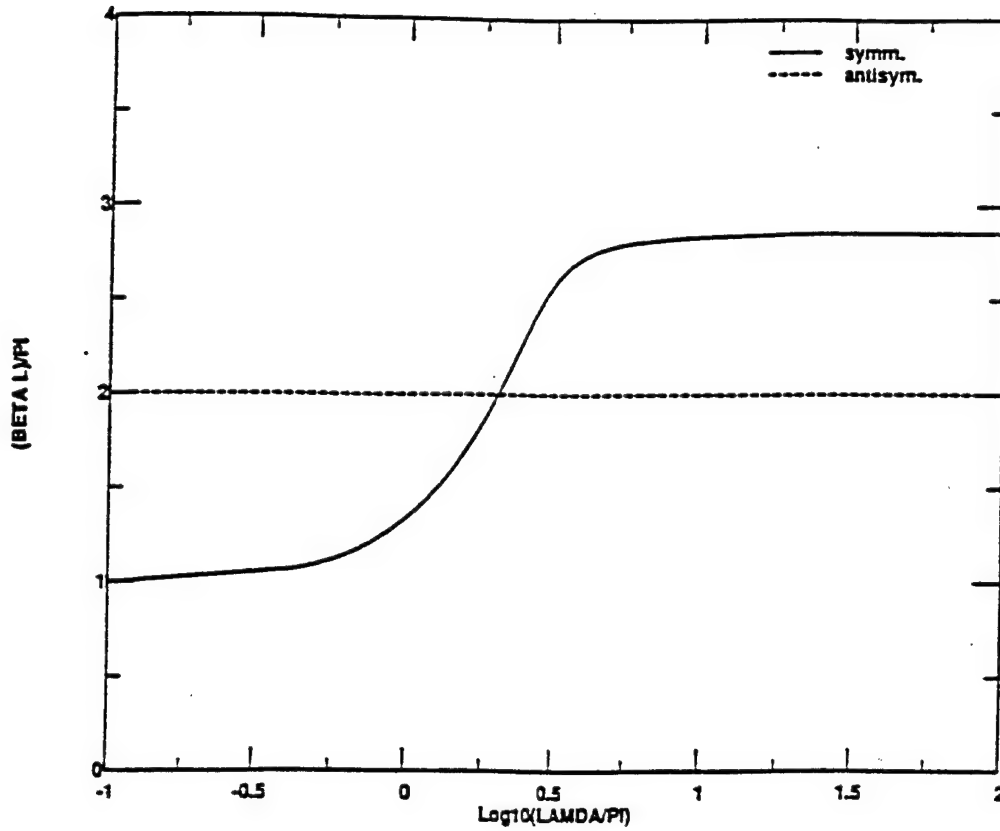Figure 6.2: Dependence of fundamental natural frequency on λ.

$$\lim_{\lambda^2 \to \infty} \beta_{1,2} L = 2.86\pi, 4.92\pi. \tag{6.29}$$

As derived previously, the fundamental frequency of antisymmetric modes is given by $\beta_1 L = 2\pi$. However, as we have shown, solutions for the two limiting values of λ^2 fall on either side of this value. The relationship between λ^2 and the first root of (6.26) is shown in figure 6.2. Of particular interest is that symmetric natural frequencies cross the antisymmetric frequency for increasing values of λ^2. The cross-over point for the first mode corresponds to $\lambda = 2\pi$, and a steep transition in frequency occurs near this value. Similar frequency cross-overs occur at other modes as well (Burgess, 1985).

The mode shapes for longitudinal modes can be determined by introducing (6.25) into (6.18) and integrating along the cable from $-L/2$ to s. Imposing the boundary condition $\bar{p}(-L/2) = 0$ yields

$$\bar{p}(s) = \frac{h}{H}(\frac{\alpha}{\beta L})^2 [(\frac{\beta L}{\lambda})^2 (s + L/2) + \frac{1}{\beta}(\frac{\sin(\beta s)}{\cos(\beta L/2)} + \tan(\beta L/2)) - (s + L/2)]. \tag{6.30}$$

Note that for symmetric normal modes, longitudinal modes are antisymmetric.

6.2.3 NUMERICAL RESULTS

In order to verify the numerical algorithm's ability to model elastic cable behavior, simulations of the suspended catenary problem were conducted for a range of λ values.
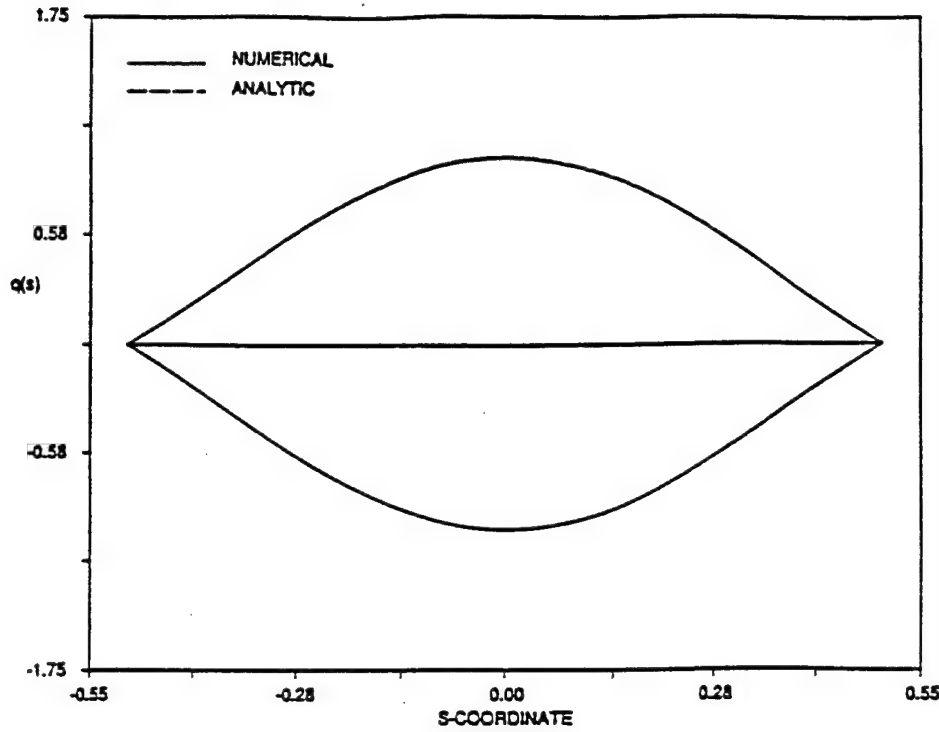
79

Figure 6.3: Transverse symmetric mode shape for $\lambda = \pi$; numerical and analytic results shown.

Specifically, we attempt to demonstrate numerically the transition in mode shapes predicted by linear theory.

As discussed, the linear equations are derived on the basis of small displacements from some known static configuration. Therefore, because the nonlinear terms are retained in the numerical model, excitation amplitudes were maintained at small values. A separate routine was developed to calculate the static shape, as input to the dynamic algorithm. In addition, the boundary conditions were modified, with the new conditions being given by

$$
\begin{aligned}
u(t, -L/2) &= 0 \\
v(t, -L/2) &= 0 \\
u(t, L/2) &= 0 \\
v(t, L/2) &= 0
\end{aligned}
\tag{6.31}
$$

Numerical solutions were obtained using a cable of unit length and the nondimensional parameters $\alpha = 0.1$ and $h/H = 0.01$. The normal and tangential velocities along the cable were initialized according to the linear solutions given by (6.25) and (6.30), respectively.

Numerical results for the calculated symmetric mode shapes, after 20 cycles have elapsed, are shown in figures 6.3, 6.4, and 6.5 for $\lambda = \pi$, 2π, and 3π, respectively. Also shown are the linear results derived previously. As readily seen, the two results are indistinguishable and the numerical algorithm is able to accurately model the modal transition that occurs.
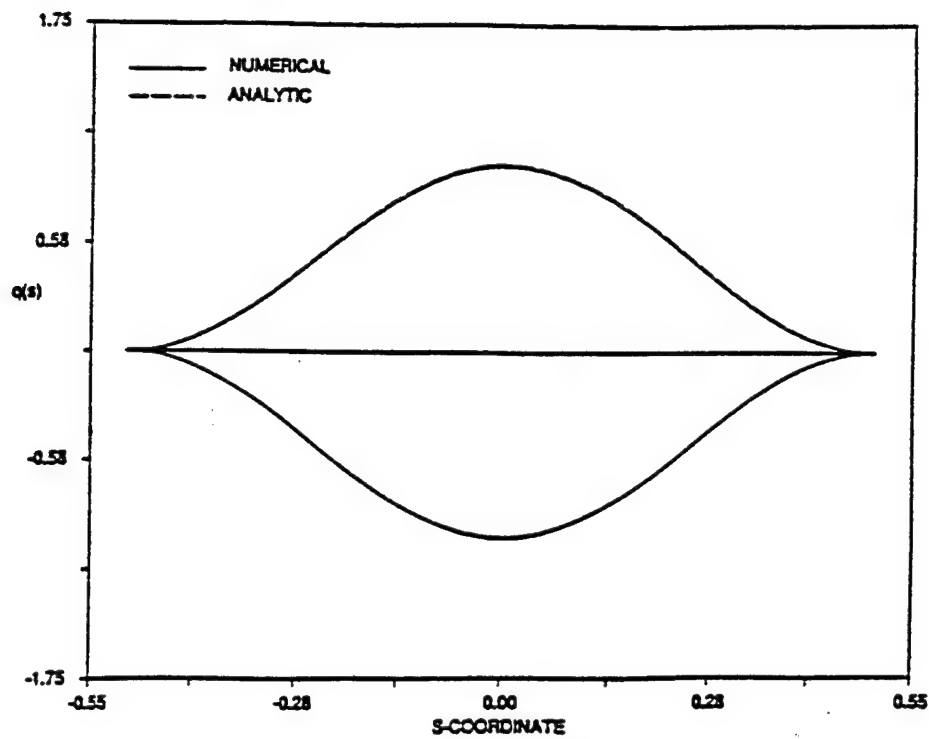
80

Figure 6.4: Transverse symmetric mode shape for $\lambda = 2\pi$ (cross-over point); numerical and analytic results shown.
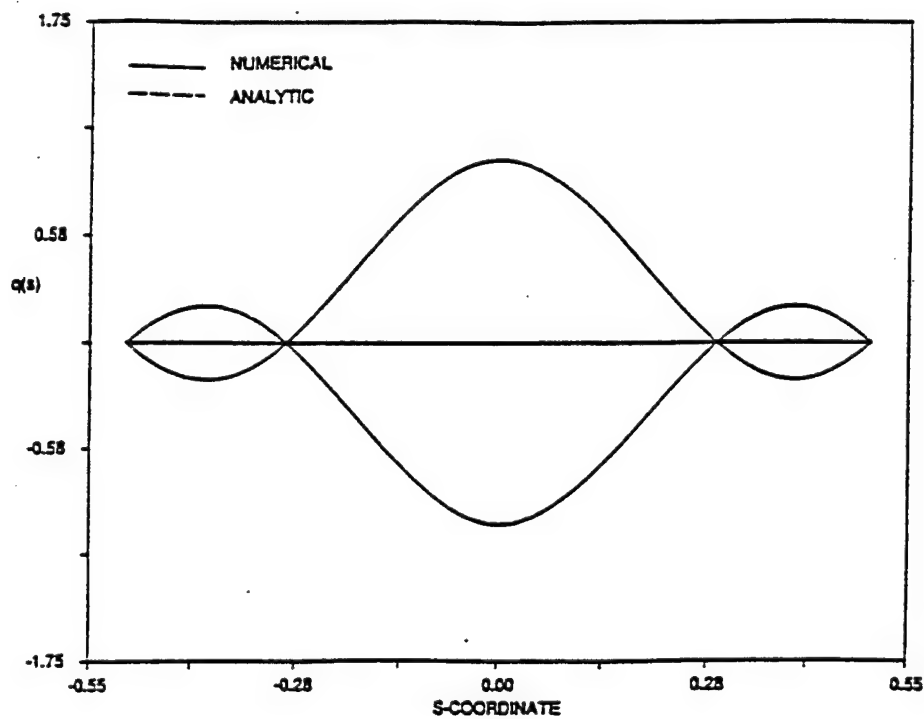

Figure 6.5: Transverse symmetric mode shape for $\lambda = 3\pi$; numerical and analytic results shown.

81

6.3 Extensible Dynamics of Hanging Chain

The asymptotic and numerical solutions of the hanging chain problem presented in §5 were obtained under the assumption that the chain was inextensible. In this chapter, we consider the extensible chain dynamics to verify the validity of this assumption. In addition, the effects of reducing the elastic stiffness in the chain are investigated to determine at which point elasticity becomes important.

6.3.1 MODERATE EXCITATION AMPLITUDES

The chain used throughout the experimental tests was comprised of steel links, roughly 5 mm in diameter. The equivalent nondimensional elastic stiffness was found to be on the order of $EA/w_o L = EA^* = 4 \times 10^5$. This value will be used as a reference value for determining the validity of neglecting elasticity. For this value of EA^*, the ratio of elastic to transverse wave speeds of of order 600 or greater. A synthetic chain of the same dimensions would have a ratio on the order of 60. The ratio of the fundamental elastic frequency to the driving frequency, assuming the elastic frequencies correspond to those associated with free-fixed end conditions, is given by

$$r_\omega = \frac{\pi [EA^*]^{1/2}}{\beta_n (1 + \sigma)} \tag{6.32}$$

where β_n is the nth root of the Bessel function of the first kind and order 0.

Numerical simulations were conducted using the excitation amplitude given in §5.4 ($Y_o = 0.0087L$), for a range of EA^* values. The excitation frequency was chosen to correspond to resonance, i.e. $\sigma = 0$. Figure 6.6 shows the tension time history, at four locations along the chain, obtained using $EA^* = 4 \times 10^3$. Also shown are the results for the inextensible chain. As readily seen, elastic effects are insignificant for values of elastic stiffness above this value. This is attributable to the excitation frequencies remaining in a narrow frequency band, well below the elastic frequencies. Therefore, for moderate excitation amplitudes, it proves valid to neglect elasticity.

Numerical results are shown in figure 6.7 for a chain with very low elastic stiffness ($EA^* = 100$). The results show only a slight shift in frequency and amplitude occurs due to elasticity. The first elastic natural frequency, in this case, is roughly 8 times the excitation frequency.

6.3.2 LARGE AMPLITUDE EXCITATION

Here we consider the large amplitude response of a chain with elasticity. Results are presented for the three cases listed in table 6.1. Figure 6.8 shows the tension time history, at four points along chain, using the value $EA^* = 4.0 \times 10^4$ (case 1). Note that this value is an order of magnitude below the reference value. As readily seen, elasticity does not affect the chain's dynamics for this case as elastic waves are not excited. These results show that the excitation energy, although broad-banded near the point of the chain's collapse, remains below the fundamental frequency of elastic waves. The frequency ratio in this case is large, as shown in table 6.1. Based on these results, and the results presented in the previously, we can conclude that the results obtained in §5, which are based on the assumption the chain is inextensible, are valid.
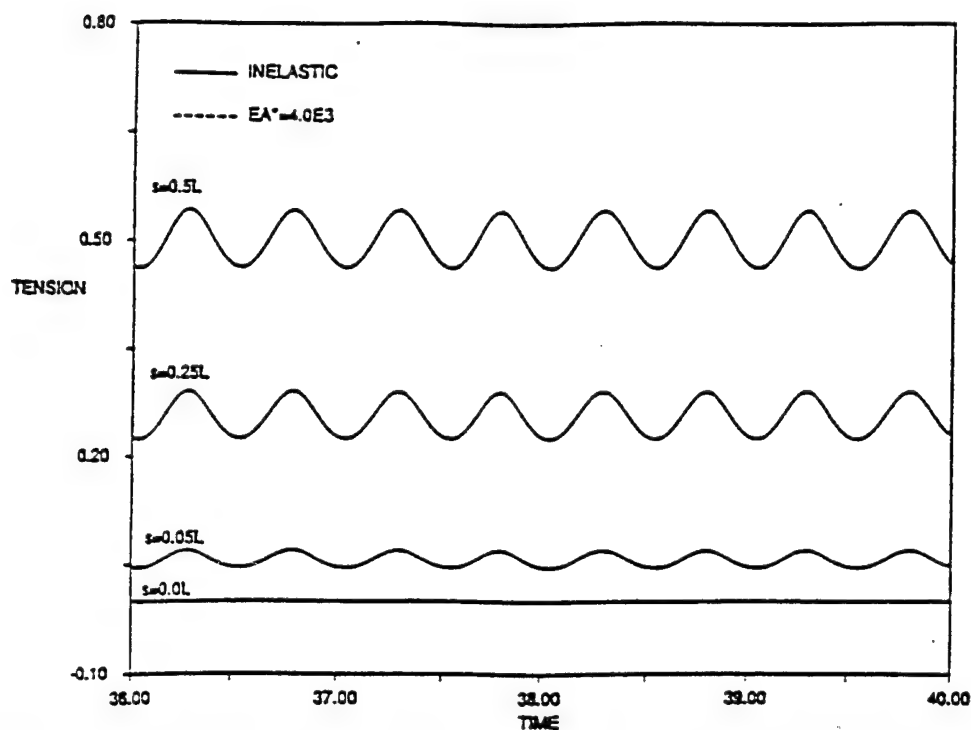
Figure 6.6: Comparison between tension time history at four locations along chain for inextensible chain and elastic chain ($EA^* = 4 \times 10^3$).
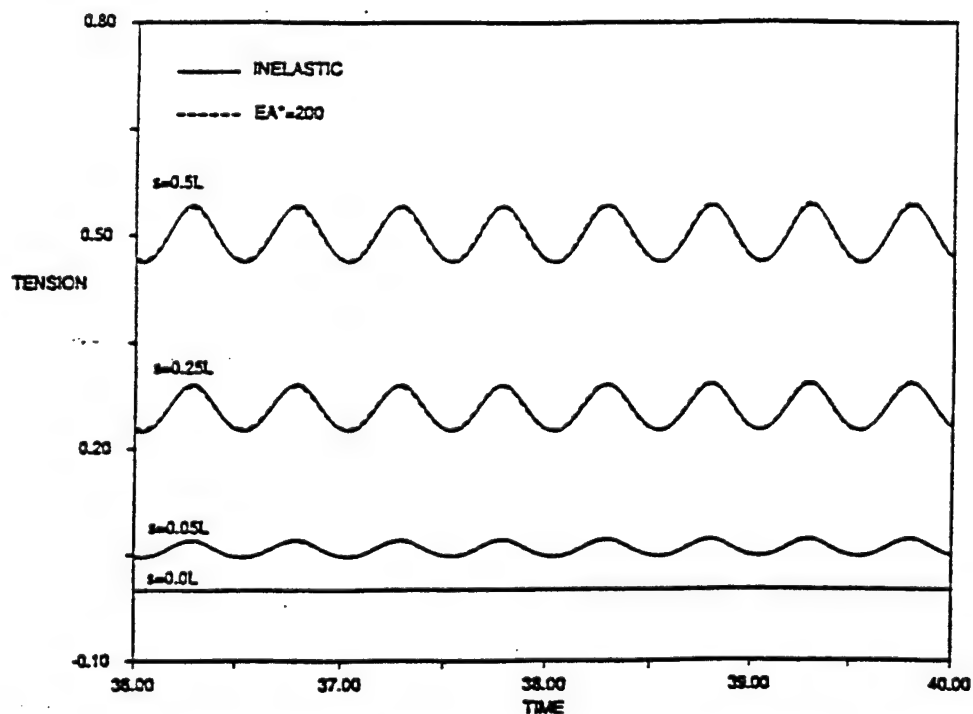

Figure 6.7: Comparison between tension time history at four locations along chain for inextensible chain and elastic chain ($EA^* = 200$).
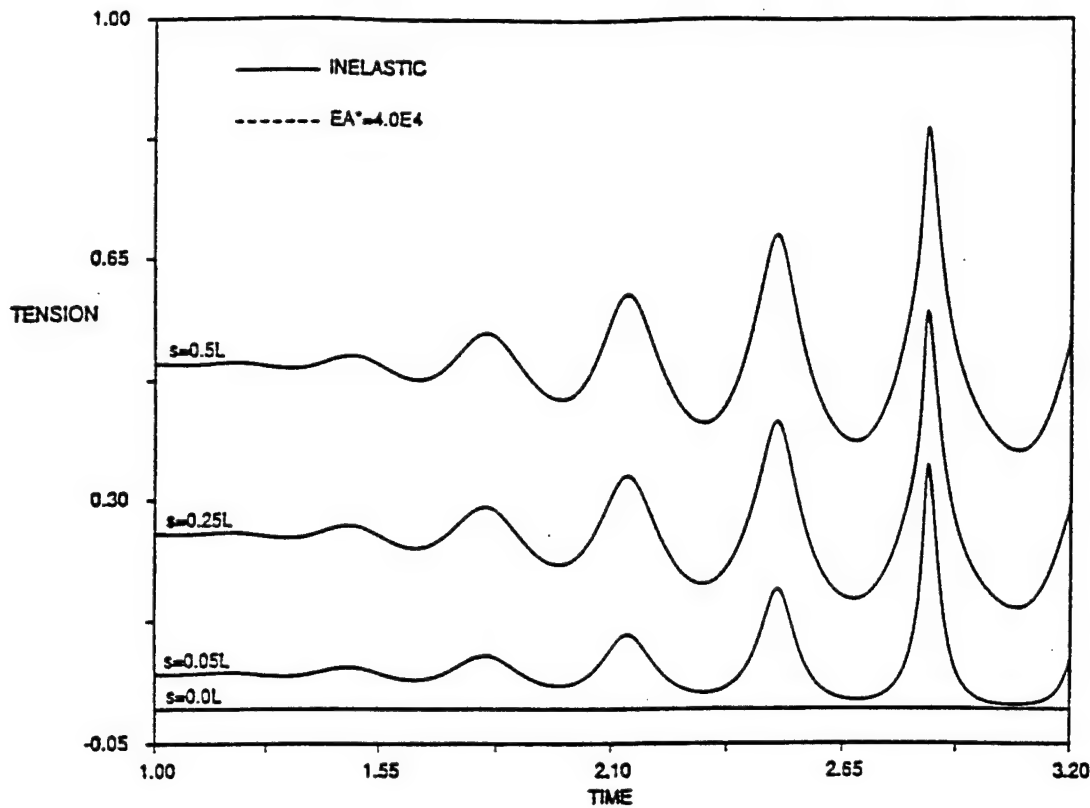
Figure 6.8: Comparison between tension time history at four locations along chain for inextensible chain and elastic chain ($EA^* = 4.0 \times 10^4$).

Case#	EA^*	ω^* (linear)	ω^* (observed)	r_ω
1	4×10^4	314.	—	80
2	4×10^3	99.3	113.	25
3	4×10^2	31.4	36.6	8

Table 6.1: Case studies for analysis of elastic affects.

We next consider the effects of reducing the elastic stiffness further (cases 2 and 3). For case 2 we find that elastic waves do begin to develop (figure 6.9) after the tension peaks become sufficiently narrow in time, i.e. begin to look impulsive. Prior to the point of maximum tension, no elastic effects are present. The observed frequency of the elastic waves (table 6.1) differs from the value predicted by linear theory by roughly 14 percent.

As shown in figure 6.9, the elastic wave amplitude grows in the direction away from the free boundary. The tension variation the occurs due to the elastic waves can be isolated by removing the tension found for the inextensible case. Here we find an interesting result. The elastic waves that form are not travelling waves. Instead, we find that a standing wave develops that encompasses the entire chain. The mode shape of this standing wave is shown in figure 6.10, along with the linear mode shape of a straight cable with free-fixed boundary conditions. As shown, the largest discrepancy occurs near the free-end. In this region the curvature is greatest and curvature has been shown to have a significant affect on the elastic frequencies and mode shapes (Burgess, 1988). Curvature effects, therefore,
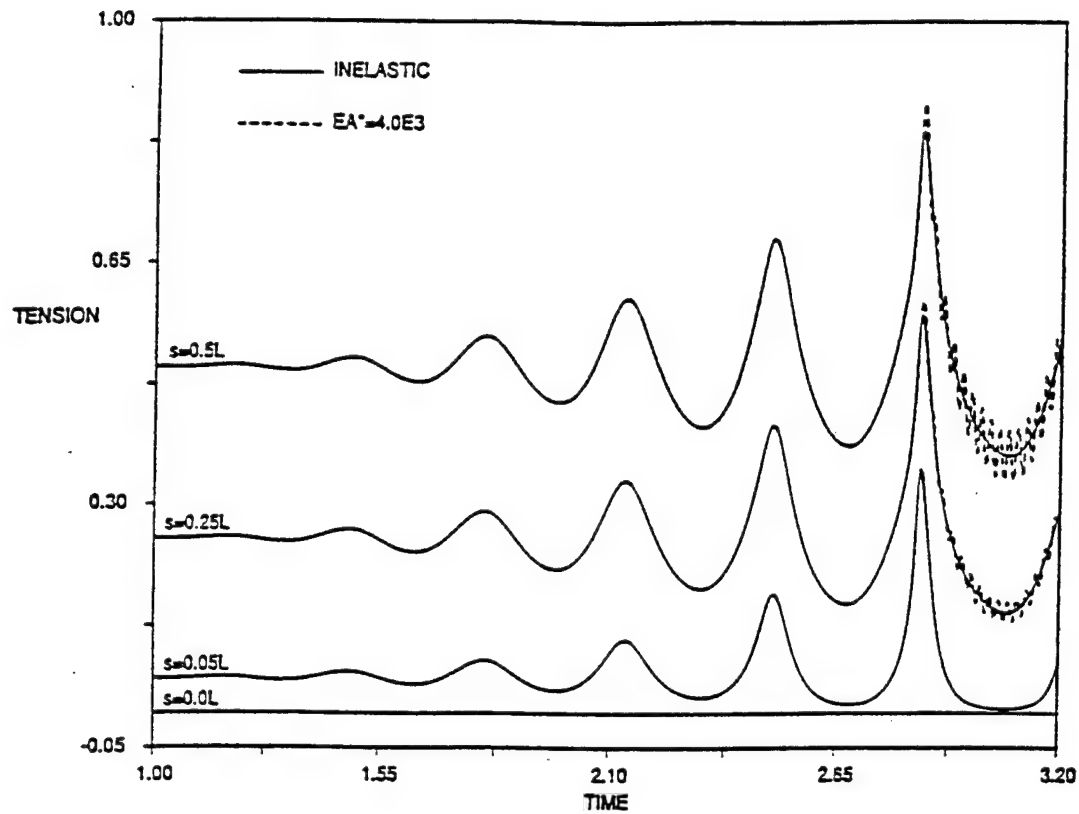
84

Figure 6.9: Comparison between tension time history at four locations along chain for inextensible chain and elastic chain, $EA^* = 4.0 \times 10^3$.

may also account for the discrepancy in the observed elastic frequency.

Further proof that the elastic waves are stationary is provided by a contour plot of the elastic tension variation along the chain in time (figure 6.11). As shown, the characteristics are vertical, indicating elastic energy does not travel along the cable. If the elastic waves did travel, the characteristics would have a finite slope, given by the elastic wave speed.
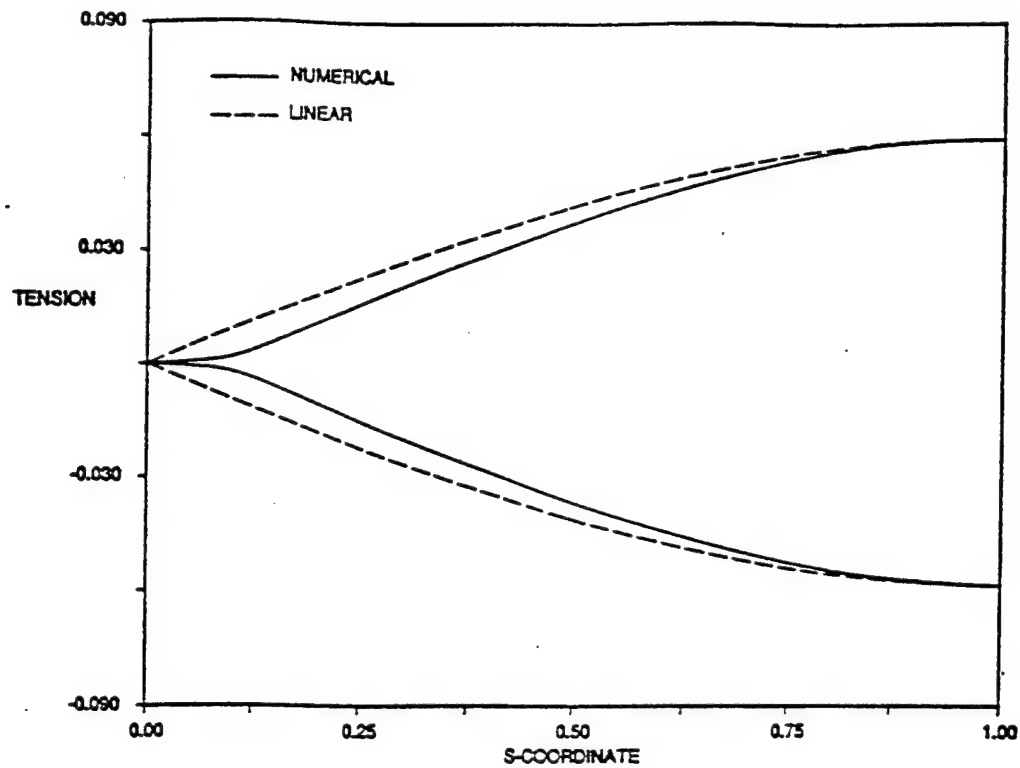
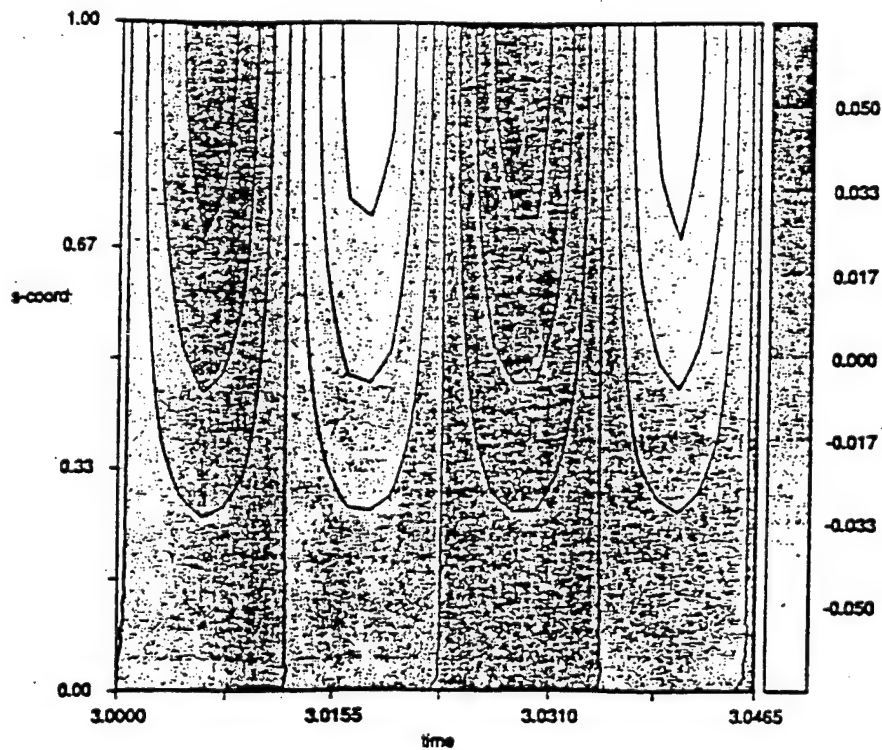Figure 6.10: Mode shape for tension variation due to elastic waves, using $EA^* = 4.0 \times 10^3$.

Figure 6.11: Contour plot of elastic tension variation in time and space for $EA^* = 4.0 \times 10^3$.

Similar results were obtained for still further reductions in the value of EA^* (case 3). Here, however, we find that elastic waves begin to develop at lower tension amplitudes (figure 6.12). In this case the fundamental elastic frequency is much closer to the excitation frequency, i.e $r_\omega = 8$. Again we find that the elastic waves are stationary and qualitatively similar results are found for the mode shape (figure 6.13) and characteristics (figure 6.14).
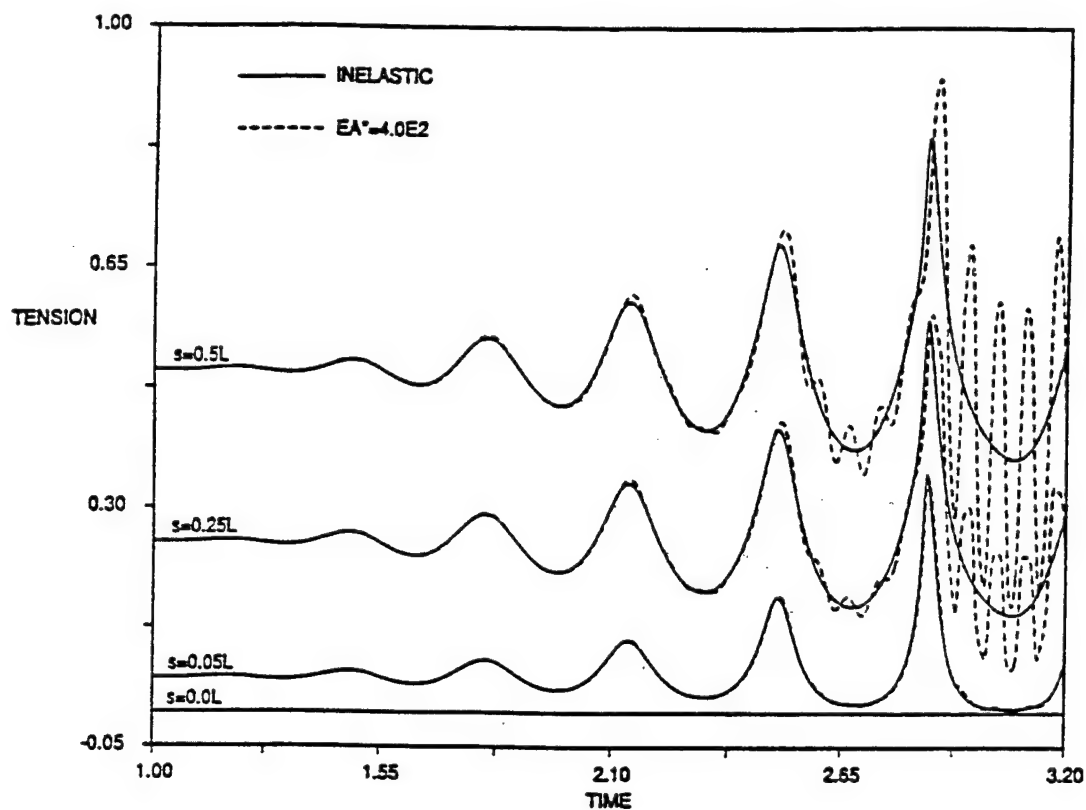

Figure 6.12: Comparison between tension time history at four locations along chain for inextensible chain and elastic chain, $EA^* = 4.0 \times 10^2$.
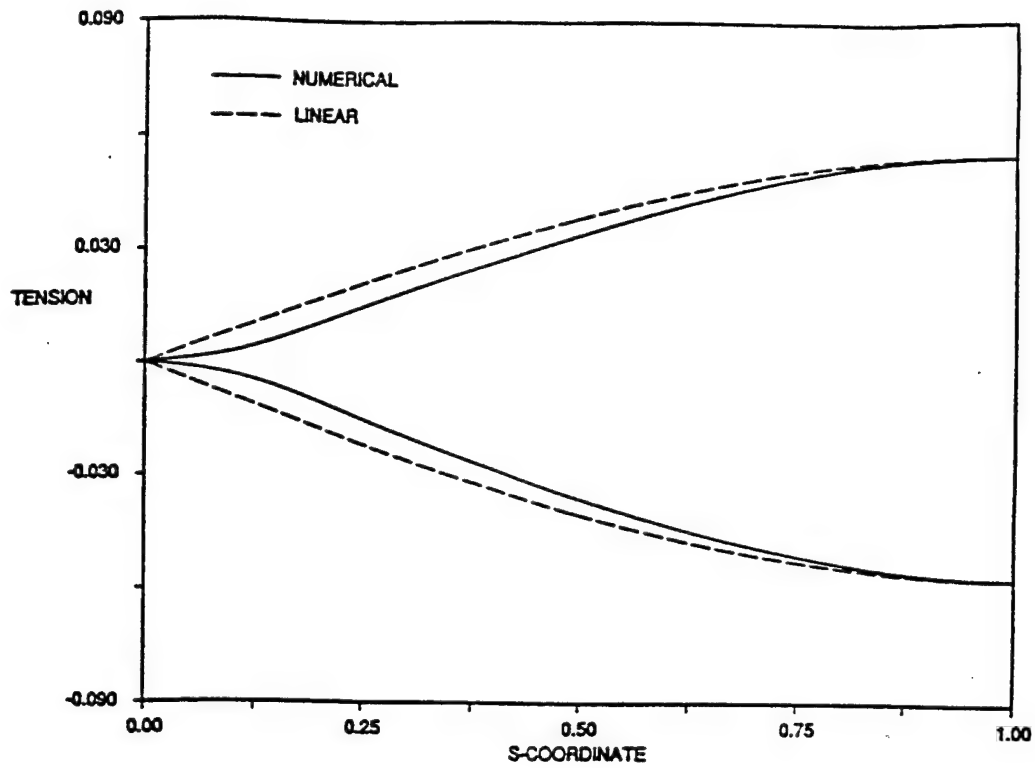
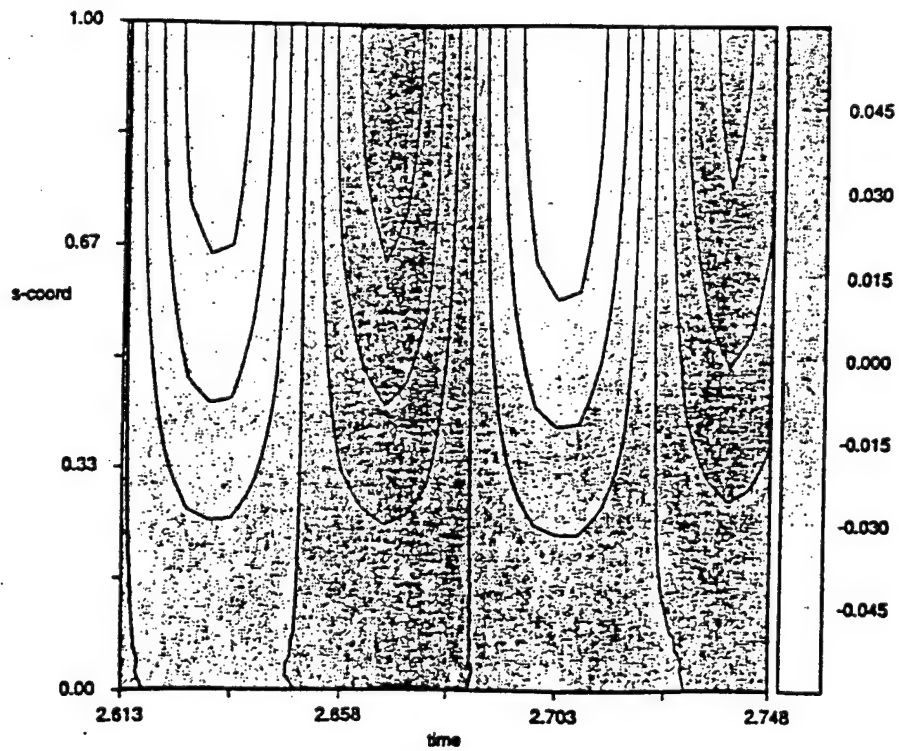Figure 6.13: Mode shape for tension variation due to elastic waves, using $EA^* = 4.0 \times 10^2$.

Figure 6.14: Contour plot of elastic tension variation in time and space for $EA^* = 4.0 \times 10^2$.

VII. HYDRODYNAMIC DAMPING IN VORTEX-INDUCED VIBRATIONS

7.1 Introduction

Elastically mounted cylinders and long, flexible cylinders experience vortex-induced vibrations when placed normal to a flow. The amplitude of this process is self-limiting with a maximum value approximately equal to one to two cylinder diameters. Laboratory experiments have been conducted to measure forces on rigid cylinders that are oscillated at a specific amplitude and frequency transversely to a uniform flow. These tests confirm that there is power input into the cylinder vibrations at small amplitudes of motion, for frequencies close to the Strouhal frequency of natural vortex formation, whereas there is dissipation for larger amplitudes (King 1977, Staubli 1983, Bearman 1984). When a cylinder oscillates with a frequency that is within a narrow range about the Strouhal frequency, the vortex formation process synchronizes with the motion of the cylinder in what is called a condition of *lock-in*. Under lock-in conditions, a vibrating cylinder is subject to a significantly increased drag force, up to three or more times higher than that of a stationary cylinder.

Hartlen and Currie (1970) and several other authors (Bearman 1984) used the van der Pol oscillator to represent qualitatively the self-limiting nature of the excitation lift force. Alternatively, the concept of energy balance has been incorporated in models to predict the response of long, flexible cylinders (Vandiver 1988). In these models, the direction of energy transfer is dependent on whether or not the motion of the cylinder at a particular point is correlated with the vortex formation process. Energy is assumed to be transferred from the fluid to the cylinder at points where the motion is synchronized with vortex shedding (lock-in condition), while it is assumed that the cylinder loses energy to the fluid at points where the motion is not correlated with vortex shedding. At these points, the loss of energy is modelled by an "equivalent" hydrodynamic damping term, calculated by linearizing the quadratic drag force acting on the cylinder.

In this section we show, on the basis of experimental results, that the vortex-induced lift force depends on the amplitude of the cylinder vibration in a manner which is characteristic of a process containing a purely linear damping term. This provides a direct way of evaluating the damping coefficient using laboratory measurements.

7.2 Hydrodynamic Damping Model for Harmonic Response

The force acting on a section of a slender circular cylinder of diameter d, vibrating harmonically in the transverse direction relative to an oncoming flow of velocity V, is a nonlinear function of the motion. We denote the lift force per unit span that is in-phase with the velocity by $L_v(t)$ and its amplitude by L_o and proceed to nondimensionalize it to obtain the lift coefficient that is in-phase with velocity, C_{L_v}:

$$C_{L_v} = \frac{L_o}{\frac{1}{2}\rho d V^2} \ , \tag{7.1}$$

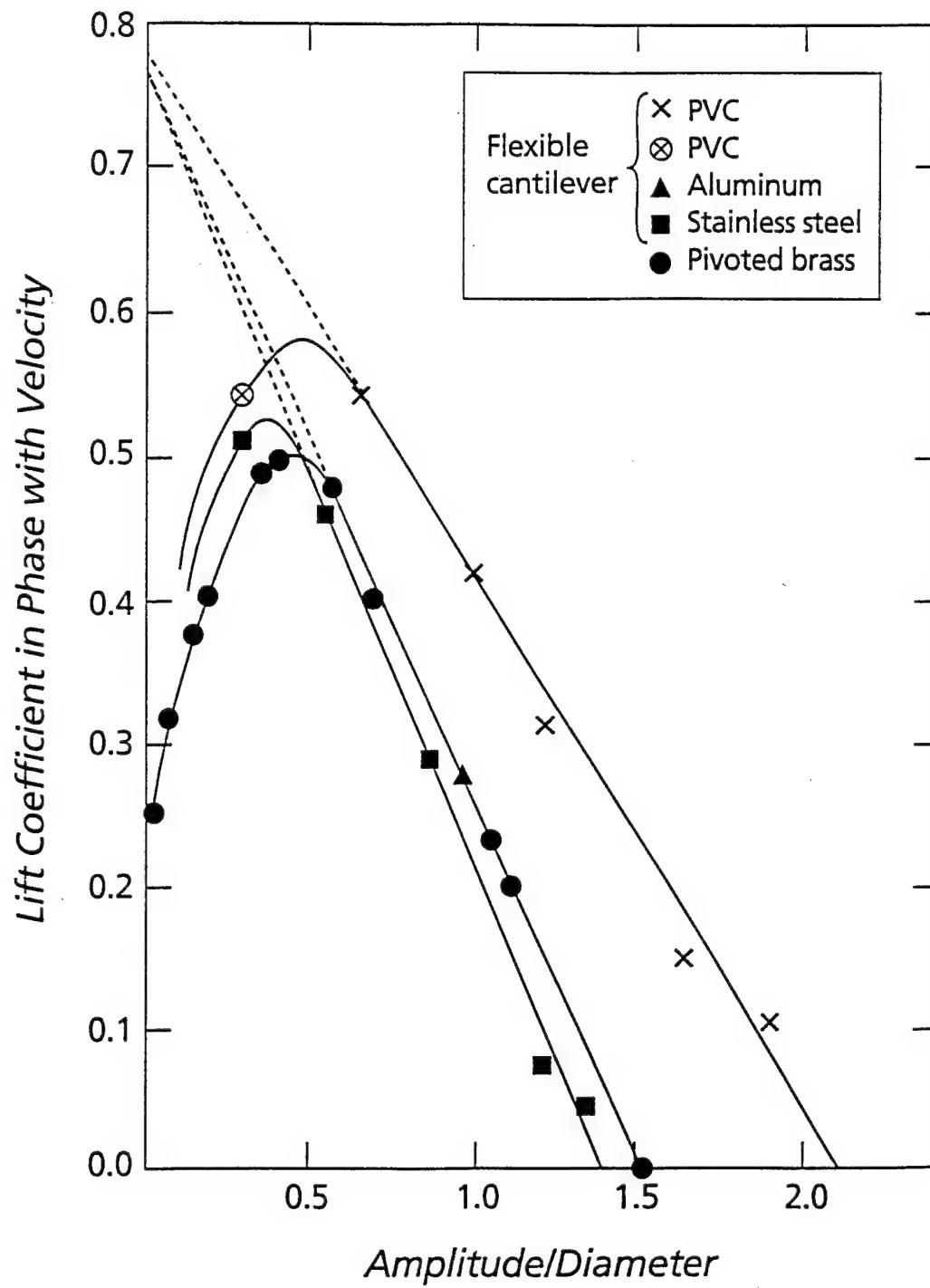where ρ denotes the fluid density.

Figure 7.1: The lift coefficient in-phase with velocity as a function of the amplitude-to-diameter ratio (King 1977).

Figure 7.1 shows a plot of the measured coefficient, C_{L_v}, of rigid pivoted cylinders versus the vibration amplitude for a nondimensional oscillation frequency close to the Strouhal number (King 1977). Power input occurs when C_{L_v} is positive and dissipation occurs when C_{L_v} is negative. Except for small amplitudes, when the vortex formation process is not well correlated along the span of the cylinder, there is clearly a linear relation between the lift coefficient and the amplitude of motion. Over a range of practical interest, typically for amplitude to diameter ratios higher than 0.4, the curve can be approximated by a straight line with negative slope. This is a distinct feature of a nonlinear process that contains a term that can be modelled through a linear damping coefficient. The damping coefficient can be directly obtained from the slope of the line. A simple representation of the lift force curve is

$$C_{L_v} = C_o - \lambda \frac{A}{d} \ , \tag{7.2}$$

where $\frac{A}{d}$ is the amplitude-to-diameter ratio and C_o and λ are curve-fitting constants. Equation (2) is accurate if the cylinder vibrates with an amplitude that is larger than the threshold amplitude.

It should be noted that the methodology to replace an amplitude-dependent excitation by equivalent motion-dependent terms has been applied before in other fields to analyze nonlinear phenomena, such as the value of wave-drift damping estimated from second order wave forces (Faltinsen 1990).

Experiments have been conducted in the MIT Testing Tank Facility on rigid circular cylinders of diameter 2.54 cm and span 30 cm, forced to move in a prescribed motion transversely to a flow with constant velocity V (Gopalkrishnan 1992). Figure 7.2 shows several plots of the coefficient, C_{L_v}, for harmonic motion versus the amplitude-to-diameter ratio for various imposed frequencies, which are near the frequency of the maximum in-phase lift coefficient. It is interesting to note that the slope of the various curves varies little over a range of nondimensional frequencies, $\frac{fd}{V}$, where f is the oscillation frequency in Hertz.

For a purely sinusoidal force at circular frequency $\omega = 2\pi f$, equation 7.2 provides the component of the lift force in phase with velocity:

$$L_v(t) = \frac{1}{2}\rho d V^2 \left(C_o - \lambda \frac{A}{d}\right) \sin \omega t, \tag{7.3}$$

If we define

$$L_e(t) = \left(\frac{1}{2}\rho d V^2\right) C_o \sin \omega t, \tag{7.4}$$

$$b_h = \left(\frac{1}{2}\rho d V^2\right) \frac{\lambda}{\omega d}, \tag{7.5}$$

$$v(t) = \omega A \sin \omega t \tag{7.6}$$

where $v(t)$ is the cylinder velocity, we can write equation 7.3 more simply as

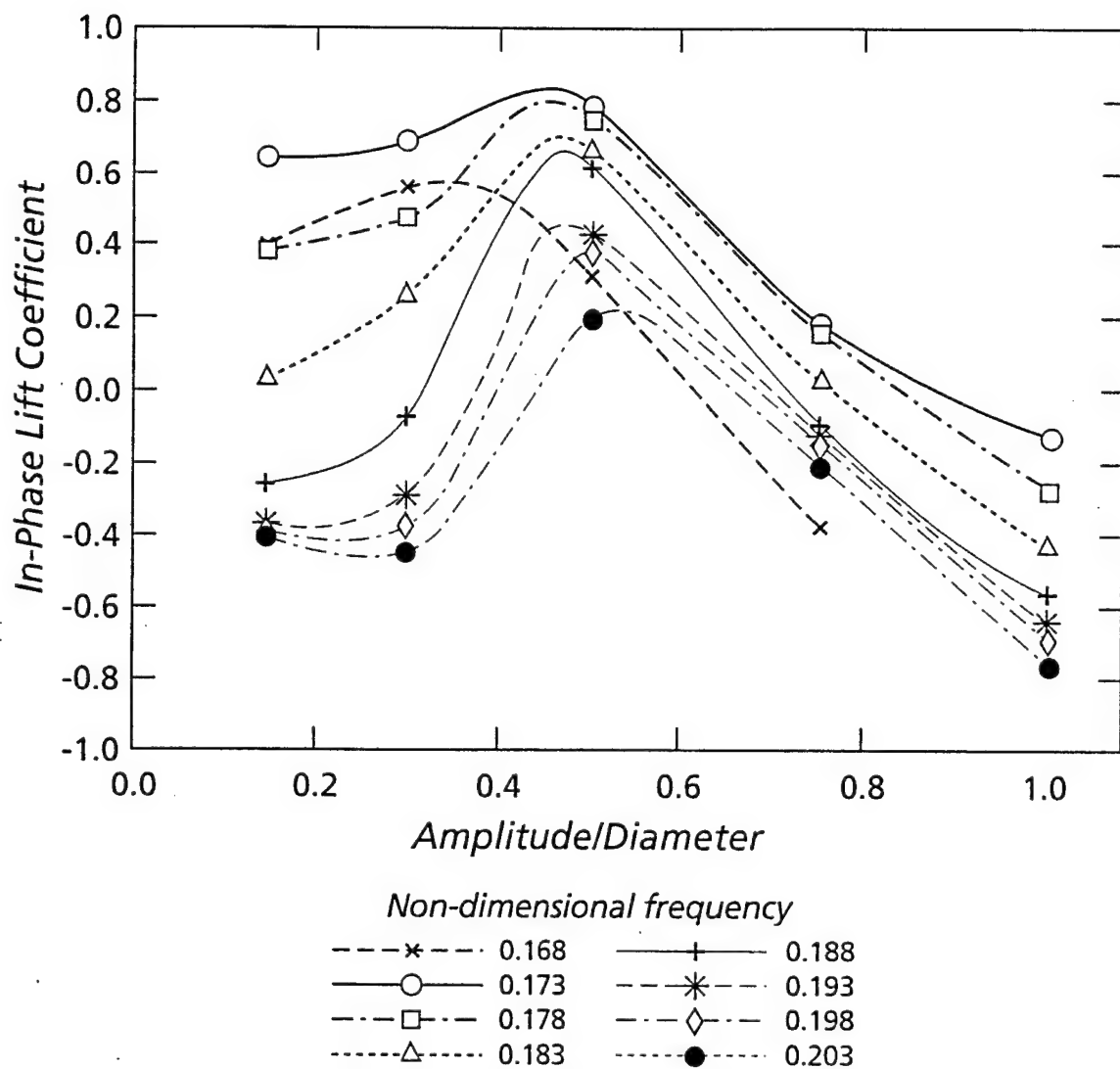$$L_v(t) = L_e(t) - b_h v(t). \tag{7.7}$$

91

Figure 7.2: Experimental measurements (Gopalkrishnan 1992) of the lift coefficient in-phase with velocity as a function of the amplitude-to-diameter ratio for various values of the nondimensional frequency parameter $\frac{fd}{V}$.

In equation 7.7, the lift force that is in-phase with the cylinder velocity is decomposed into two parts, one of which is a pure excitation force $L_e(t)$ and a second term which is a linear damping force $b_h v(t)$. Equation 7.5 can be used to obtain a direct estimate of the hydrodynamic damping coefficient b_h, once the curve-fitting constant λ is determined from experimental data. We define the hydrodynamic damping ratio, ζ_h, as:

$$\zeta_h = \frac{b_h}{2m\omega} = \frac{\rho}{\rho_c} \frac{1}{4\pi^3} \frac{\lambda}{St^2}, \tag{7.8}$$

where m is the mass per unit length of the cylinder and ρ_c is the cylinder density. We have assumed that the harmonic motion is at the Strouhal frequency $\omega_v = 2\pi f_v$ and write the Strouhal number as $St = \frac{f_v d}{V}$. Then, taking a metallic cylinder with specific density equal to 5.0, specifying a Strouhal number of $St = 0.17$, and calculating $\lambda = 1.36$ from the experimental data in figure 7.2, we find that $\zeta_h = 0.076$ (7.6% of critical).

Both the damping coefficient, b_h, and the pure excitation force in the direction of the velocity, L_e, are independent of amplitude. The excitation force, however, is phase-correlated with the velocity. This is important in any numerical calculation, as shown in the sequel. For most applications in water, the structural damping is small in comparison to hydrodynamic damping and may be neglected. In air, the structural damping is significant and may be added directly to b_h.

7.3 Hydrodynamic Damping for Narrow-Band Response

Lock-in of a flexibly mounted cylinder, or a flexible structure is usually characterized by a narrow-band response with characteristic beating oscillations. We can extend heuristically the derivation of §2 to apply to these cases when the response is not harmonic. For example, a three-dimensional plot of the lift coefficient in phase with velocity as function of the amplitude-to-diameter ratio and the frequency of oscillation can be constructed from figure 7.2. Such plots have been provided by Staubli (1983) and Gopalkrishnan (1992). The lift force that is in-phase with the velocity can be then represented then by the following, more general equation

$$C_{L_v}(\omega) = H(\omega)C_o - \Lambda(\omega)\lambda\frac{A}{d} , \tag{7.9}$$

which is similar to equation 7.2, but includes the frequency dependence ω in the curve-fitting parameters H and Λ. The functional form of the curve-fitting parameters is determined from experimental data, and C_o and λ are as defined before. Because of the similarity in the the shapes of the curves in figure 7.2, we conclude that $\Lambda(\omega)$ is very nearly constant over a narrow frequency range and is equal to one. This results in considerable simplification for use in numerical calculations.

The accuracy of equation 7.9 is subject to the same amplitude-threshold considerations as those related to equation 7.2. In addition, one must note that, in order for equation 7.9 to apply to a multi-frequency response, linearity must be assumed, which is not the case for all parameters relevant to vortex-induced oscillations. For example, the excitation force for monochromatic excitation at nonlock-in conditions contains an additional component at the Strouhal frequency. Thus, in order to employ equation 7.9, we must assume that the dominant force component has a frequency content that is within a narrow band around a specific frequency ω, and that the response is still within the lock-in regime. Triantafyllou

and Karniadakis (1989) have shown numerically and Gopalkrishnan (1992) and Gopalkrishnan *et al.* (1992) have shown experimentally that, in the case of a beating oscillation, i.e., an oscillation consisting of two (or three equidistant) sinusoidal components, the harmonic results can be used to predict the lift force in a multi-frequency response, provided that the frequencies are sufficiently close together and within the lock-in regime. However, the drag force in a multi-frequency response can not be calculated on the basis of harmonic results.

Hence, assuming that harmonic data can be used to calculate the lift force in a narrow-band response, we can write H and Λ as integro-differential operators in the time domain. The damping, as expressed by the term containing Λ, is still linear and resembles, in form, the well-known, frequency-dependent damping of floating bodies in the presence of a free surface (Faltinsen 1990).

If the cylinder motion has a narrow-band spectrum about $\omega = \omega_v$, then we can exploit the fact that the slope of the lift-force coefficient in-phase with the velocity for a given imposed amplitude appears to be nearly frequency-independent (figure 7.2), and we can write the time-dependent lift force approximately as

$$L_v(t) = \left[\frac{v(t)}{\hat{v}(t)}\right] L_{eo} - b_h v(t) \ , \tag{7.10}$$

where $\hat{v}(t)$ is the slowly varying envelope of $v(t)$. The damping coefficient, b_h, is given by equation 7.5 with $\omega = \omega_v$, and L_{eo} is approximately given as

$$L_{eo} = H(\omega_v) C_o \left(\frac{1}{2}\rho d V^2\right) \ . \tag{7.11}$$

As with the case of the purely sinusoidal response, the expression for b_h is simple and can be determined directly from experimental data (figure 7.2). The difficulty in this case consists of ensuring that the excitation is indeed properly correlated with the velocity. This is straightforward in time-domain simulations, since one must calculate the envelope of the velocity at each time step before using equation 7.10. Often, however, frequency domain techniques are employed, resulting in considerable savings in computational expense; an additional requirement must then be imposed, to ensure that the excitation is properly correlated, viz.

$$\left[\lim_{T\to\infty} \frac{1}{T} \int_0^T L_e(t)v(t)dt\right]^2 = \frac{1}{2}L_o^2 \left[\lim_{T\to\infty} \frac{1}{T} \int_0^T v(t)v(t)dt\right] \ , \tag{7.12}$$

where

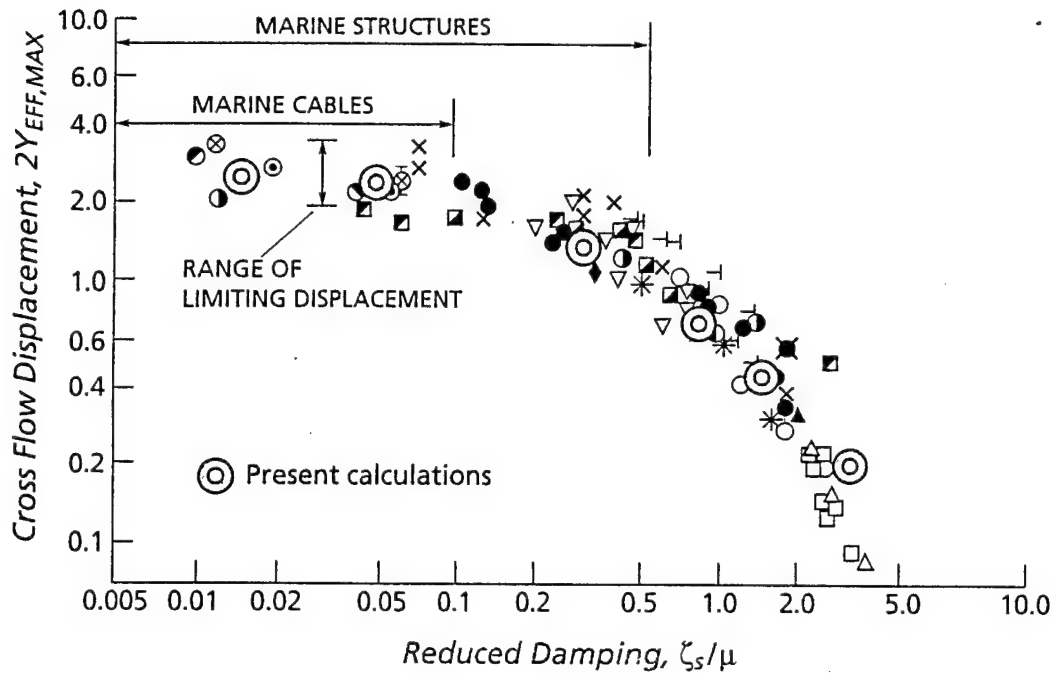$$L_o = \left(\frac{1}{2}\rho d V^2\right) C_o \ . \tag{7.13}$$

Figure 7.3: Comparison between the measurements of the maximum double-amplitude motion of a circular cylinder as a function of the reduced damping $\frac{\zeta}{\mu}$ (Griffin 1981) and calculations using the method outlined here.

7.4 Applications

Below, we provide the results of simple calculations of the vortex-induced response of cylinders based on the concepts and equations derived in §7.2 and §7.3.

7.4.1 SPRING-MOUNTED, RIGID CYLINDER IN A UNIFORM CURRENT

We begin by considering the narrow-band, lock-in response of a flexibly-mounted, rigid cylinder. The natural frequency of the system is equal to the frequency of maximum lift coefficient in-phase with the velocity. A compilation of data for vibrating cylinders as a function of the reduced damping from Griffin (1981) is shown, for comparison, in figure 7.3. The reduced damping is defined as the ratio of the structural damping ratio ζ_s and the quantity μ, where

$$\zeta_s = \frac{b_s}{2m\omega} \ , \tag{7.14}$$

$$\mu = \frac{\frac{1}{2}\rho d V^2}{m\omega^2 d} \ . \tag{7.15}$$

The term b_s is the structural damping coefficient per unit span.

95

Superimposed on the figure are calculations by the present method. Here, we have modelled the transverse motion, $y(t)$, of a rigid cylinder of unit span, having a mass m, mounted on a spring of constant k and a linear dashpot of constant b_s, and placed transversely to a constant flow of velocity V. The following is the equation of motion that is used for the calculations

$$m\frac{d^2y(t)}{dt^2} + b_s\frac{dy(t)}{dt} + ky(t) = f(t) \ . \tag{7.16}$$

The right hand side of the equation, $f(t)$, is the fluid force, which is written as the sum of an added mass term and the lift force in-phase with the velocity, which is further decomposed in accordance with equation 7.9. The method of harmonic balance together with equation 7.12 provides the solution plotted in figure 7.3. The calculations show good agreement with experimental data, even for large values of structural damping when the response is smaller than the threshold value.

7.4.2 TAUT STRING IN A SHEAR CURRENT

For the next application, we consider a taut string of length L placed transversely to a spatially-varying current with nominal velocity V. The transverse response of the string, $y(t, s)$, is assumed to be described accurately by the following linear structural model and a hydrodynamic force, $f(s, t)$,

$$m\frac{\partial^2y}{\partial t^2} + b_s\frac{\partial y}{\partial t} = \frac{\partial}{\partial s}\left[T(s)\frac{\partial y}{\partial s}\right] + f(s, t) \ , \tag{7.17}$$

where s is the Lagrangian coordinate along the string, $T(s)$ is the static tension, m is the mass per-unit-length and b_s is the structural damping per-unit-length. The force, $f(s, t)$, can be decomposed into the approximate form of equation 7.10 with a hydrodynamic damping force and an excitation force that is in-phase with the velocity. The decomposition also yields a term that represents the added mass force. It is further assumed that the characteristic wavelength of the string oscillations is much smaller than the length of the string, hence the response is effectively that of an infinitely long string.

An important consideration in studying the response of long structures is the length over which the vortex formation process can be assumed to be correlated. It is assumed herein that vortex shedding is fully correlated over half of a wavelength of a travelling wave. This is based on experimental measurements by Ramberg and Griffin (1976), who evaluated the cross-correlation between velocities measured at two locations in the wake of a vibrating cable, separated by a distance s along the axis of the cable: They found nearly perfect correlation for all points between two successive nodes of the vibrating cable for vibrational amplitudes above a threshold value. Also, Gharib (1989) showed through visualization of the response of a flexible cylinder that there is full correlation in the vortex formation process between two successive nodes, while, at the nodes, longitudinal vortical structures destroy any vortex interconnection. The frequency of excitation within a half wavelength is assumed to be equal to the frequency at the anti-node, where the maximum amplitude occurs.

Equation 7.17 can be solved together with equation 7.10 to provide the time-domain response of a cable, even when the response is not monochromatic. The present analysis is applicable provided that the response is narrow-banded and the maximum response amplitude is larger than about 0.4 diameters.

96

Here, we used standard frequency-domain techniques to solve equations 7.10 and 7.17 and obtain the vibration amplitude of a tow cable in a shear current. The presence of shear current causes the vortex-induced vibrations to be amplitude modulated. The excitation force depends on the slowly varying envelope of the velocity of vibration, hence the solution is obtained by iteration. Once we calculate the vibration amplitude, we use the laboratory measurements of Gopalkrishnan (1992) to estimate the drag coefficient.

We compared our predictions against the following data from full-scale experiments of towed cables in shear currents:

1. Data from Yoerger *et al.* (1991) for run 1A in the authors' notation, involving a 1,200-meter cable towed nearly vertical at 0.5 m/s in the presence of a measured shear current. The configuration of the cable was recorded using acoustic transponders, and from these measurements the drag coefficient was estimated to be equal to 2.47 ±0.24. By using the measured shear current and the procedure outlined above, we obtained a spatially varying drag coefficient along the cable length, between the values of 2.0 and 2.7, with an average value of 2.21.

2. Data from Yoerger *et al.* (1991) for run 2A involving an 800-meter cable towed at 0.5 m/s in the presence of a shear current. The calculations provided an average drag coefficient of 2.05. The measured full-scale drag coefficient was 2.24 ±0.24.

3. Data from figure 14 in Grosenbaugh (1991) for a cable 1,200-meters long towed nearly vertically in a transient condition. Our calculations gave a spatially varying drag coefficient in the range of 1.7 to 2.7, with an average value of 2.08. The average drag coefficient from the full-scale measurements was 1.95 ±0.20.

4. Data from figure 3 in Grosenbaugh (1991) corresponding to a 1,200-meter tow cable that had reached steady-state conditions. The calculation provided a spatially varying drag coefficient in the range of 1.6 to 2.4, with an average value of 1.95. The estimated average drag coefficient from the full-scale measurements was 2.15 ±0.20.

7.5 Summary

The basic result of the present work is that a linear hydrodynamic damping term is an intrinsic feature of vortex-induced vibrations in the lock-in regime, as experimental results demonstrate. The value of the linear damping term can be obtained directly from forced-motion tests on rigid cylinders. This allows simple and efficient calculations of the vortex-induced response under lock-in conditions of flexibly-mounted, rigid cylinders and long flexible cylinders.

VIII. VORTEX-INDUCED VIBRATIONS AND DRAG AMPLIFICATION IN SHEAR FLOWS

Michael S. Triantafyllou
Department of Ocean Engineering
Massachusetts Institute of Technology

1. INTRODUCTION

FOCUS: THE AMPLITUDE OF VIBRATION
          AND RESULTING DRAG
          COEFFICIENT AMPLIFICATION IN
          SHEAR FLOWS OF CABLES AND
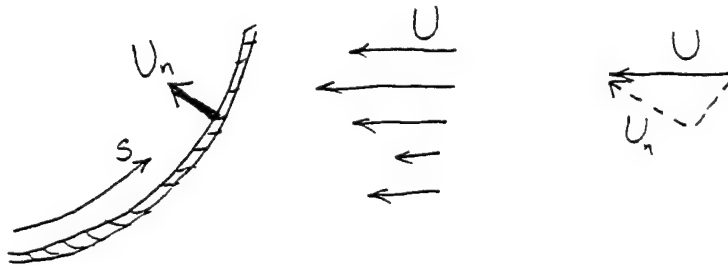   MOORINGS

FIGURE 1

IN A SHEAR FLOW AND/OR WHEN THE
CABLE IS CURVED THE NORMAL VELOCITY
TO THE CABLE VARIES WITH THE LENGTH (s)

AS A RESULT THE FREQUENCY OF VORTEX
FORMATION f_v VARIES ALSO

$$f_v = (St) \frac{U_n}{d}$$

$$(St) \simeq 0.20$$

$$d = cable \ diameter$$

WHEN YOU SUPERPOSE TWO SINUSOIDS OF
DIFFERENT FREQUENCY, ω_1 AND ω_2, _BEATING_
OSCILLATIONS RESULT IF

$$|\omega_1 - \omega_2| << \quad \omega_1, \omega_2$$

BEATING OSCILLATIONS ARE CHARACTER-
ISTIC OF CABLE VIV IN SHEAR FLOWS

$$\sin\omega_1 t + \sin\omega_2 t = 2\sin\left(\frac{\omega_1+\omega_2}{2} t\right)\cos\left(\frac{\omega_1-\omega_2}{2} t\right)$$

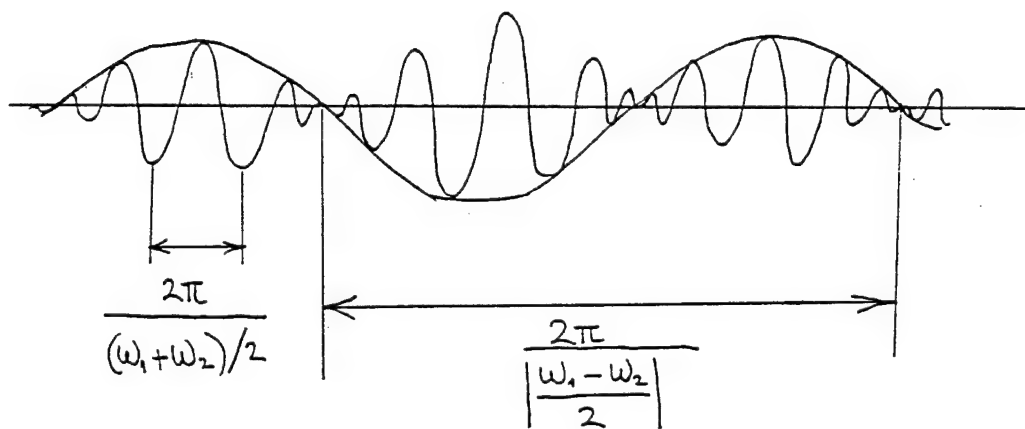$$\frac{2\pi}{(\omega_1+\omega_2)/2}$$

$$\frac{2\pi}{\left|\frac{\omega_1-\omega_2}{2}\right|}$$
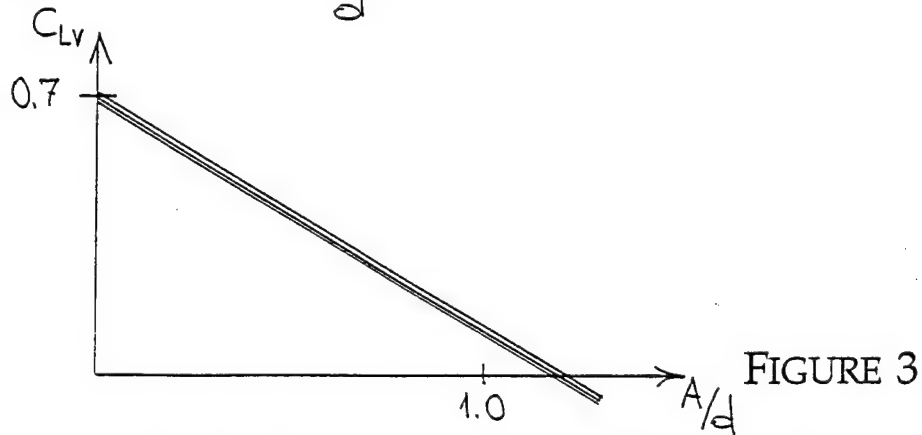
FIGURE 2

100

2. EXCITATION

THE EXCITATION IS CAUSED BY THE LIFT FORCE PER UNIT LENGTH:

$$F(t) = \frac{1}{2} \rho \, C_L(t) \, d \, U_n^2$$

WHERE $C_L(t)$ VARIES NEARLY SINUSOIDALLY IN TIME AT FREQUENCY EQUAL TO (1) THE STROUHAL FREQUENCY (STATIONARY CYLINDER), (2) THE EXCITATION FREQUENCY (LOCK-IN REGION), (3) COMBINATION OF EXCITATION AND STROUHAL FREQUENCIES (NON-LOCK-IN), (4) COMBINATION FREQUENCIES WHEN EXCITED BY MANY SINUSOIDS.

(1) WHEN THE CYLINDER IS STATIONARY, $C_L(t)$ VARIES AT f_v, AND HAS A <u>POSITIVE</u> COMPONENT WITH RESPECT TO VELOCITY (I.E. IT PUTS ENERGY IN THE SYSTEM).

IF THE CYLINDER IS EXCITED AT FREQUENCY f_v AND AMPLITUDE A, THEN THE LIFT COEFFICIENT IN PHASE WITH VELOCITY, C_{LV} DECREASES IN MAGNITUDE ALMOST LINEARLY AND BECOMES NEGATIVE AT $\frac{A}{d} \simeq 1.0$

FIGURE 3

(2) WHEN THE CYLINDER IS EXCITED AT $f \neq f_v$ AND AMPLITUDE A, THE SAME PLOT IS OBTAINED AS ABOVE BUT WITH SMALLER AMPLITUDE INITIALLY.
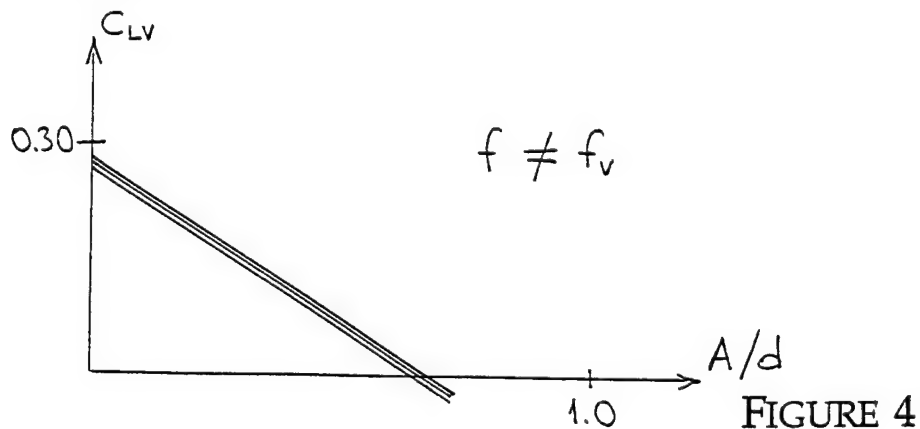
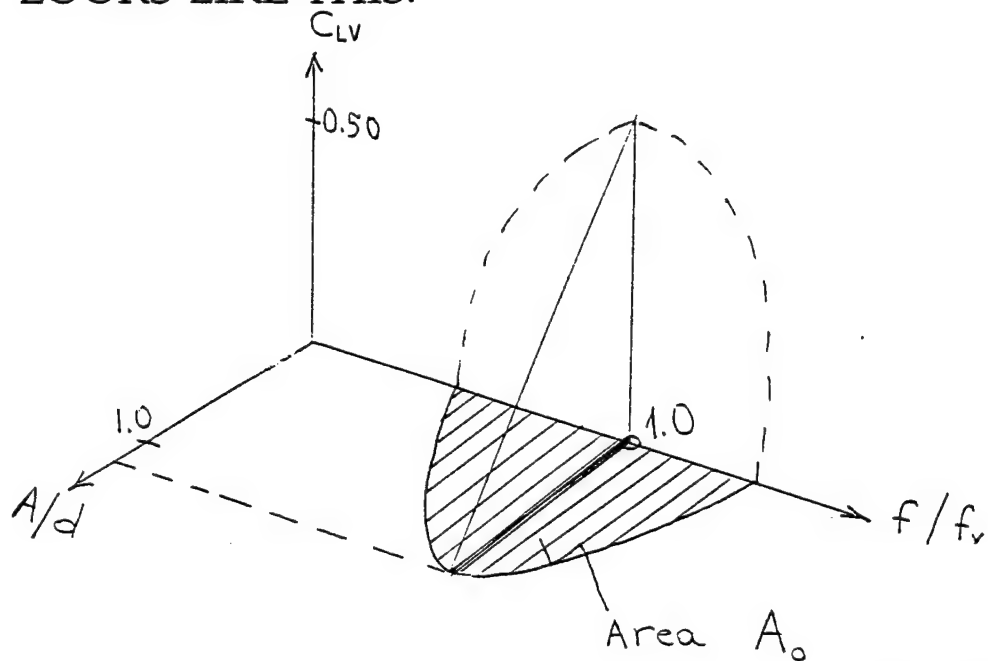FIGURE 4

A COMPOSITE THREE-DIMENSIONAL PLOT
LOOKS LIKE THIS:

FIGURE 5

(3) WHEN THE CYLINDER IS EXCITED AT TWO
FREQUENCIES, (ω_1, ω_2) THEN WE
DISTINGUISH THREE CASES:

(I) ω_1, ω_2 in A_0

(II) ω_1 in A_0, ω_2 outside

   [or, ω_1 outside A_0, ω_2 in A_0]

(III) ω_1, ω_2 outside A_0

103

CASE III IS UNIMPORTANT, CASE II IS SIMPLE, BECAUSE C_{LV} IS ALMOST THE SAME AS WHEN THERE IS ONLY ONE EXCITATION FREQUENCY (THE ONE INSIDE A_o). <u>CASE I, HOWEVER, REQUIRES EXPERIMENTAL DATA</u>.

(4) WHEN THE CYLINDER IS EXCITED AT MULTIPLE FREQUENCIES (MORE THAN TWO), IN PRINCIPLE, THE PREVIOUS CASE (TWO FREQUENCIES) PROVIDES A GOOD DESCRIPTION OF THE QUALITATIVE RESPONSE.

3. DRAG COEFFICIENT

(1) THE DRAG COEFFICIENT HAS THE
NOMINAL VALUE 1.2 WHEN THE CABLE IS
STATIONARY. WHEN THE CABLE IS
MOVING AT AMPLITUDE A AND
FREQUENCY f_v , THEN C_D INCREASES:

$$C_D \simeq C_{DO} * (\text{amplification factor})$$

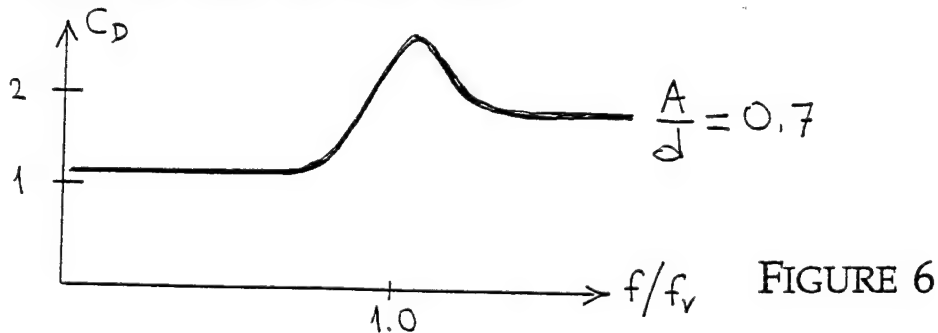IF THE FREQUENCY $f \neq f_v$, THEN
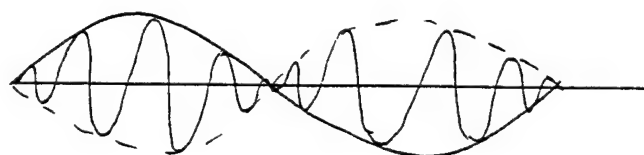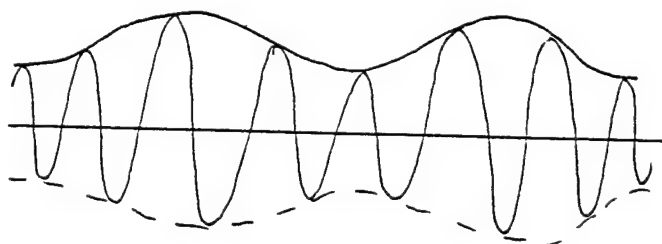AMPLIFICATION IS LOWER.

FIGURE 6

(2) IN CASE OF TWO OR MORE FREQUENCIES
OF EXCITATION, C_D VARIES
CONSIDERABLE AS A FUNCTION OF
FREQUENCIES AND AMPLITUDES
IMPOSED.

105

A CASE OF PARTICULAR INTEREST IS
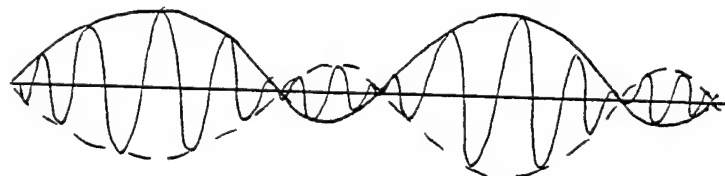## BEATING OSCILLATIONS

TYPES OF BEATING

TYPE I

TYPE II

TYPE III

FIGURE 7

THE FOLLOWING MODELS DESCRIBE THE
VARIOUS TYPES:

$$y(t) = A \sin \omega t \left\{ 1 + 2\alpha \cos \delta t \right\}$$

TYPE I $\quad \alpha = \frac{1}{2}$

II $\quad \alpha < \frac{1}{2}$

III $\quad \alpha > \frac{1}{2}$

EXPERIMENTS ARE NEEDED TO FIND c_D IN BEATING OSCILLATIONS FOR ALL THREE TYPES AS FUNCTION OF $\omega, \alpha, \delta, A$

ONE SHOULD NOTE: THE REASON C_D IS A COMPLICATED FUNCTION OF BEATING CHARACTERISTICS IS THAT WHEN THE AMPLITUDE IS SMALL, VORTEX SHEDDING RESEMBLES THAT OF A STATIONARY CYLINDER. WHEN THE AMPLITUDE IS LARGE, IT RESEMBLES THE LOCK-IN CASE. THE SWITCHING BETWEEN THESE TWO MODES IS NOT SMOOTH AND AT TIMES IT IS RANDOM. HENCE AVERAGING C_D IS A COMPLICATED MATTER.

4. C_L PREDICTIVE MODEL

BASIC RELATION

$$\widetilde{C}_{LV} = H\left(\frac{f}{f_o}\right) \widetilde{C}_{LVO} - G\left(\frac{f}{f_o}\right) \frac{A}{d} \qquad (1)$$

THIS RELATION IS OBTAINED BY CURVE-FITTING EXPERIMENTAL DATA. $H(x)$, $G(x)$ ARE FUNCTIONS DETERMINED BY THE DATA. $\widetilde{C}_{LV}$, $\widetilde{C}_{LVO}$ ARE AMPLITUDES OF DRAG COEFFICIENT, EXPERIMENTALLY DETERMINED. THE EXACT MEANING OF THIS EQUATION IS FAR MORE COMPLEX THAN WHAT APPEARS AT FIRST SIGHT: THE FUNCTIONS H AND G ARE FUNCTIONS OF FREQUENCY, SO IN THE TIME DOMAIN THEY REPRESENT INTEGRO-DIFFERENTIAL OPERATORS. ALSO, THIS IS THE AMPLITUDE OF C_L IN PHASE WITH VELOCITY. FOR EXAMPLE, IF THE IMPOSED MOTION IS SINUSOIDAL AT FREQUENCY $f = f_v$, THEN THE EQUATION ABOVE RESULTS IN THE FOLLOWING RELATION:

$$C_{LV} = \widetilde{C}_{LV} \cos\left(2\pi f_v\, t\right) \qquad (2)$$

$$\widetilde{C}_{LV} = 0.70 \left\{ 1 - \frac{A}{d} \right\} \qquad (3)$$

$$y(t) = A \sin\left(2\pi f_v\, t\right) \qquad (4)$$

WHERE THE EXACT SHAPE OF C_{LV} IS SUGGESTED BY FIGURE 3.

IF Y(t) IS NOT EXACTLY SINUSOIDAL, BUT IT HAS A NARROW BAND SPECTRUM AROUND f_v THEN (2) THROUGH (4) ARE WRITTEN AS:

$$C_{LV} = 0.70 \frac{v(t)}{\hat{v}(t)} - \frac{0.70}{2\pi f_v d} v(t) \quad (5)$$

WHERE $\hat{V}(t)$ DENOTES THE ENVELOPE OF

$$V(t) = \frac{dy(t)}{dt}$$

IN THE GENERAL CASE (5) CAN BE EXTENDED TO ACCOUNT FOR DIFFERENT FREQUENCIES THAN f_v.

THE COEFFICIENT $\tilde{C}_{LV}$ IS OBTAINED BY
TAKING THE CROSS-CORRELATION BETWEEN
$C_L(t)$ AND $V(t)$

$$\langle C_L(t), V(t) \rangle = \lim_{T \to \infty} \frac{1}{2T} \int_{-T}^{T} C_L(t) \, V(t) \, dt \quad (6)$$

$$\tilde{C}_{LV} = 2 \frac{\langle C_L(t), V(t) \rangle}{\sqrt{2 \langle V(t), V(t) \rangle}} \quad (7)$$

$\langle V(t), V(t) \rangle$ IS THE AUTO-CORRELATION OF $V(t)$

$$\langle V(t), V(t) \rangle = \lim_{T \to \infty} \frac{1}{2T} \int_{-T}^{T} V^2(t) \, dt \quad (8)$$

5. CABLE PREDICTIVE MODEL

VORTEX-INDUCED VIBRATIONS ARE OF HIGH
FREQUENCY. THE APPROPRIATE MODEL FOR
LONG CABLES IS THAT OF A STRING WITH
VARIABLE PROPERTIES:

$$m \frac{\partial^2 y}{\partial t^2} + b \frac{\partial y}{\partial t} = \frac{\partial}{\partial s}\left[T(s) \frac{\partial y}{\partial s}\right] + f(s,t)$$

THE END EFFECTS ARE NEGLIGIBLE, SO AN
INFINITE LENGTH MAY BE ASSUMED. THE
GREEN'S FUNCTION DUE TO A SINUSOIDAL
FORCE OF AMPLITUDE f_o, SITUATED AT $s = \xi$,
OF FREQUENCY ω, IS

$$G(s,\xi,\omega) = \frac{1}{2\pi i \, K(\xi) T(\xi)} \sqrt[4]{\frac{T(\xi)}{T(s)}} \; E(s,\xi) \tag{9}$$

$$E(s,\xi) = \exp\left\{-i \int_{s_1}^{s_2} k(x) \, dx\right\} \tag{10}$$

$$\text{if } s > \xi \text{ then } \begin{cases} s_2 = s \\ s_1 = \xi \end{cases} ; \quad \text{else} \begin{cases} s_2 = \xi \\ s_1 = s \end{cases}$$

$$k(\xi) = \frac{m\omega^2 - i\omega b}{T(\xi)} \tag{11}$$

IF THERE IS DISTRIBUTED FORCE OF VARIABLE FREQUENCY ALONG THE LENGTH

$$f(s,t) = Re\left\{ f_o(s) \ e^{i\,\omega(s)\,t} \right\} \tag{12}$$

THEN THE RESPONSE IS

$$y(s,t) = Re\left\{ \int_{-\infty}^{\infty} f_o(\xi) \ e^{i\omega(\xi)t} \ G\big(s,\xi,\omega(\xi)\big)\,d\xi \right\} \tag{13}$$

WHERE $Re(x)$ MEANS REAL PART OF x.

6. CORRELATION LENGTH

VORTICES SHED BEHIND A LONG CYLINDER ARE CORRELATED OVER DISTANCES WHICH DEPEND ON THE REYNOLDS NUMBER, THE CHARACTERISTICS OF THE SHEAR FLOW, THE INTENSITY OF TURBULENCE AND THE AMPLITUDE AND FREQUENCY OF THE CYLINDER'S MOTION.

IN A STATIONARY CYLINDER, THE CORRELATION LENGTH IS SMALL (2-5 DIAMETERS FOR REYNOLDS NUMBER ABOVE 4,000). WHEN THE CYLINDER MOVES, HOWEVER, SIGNIFICANT SELF-ORGANIZATION OF THE FLOW OCCURS. VISUALIZATION PICTURES SHOW COMPLETE ORGANIZATION AT THE ANTINODES, WHILE AT NODES THREE-DIMENSIONAL EFFECTS DESTROY CORRELATION.

USING THESE BASIC FACTS, WE OBTAIN THE FOLLOWING CONDITION FOR THE CORRELATION LENGTH $L_c(s)$

$$Re \left\{ \sqrt{\frac{m\omega^2 - i\omega b}{T(s)}} \quad L_c(s) \right\} = \pi \qquad (14)$$

7. IMPLEMENTATION

THE MODEL IS IMPLEMENTED AS FOLLOWS:

(1) THE NORMAL VELOCITY U_n IS FOUND AT EACH POINT OF THE CABLE AND HENCE THE STROUHAL FREQUENCY f_s, ω_s

$$f_s = (St) \frac{U_n}{d} \tag{15}$$

$$\omega_s = 2\pi f_s \tag{16}$$

(2) USING EQUATION (14), THE CORRELATION LENGTH IS DETERMINED ALONG THE CABLE LENGTH, I.E. $L_c(s)$

(3) THE RESPONSE $Y(s,t)$ IS FOUND FROM EQUATION (13) USING A FORCE MODEL CONSISTING OF CORRELATED CABLE SEGMENTS OF LENGTH $L_c(s)$ OSCILLATING FREQUENCY $\omega_s(s)$. FOLLOWING EQUATION (1) THE FIRST TERM

$$H\left(\frac{f}{f_o}\right) \tilde{C}_{Lv_0}$$

PROVIDES THE AMPLITUDE OF THE
EXCITATION FORCE, WHILE THE
SECOND TERM

$$- G \left(\frac{f}{f_0} \right) \frac{A}{d}$$

PROVIDES DAMPING. THIS IS MORE
CLEARLY SEEN FROM EQUATION (5):

$$m \frac{\partial^2 y}{\partial t^2} + b \frac{\partial y}{\partial t} - \frac{\partial}{\partial s} \left[T(s) \frac{\partial y}{\partial s} \right] =$$

$$= f(s,t) =$$

$$= \frac{1}{2} \rho \, d U^2 \left\{ 0.7 \frac{v(t)}{\hat{v}(t)} - \frac{0.7}{2\pi f_v d} \frac{\partial y}{\partial t} \right\}$$

RESULTING IN:

$$m \frac{\partial^2 y}{\partial t^2} + \left\{ b + \frac{1}{2} \rho \, d U^2 \frac{0.7}{2\pi f_v d} \right\} \frac{\partial y}{\partial t}$$

$$- \frac{\partial}{\partial s} \left[T(s) \frac{\partial y}{\partial s} \right] = \frac{1}{2} \rho \, d U^2 \, 0.7 \left[\frac{v(t)}{\hat{v}(t)} \right]$$

$$(17)$$

WHERE ♭ IS THE STRUCTURAL DAMPING.

THE TERM $\dfrac{V(t)}{\hat{V}(t)}$ POSES EXTREME DIFFICULTIES.

FOR THIS REASON THE SOLUTION IS
OBTAINED ITERATIVELY:

(I)   FIRST ASSUME

$$\frac{V(t)}{\hat{V}(t)} = \cos\left(\omega_v\, t\right)$$

(II)   SOLVE (17) TO FIND $Y(s,t)$

EVALUATE $\left\langle \dfrac{\partial y}{\partial t}(s,t)\,,\, f(s,t) \right\rangle$

$\left\langle \dfrac{\partial y}{\partial t}(s,t),\, \dfrac{\partial y}{\partial t}(s,t) \right\rangle$ USING (7),(8)

(III)   REPEAT CALCULATION USING
MODIFIED LIFT COEFFICIENT
C_L^* , SUCH THAT $\left\langle C_L^*(s,t),\, \dfrac{\partial y}{\partial t}(s,t) \right\rangle^2$

$$= \left\langle C_L(s,t)\,,\, C_L(s,t) \right\rangle \left\langle \frac{\partial y}{\partial t}(s,t),\, \frac{\partial y}{\partial t}(s,t) \right\rangle$$

(18)

IX. ANALYSIS OF THE DRAG AND VORTEX-INDUCED VIBRATIONS OF THE SAIC CABLE WITH HAIRED FAIRING

9.1 Introduction

This report contains the results of experimental measurements and numercial calculations of the hydrodynamic forces of the SAIC cable with haired fairing. In the experiments, we measured lift and drag forces of the cable section undergoing forced oscillations. We then used these data as input into our numerical model that calculates drag coefficients and flow-induced vibrations of long marine cables (made from the same material that is being tested) in a shear current.

The experiments were performed at the Massachusetts Institute of Technology (MIT) Towing Tank using a special apparatus (figure 9.1) that we designed to oscillate a cylinder transverse to a flow. The apparatus was attached to the towing carriage and towed down the tank at a constant velocity. At the same time, the cylinder was oscillated up-and-down with a given motion and at a constant frequency.

The lift and drag forces were measured using a highly sensitive and mechanically stiff three-axis quartz piezoelectric force transducer. The position of the cylinder was measured with a Linear Variable Differential Transformer. The analog signals from these instruments were low-pass filtered at 100 Hz (to avoid aliasing) and then recorded digitally at 400 Hz using a 16 channel A/D input converter with sample-and-hold capabilites.
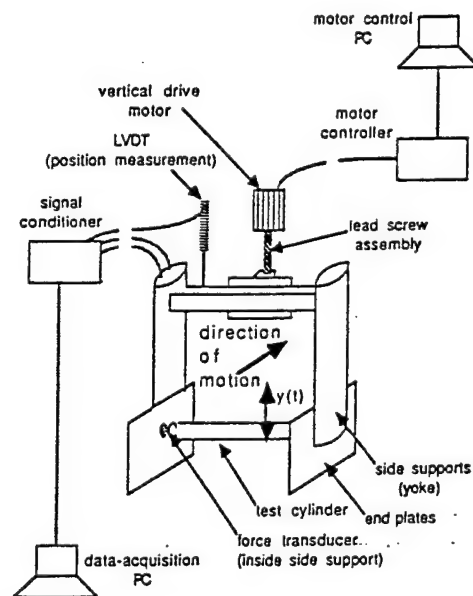

Figure 9.1: The experimental set-up used in the Towing Tank.

All of the forced oscillation experiments were performed at a towing speed of 0.4 m/s. This corresponds to a Reynolds number of approximately 10,000 which is typical for marine cables operating in the open ocean. The cylinder motion $z(t)$ was pure sinusoidal at a given oscillation frequency f_o and an amplitude-to-diameter ratio of $\frac{A}{d}$:

$$z(t) = \frac{A}{d} \sin 2\pi f_o t \qquad (9.1)$$

Three values of $\frac{A}{d}$ were tested: $\frac{A}{d} = 0.15$, $\frac{A}{d} = 0.30$, and $\frac{A}{d} = 0.50$. At each of the amplitudes we tested 25 frequencies ranging from 0 to 2 times the Strouhal frequency. The Strouhal frequency is the frequency of vortex shedding corresponding to the case of stationary motion and is defined as:

$$St = \frac{f_s d}{U} \qquad (9.2)$$

where f_s is the vortex shedding frequency, d is the cylinder diameter, and U is the tow speed. For a smooth circular cylinder, $St = 0.2$; for the SAIC cable, $St = 0.14$.

The experimental data will be presented in graphical form in terms of the lift and mean drag coefficients. The lift and mean drag coefficients are defined as:

$$C_L = \frac{L_o}{\frac{1}{2}\rho l d U^2} \qquad (9.3)$$

$$C_D = \frac{D_m}{\frac{1}{2}\rho l d U^2} \qquad (9.4)$$

where L_o is the amplitude of the oscillatory lift force and D_m is the mean drag force. The water density is ρ, the cylinder length is l, the cylinder diameter is d, and the towing velocity is U.
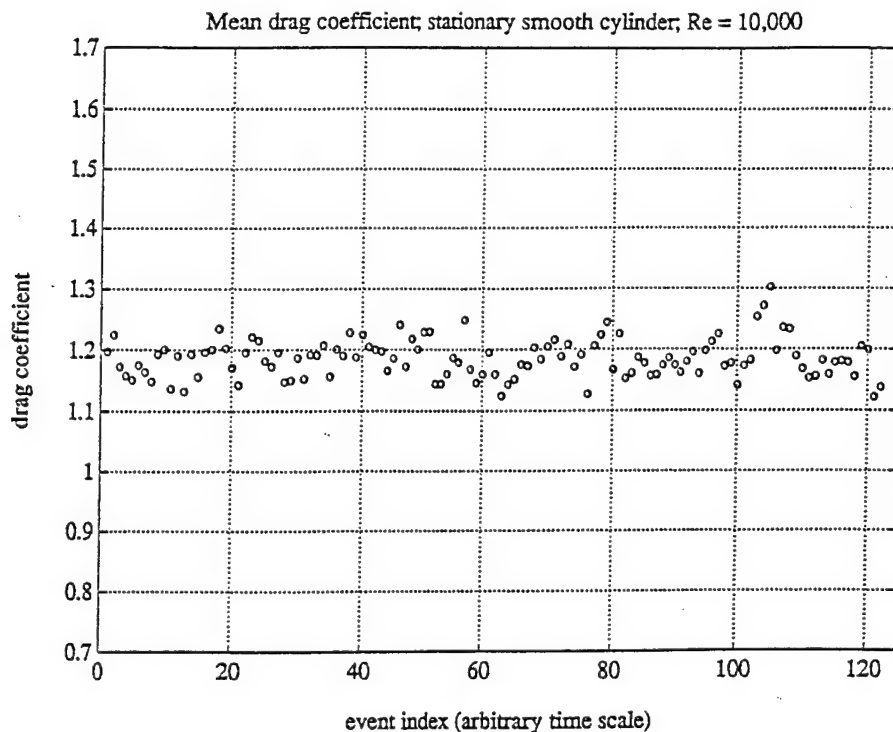
Figure 9.2: One hundred, twenty-two (122) measurments of the mean drag coefficient of a stationary smooth circular cylinder measured over a two year period.

9.2 Experimental Results

9.2.1 RESULTS FOR SMOOTH STATIONARY CYLINDER

The purpose of figures 9.2 – 9.4 are to show the accuracy of the apparatus in measuring lift and drag forces on cylinders. There is much data in the scientific and engineering literature for smooth circular cylinders that are held stationary. Over the past 2 years, we have accumulated data for smooth circular cylinders as a measure of the accuracy and consistency-over-time of our apparatus. Our measurements of mean drag coefficient, Strouhal number, and lift coefficient are within the accepted ranges for published values.

Typical values for the mean drag coefficient for a Reynolds number of 10,000 are C_D equals 1.1 to 1.3. The average of our 122 measurements that we have made over a period of 2 years is 1.1856 with a standard deviation of 0.0315 (figure 9.2).

Strouhal numbers for stationary smooth circular cylinders have been measured between 0.18 and 0.22. Our average for the 122 measurements is 0.1932 with a standard deviation of 0.0014 (figure 9.3).

Values for lift coefficients (measured by others) range from 0 to 0.8 and typically have scatter due to three-dimensional effects. Our data (figure 9.4) is consistent with these past studies.
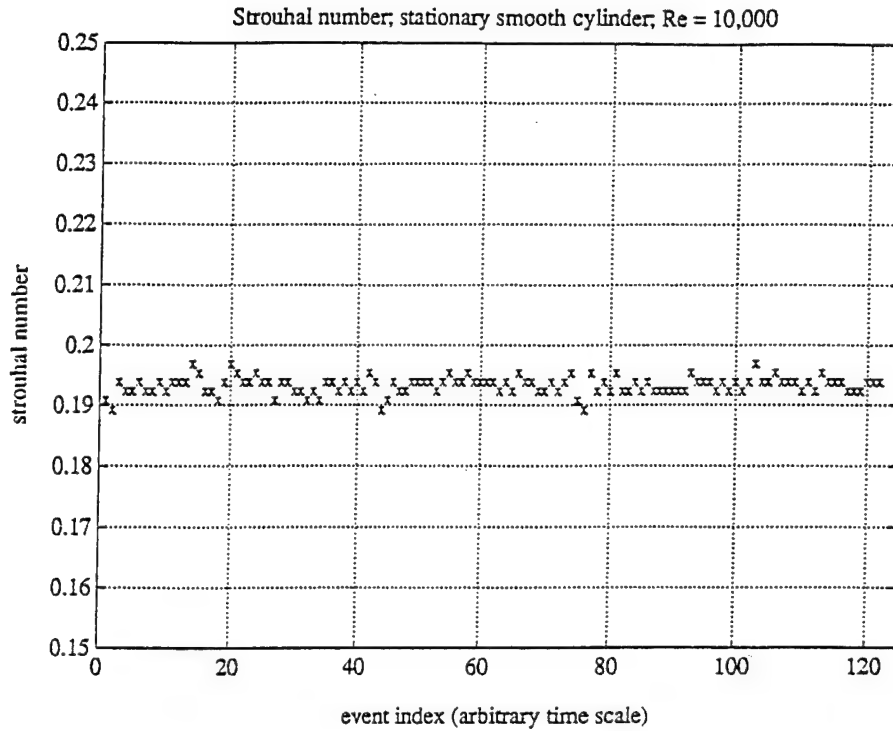
119

Figure 9.3: One hundred, twenty-two (122) measurments of the Strouhal number of a stationary smooth circular cylinder measured over a two year period.
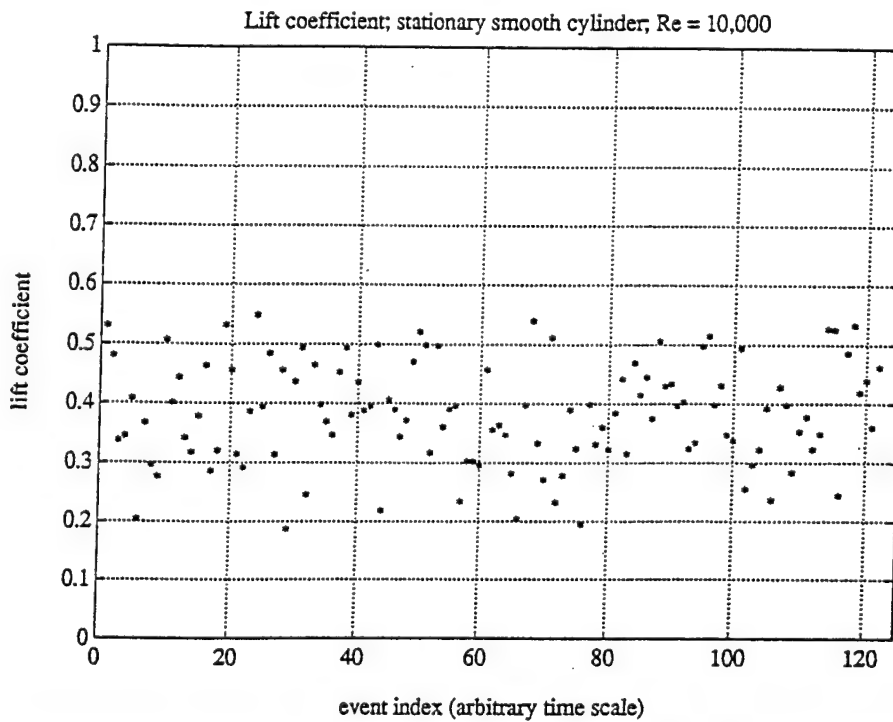

Figure 9.4: One hundred, twenty-two (122) measurments of the lift coefficient of a stationary smooth circular cylinder measured over a two year period.

9.2.2 Lift Coefficients for SAIC Cable with Haired Fairing

The most important data for determining the equilibrium motion of a freely vibrating cable (i.e. amplitude and frequency of motion of the cable) is the *lift coefficient in phase with the cylinder velocity*. If this value is positive, then energy is being pumped into the cylinder, and its amplitude would increase if the cylinder was not constrained. If value of the *lift coefficient in phase with the cylinder velocity* is negative, then the motion of the cylinder is being resisted by the fluid, there is drag, and the cylinder amplitude would decrease if it was vibrating freely. When the *lift coefficient in phase with the cylinder velocity* is zero, there is equilibrium. Roughly, the amplitude of vibration at which this occurs will be the upper bound for the amplitude of vibration of a long marine cable made from the same material of that being tested.

Figure 9.5 gives the *lift coefficient in phase with the cylinder velocity*. The values are plotted versus the nondimensional frequency of motion of the cylinder which is defined as:

$$\frac{f_o d}{U} \tag{9.5}$$

where f_o is the frequency at which the cylinder is being oscillated, d is the cylinder diameter, and U is the flow velocity. Data are given for three different amplitude-to-diameter ratios.

What is clear is that for an amplitude-to-diameter ratio of $A/d = 0.50$ the fluid is always acting to damp the motion of the cylinder. For $A/d = 0.30$ and $A/d = 0.15$ there is a region were the fluid is exciting the motion of the cylinder. From this we estimate that the maximum strumming amplitude is between 0.30 and 0.50 cable diameters. Linear interpolation gives a value of 0.38.

9.2.3 Contour Plot of Lift Coefficient In-Phase with the Cylinder Velocity

To get a better indication of what are the equilibrium amplitude and frequency of vibration of the SAIC haired fairing cable, we constructed a contour plot (figure 9.6) of the *lift coefficient in phase with the cylinder velocity*. The X-axis is the nondimensional frequency of motion $\frac{fd}{U}$ and the Y-axis is the amplitude-to-diameter ratio, A/d. The contour lines represent lines of constant lift coefficients. The important line is the one corresponding to $C_L = 0$. The equilibrium motion of the cylinder is located on this line. From stability arguments, the equilibrium motion is located at the peak of the $C_L = 0$ curve. From this we conclude that the equilibrium amplitude of vibration is $A/d = 0.38$ and the equilibrium frequency of motion is $\frac{fd}{U} = 0.145$.

9.2.4 Upper Bound of Mean Drag Coefficients of SAIC Cable

Once we have the equilibrium values for the amplitude of vibration and the frequency of vibration of the SAIC cable section, it is a simple matter to determine an upper bound for the mean drag coefficient. Figure 9.7 is a plot of the mean drag coefficient as a function of nondimensional frequency. For an amplitude-to diameter ratio of $A/d = 0.38$ and a nondimensional frequency of $\frac{fd}{U} = 0.145$, we can interpolate to find that $C_D = 2.05$.

The actual mean drag coefficient of the SAIC cable when it is deployed in 5000 m of water is less than the this value due to three-dimensional effects. The results of calculations to determine the "in-situ" value are given in the next section.
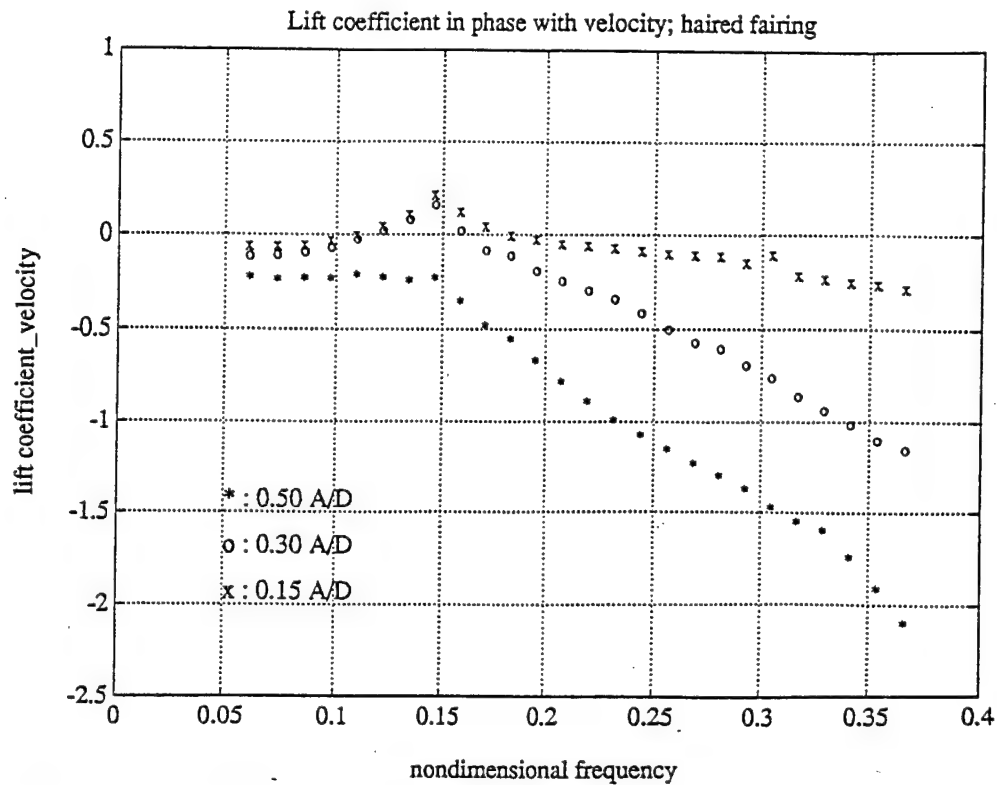
121

Figure 9.5: Laboratory measurements of the lift coefficient in phase with the velocity of motion of a section of the SAIC cable as a function of nondimensional frequency. The different symbols correspond to the three different amplitudes of motion that were used in the tests.
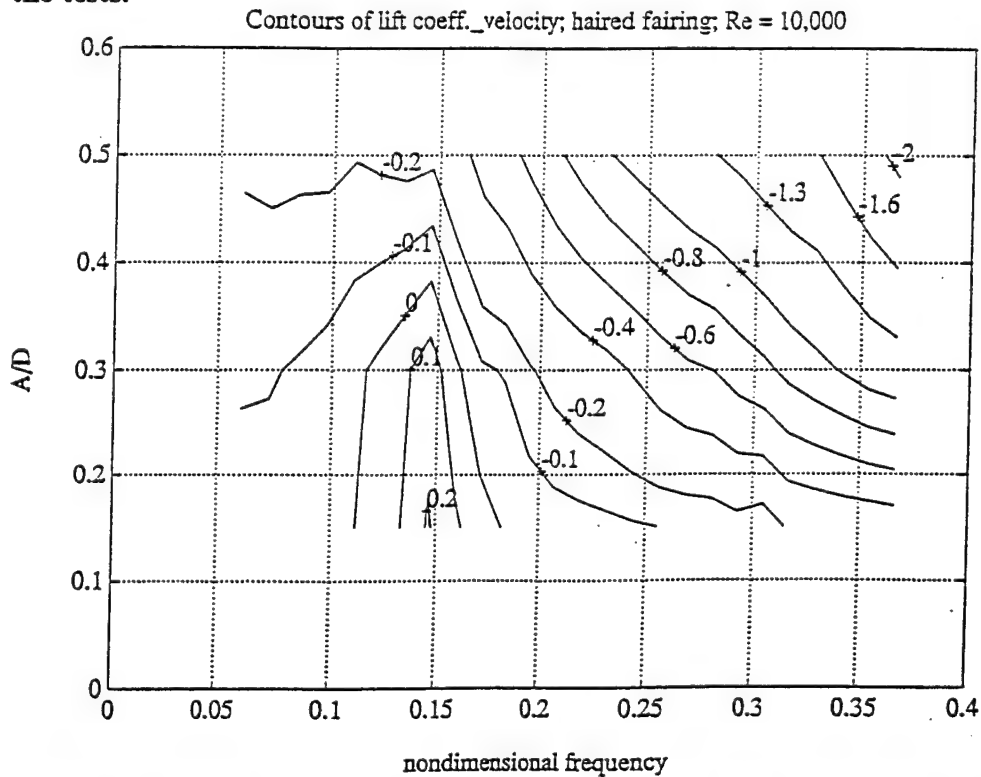

Figure 9.6: Contour plot of the lift coefficient in phase with the velocity of motion of a section of the SAIC cable.
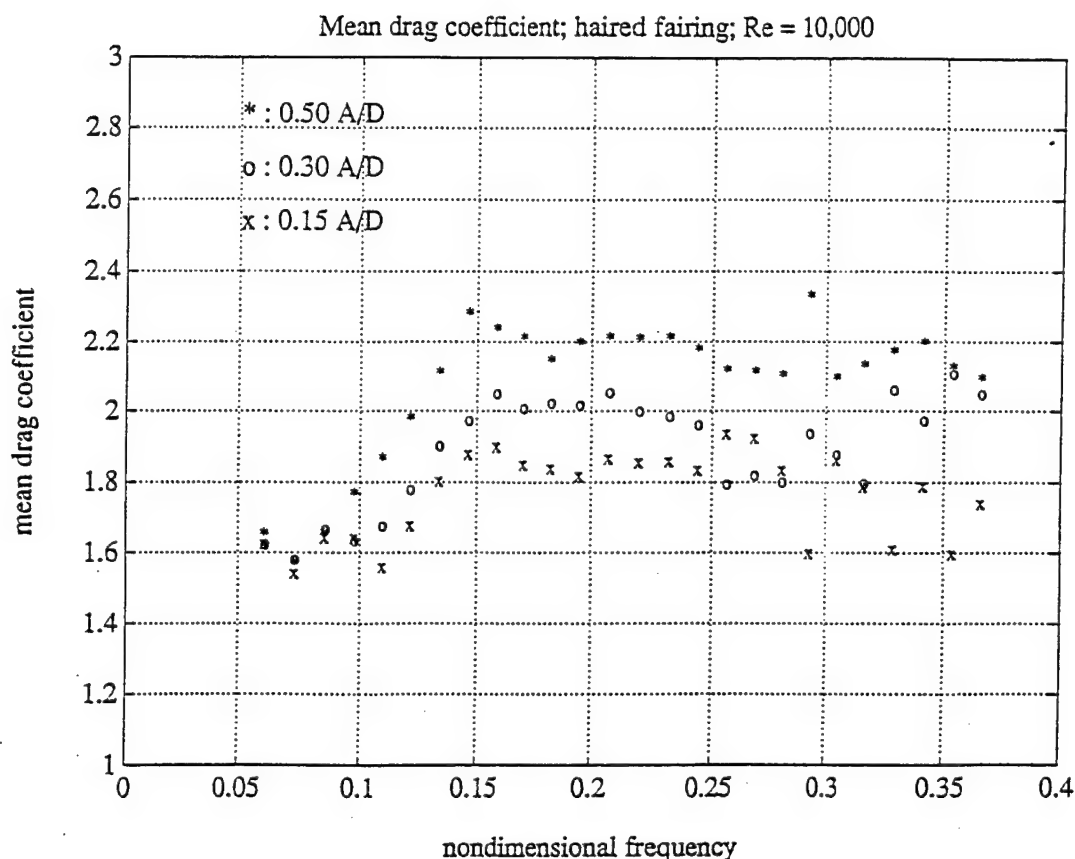
Figure 9.7: Laboratory measurements of the mean drag coefficient of a section of the SAIC cable.

9.2.5 MEAN DRAG COEFFICIENT OF A LONG MARINE CABLE IN A SHEAR CURRENT

For a long marine cable in a shear current, it is important to account for changes in the vibration frequency as a function of depth and also to account for the three-dimensional structure of the vortex shedding process. We do this with a numercal program which uses the experimental data as input.

A vibrating cable can be viewed as a wave guide. It allows motions originating at different locations along the cable to travel up and down the cable as transverse waves. These waves combine with other waves and produce the overall amplitude of motion at any given location along the cable. The amplitude of the motion is a function of the hydrodynamic forces, the same forces which we measured in the Towing Tank.

We use the data for *lift coefficient in phase with the cylinder velocity* as input into our computer model and calculate the flow-induced vibration of the SAIC cable in a shear current. Figure 9.8 is the key to our input. It gives the all-important *lift coefficient in phase with the cylinder velocity* as a function of cylinder amplitude. The drop-off in the value of the lift coefficient at low amplitudes ($\frac{A}{d} < 0.3$) is due to three-dimensional effects in the laboratory apparatus. For two-dimensional flow, the lift coefficient would follow the dashed line and be a maximum at $\frac{A}{d} = 0$. The numerical program uses the dashed curve to adjust the fluid forcing and make it either cause drag (when the local $A/d > 0.38$) or excitation (when the local $A/d < 0.38$). The output from the computer program is the maximum amplitude of vibration of the cable and the mean drag coefficient.

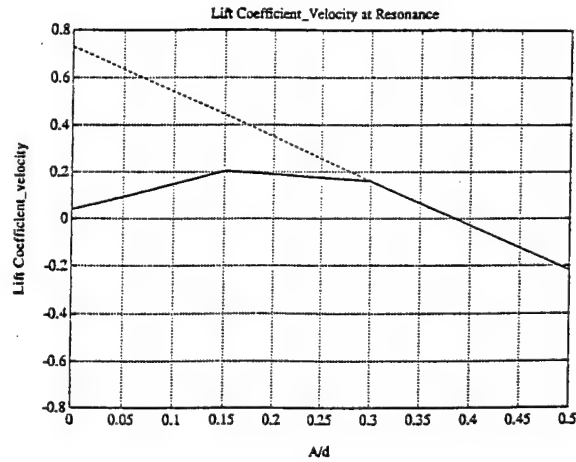For the calculations we used the following current profile:

123

Figure 9.8: The maximum lift coefficient (lift coefficient at resonance) that is in-phase with the velocity of a section of the SAIC cable, plotted as a function of amplitude-to-diameter ratio. This data are used as input for the numerical calculations.

Current Profile

Depth (m)	Current Speed (m/s)
0.	0.5
150.	0.1
5000.	0.0

The results of the calculation are $C_D = 1.9$ and $\frac{A}{d} = 0.4$. (Note: these values were determined by assuming that there was no structural damping in the cable. Marine cables have a very small amount of structural damping, and this would act to reduce the C_D and vibration amplitude slightly.)

Bibliography

[1] C.M. Ablow and S. Schechter. Numerical simulation of undersea cable dynamics. *Ocean Engng.*, 10(6):443–457, 1983.

[2] M. Abramowitz and I. Stegun. *Handbook of Mathematical Functions*. Dover Publications, 1970.

[3] C.M. Bender and S.A. Orszag. *Advanced Mathematical Methods for Scientists and Engineers*. McGraw-Hill, 1978.

[4] P. Berge, Y. Pomeau, and C. Vidal. *Order Within Chaos: Towards a Deterministic Approach to Turbulence*. John Wiley and Sons, 1984.

[5] A. Bliek. *Dynamic Analysis of Single Span Cables*. PhD thesis, Massachusetts Institute of Technology, Cambridge, Massachusetts, 1984.

[6] J.J Burgess. *Natural Modes and Impulsive Motions of a Horizontal Shallow Sag Cable*. PhD thesis, Massachusetts Institute of Technology, Cambridge, Massachusetts, 1985.

[7] J.J. Burgess. Modeling of undersea cable installation with a finite difference method. *First International of Offshore and Polar Engng Conference*, 2:222–227, 1991.

[8] J.J. Burgess and M.S. Triantafyllou. The elastic frequencies of cables. *Journal of Sound and Vibration*, 120(1):153–165, 1988.

[9] G.F. Carrier and C.E. Pearson. *Partial Differential Equations: Theory and Technique*. Academic Press, 1988.

[10] M.J. Casarella and M. Parsons. A survey of investigations on the configuration and motion of cable systems under hydrodynamic loading. *Marine Technology Society Journal*, 4(4):27–44, 1970.

[11] R. Chiou. *Nonlinear Hydrodynamic Response of Curved Singly-Connected Cables*. PhD thesis, Oregon State University, Corvallis, Oregon, 1989.

[12] Y. Choo and M.J. Caseralla. A survey of analytical methods for dynamic simulation of cable-body systems. *Journal of Hydronautics*, 7(4):137–144, 1973.

[13] G. Dahlquist and A. Bjorck. *Numerical Methods*. Prentice-Hall, 1974.

[14] T.N. Delmer, T.C. Stephens, and J.M. Coe. Numerical simulation of towed cables. *Ocean Engineering*, 10(2):119–132, 1983.

[15] T.N. Delmer, T.C. Stephens, and J.A. Tremills. Numerical simulation of cable-towed acoustic arrays. *Ocean Engineering*, 15(6):511–548, 1988.

[16] A.P. Dowling. The dynamics of towed flexible cylinders: Part 1. Neutrally buoyant elements. *Journal of Fluid Mechanics*, 187:507–532, 1988.

[17] J.E. Goeller and P.A. Laura. Analytic and experimental study of the dynamic response of cable systems. *Offshore Technology Conference*, OTC 1156, 1970.

[18] T.R. Goodman and J.P. Breslin. Statics and dynamics of anchoring cables in waves. *Journal of Hydronautics*, 10(4):113–120, 1976.

[19] F.B. Hildebrand. *Advanced Calculus for Applications*. Prentice-Hall, Inc., second edition, 1976.

[20] C.T. Howell. Numerical analysis of 2-D nonlinear cable equations with applications to low tension problems. *International Journal of Offshore and Polar Engng.*, 2(2), 1992.

[21] C.T. Howell. Investigation of large amplitude nonlinear dynamics of hanging chains. *Second International of Offshore and Polar Engng Conference*, 2, 1992 (In Press).

[22] H.M. Irvine. *Cable Structures*. MIT Press, 1981.

[23] H.M. Irvine and T.K. Caughey. The linear theory of free vibrations of a suspended cable. *Proceedings of the Royal Society of London*, A341:299–315, 1974.

[24] D.W. Jordan and P. Smith. *Nonlinear Ordinary Differential Equations*. Clarendon Press, 1987.

[25] J.W. Kamman and R.L. Huston. Modeling of submerged cable dynamics. *Computers and Structures*, 20(1-3):623–629, 1985.

[26] R.M. Kennedy. Transverse motion response of a cable-towed system: Part 1. Theory. *US Journal of Underwater Acoustics*, 30:97–108, 1980.

[27] R.M. Kennedy and E.S. Strahan. A linear theory of transverse cable dynamics at low frequency. *Naval Underwater Systems Center (NUSC) Technical Report*, Rep. 6463, 1981.

[28] J.J. Ketchmen and Y.K. Lou. Application of the finite element method to towed cable dynamics. *Proceedings Oceans 75 Conference*, 1:98–107, 1975.

[29] H. Lamb. *Dynamics*. Cambridge University Press, 1914.

[30] L.D. Landau and E.M. Lifshitz. *Theory of Elasticity*. Pergamon Press, 1959.

[31] J.W. Leonard and J.H. Nath. Comparison of finite element and lumped parameter methods for oceanic cables. *Engineering Structures*, 3:153–166, 1981.

[32] M.J. Lighthill. Note on the swimming of slender fish. *Journal of Fluid Mechanics*, 9:305–317, 1960.

[33] A. E. H. Love. *A Treatise on the Mathematical Theory of Elasticity*. Dover Publications, 1927.

[34] J.J. McCoy. Effects of bending stiffness in tow and salvage cables. *Journal of Hydronautics*, 6(2):77–82, 1972.

[35] J. Miles. Resonant, nonplaner motion of a stretched string. *Journal of Acoustical Society of America*, 75(5):1505–1510, 1984.

[36] J.H. Milgram, M.S. Triantafyllou, F. Frimm, and G. Anagnostou. Seekeeping and extreme tensions in offshore towing. *Transactions of the Society of Naval Architects and Marine Engineers*, 96:35–72, 1988.

[37] F. Milinazzo, M. Wilkie, and S.A. Latchman. An efficient algorithm for simulating the dynamics of towed cable systems. *Ocean Engineering*, 14(6):513–526, 1987.

[38] A.R. Mitchell and D.F. Griffiths. *The Finite Difference Method in Partial Differential Equations*. John Wiley and Sons, 1980.

[39] A.H. Nayfeh. *Nonlinear Oscillations*. John Wiley and Sons, 1979.

[40] J.N. Newman. *Marine Hydrodynamics*. MIT Press, 1977.

[41] C.R. Ortloff and J. Ives. On the dynamic motion of a thin flexible cylinder in a viscous stream. *Journal of Fluid Mechanics*, 38:713–720, 1969.

[42] M.P. Paidoussis. Dynamics of flexible slender cylinders in axial flow: Part 1. Theory. *Journal of Fluid Mechanics*, 26(4):717–736, 1966.

[43] M.P. Paidoussis. Stability of towed, totally submerged flexible cylinders. *Journal of Fluid Mechanics*, 34(2):273–297, 1968.

[44] M.P. Paidoussis. Dynamics of cylindrical structures subjected to axial flow. *Journal of Sound and Vibration*, 29(3):365–385, 1973.

[45] V. Papazoglou, S. Mavrakos, and S. Triantafyllou. Scaling and model testing of cables in water. *Journal of Sound and Vibration*, 140(1):103–115, 1990.

[46] N.C. Perkins. Planar and non-planar response of a suspended cable driven by small support oscillations. *First International of Offshore and Polar Engng Conference*, 2:210–215, 1991.

[47] W.H. Press, B.P. Flannery, S.A. Teukolsky, and W.T. Vetterling. *Numerical Recipes*. Cambridge University Press, 1988.

[48] G. Rega, F. Vestroni, and F. Benedettini. Parametric analysis of large amplitude free vibrations of a suspended cable. *Journal of Solids and Structures*, 20(2):95–105, 1984.

[49] J.H. Rhors. On the oscillation of a suspension cable. *Trans. Camb. Phil. Soc.*, 9:379–398, 1851.

[50] E.J. Routh. *The Advanced Part of a Treatise on the Dynamics of a System of Rigid Bodies*. Dover Publications, sixth edition, 1955.

[51] J.V. Sanders. A three-dimensional dynamic analysis of a towed system. *Ocean Engineering*, 9(5):483–499, 1982.

[52] T. Sarpkaya and M. Isaacson. *Mechanics of Wave Forces on Offshore Structures*. Van Nostrand Reinhold, 1981.

[53] J.W. Schram and S.P. Reyle. A three-dimensional dynamic analysis of a towed cable. *Journal of Hydronautics*, 2(4):213–220, 1968.

[54] H. Shin. *Nonlinear Cable Dynamics*. PhD thesis, Massachusetts Institute of Technology, Cambridge, Massachusetts, 1987.

[55] H. Shin. Analysis of extreme tensions in a snapping cable. *First International of Offshore and Polar Engng Conference*, 2:216–221, 1991.

[56] C.P. Sparks. The influence of tension pressure and weight on pipe and riser deformations and stresses. *Journal of Energy Resources Technology*, 106:46–54, 1984.

[57] S. Timoshenko. *Theory of Elasticity*. McGraw-Hill, 1934.

[58] M.S. Triantafyllou. The dynamics of taut inclined cables. *Quarterly Journal of Mechanics and Applied Mathematics*, 37(3):421–440, 1984.

[59] M.S. Triantafyllou. Dynamics of cables, towing cables, and mooring systems. *The Shock and Vibration Digest*, 23(7):3–8, 1991.

[60] M.S. Triantafyllou and Grinfogel. Natural frequencies and modes of inclined cables. *Journal of Structural Engineering*, 112(1):139–148, 1986.

[61] M.S. Triantafyllou and C.T. Howell. Nonlinear impulsive motions of low tension cables. *Journal of Engineering Mechanics (ASCE)*, 118(4):807–830, 1992.

[62] M.S. Triantafyllou and C.T. Howell. Stable and unstable nonlinear response of hanging chains: Theory and experiment. *Proceedings of the Royal Society of London*, Submitted, 1992.

[63] M.S. Triantafyllou and C.T. Howell. Nonlinear unstable response of hanging chains. *Journal of Sound and Vibration*, 160(1), 1993 (In press).

[64] M.S. Triantafyllou and G.S. Triantafyllou. The paradox of the hanging string: An explanation using singular perturbations. *The Journal of Sound and Vibration*, 148(2):343–351, 1991.

[65] W. Tsai, K.P. Yue, and M.K. Yip. Resonantly excited regular and chaotic motions in a rectangular wave tank. *Journal of Fluid Mechanics*, 216:343–380, 1990.

[66] A. Watzky. Non-linear three-dimensional large-amplitude damped free vibration of a stiff elastic stretched string. *Journal of Sound and Vibration*, 153(1):125–142, 1992.

[67] R.L. Webster. Nonlinear static and dynamic response of underwater cable structures using the finite element method. *Offshore Technology Conference*, OTC 2332, 1975.